UNIVERSITY OF CASSINO AND SOUTHERN LAZIO

PhD Course

Methods, Models, and Technologies for Engineering

Cycle XXXVIII

Analysis of the Multiphysics Behavior of Innovative Materials for Advanced Electrical Applications

SSD: **IIET-01/A**

Supervisors

Prof. Antonio Maffucci

Prof. Mauro Di Monaco

PhD Student

Sarah Sibilia

Coordinator

Prof. Fabrizio Marignetti

ABSTRACT

Carbon-based nanomaterials, such as graphene, exhibit exceptional electrical, thermal, and mechanical properties, making them highly attractive for technological applications. However, the fabrication of pure and reproducible nanomaterials suitable for large-scale production remains complex and expensive. For this reason, increasing attention is being devoted to graphene nanoplatelet GNP-based nanocomposites, which preserve many of graphene's functional advantages while offering improved reproducibility and industrial feasibility.

In this work, several GNP-based formulations developed by Nanesa S.r.l. were studied, differing in both GNP concentration and binder type. Their electrical and thermal properties were determined through experimental characterization and coupled electrothermal modeling, in order to evaluate their potential use in multifunctional applications.

Two main applications were explored. The first concerns heating elements for de-icing systems, where the same material also acts as the sensing component of a planar capacitor for ice detection, thus combining heating and monitoring within a single layer. The second involves coatings for electromagnetic interference (EMI) shielding, which also act as distributed temperature sensors, showing a measurable response to temperature variations.

The results demonstrate that GNP-based nanocomposites can effectively integrate conductive, thermal, and sensing functionalities, offering a scalable and cost-effective platform for multifunctional engineering applications.

TABLE OF CONTENT

LIST OF FIGURES

LIST OF TABLES

INTRODUCTION

In recent decades, nanomaterials have attracted growing interest from both the scientific and industrial communities due to their remarkable physical, chemical, and mechanical properties, which make them highly promising materials for a wide range of technological applications. Among these, carbon-based nanomaterials—such as carbon nanotubes (CNTs), nanoribbons, and graphene—stand out for their excellent electrical and thermal conductivities, mechanical strength, and versatility of integration into various functional systems (Saleh, 2024; Cha, 2013).

Despite their great potential, the synthesis of pure nanomaterials that are reproducible, scalable at an industrial level, and easily integrable into complex devices remains a significant challenge (Ren, 2014, Saleh, 2024). The production processes required to achieve high-purity materials are often complex, expensive, and difficult to control, which limits their large-scale use. To overcome these limitations, research is increasingly focusing on the development of composite materials that, while not as pure as ideal nanomaterials, offer good reproducibility, lower costs, and adequate functional performance for practical applications (Gonçalves, 2025).

In this thesis, nanocomposites based on GNP (Graphene Nanoplatelets) are investigated. GNPs are graphene flakes consisting of a few stacked layers of graphite, combining

some of the outstanding properties of graphene with improved processability and easier dispersion in polymer matrices. The materials studied, developed by Nanesa S.r.l., feature different formulations that vary in both the GNP content and the type of binder employed.

The aim of this work is the characterization and modeling of these nanocomposites to determine their electrical and thermal properties and to evaluate their potential applicability in different technological contexts. In particular, two main applications are explored:

as heaters for de-icing systems,

and as coatings for electromagnetic interference (EMI) shielding.

Given their multifunctional nature, additional sensing functionalities are also investigated. In the first case, the material is studied as the sensitive element of a planar capacitor for ice detection; in the second, as a distributed temperature sensor integrated within the coating.

Through the experimental study and modeling of GNP-based nanocomposites, this thesis aims to contribute to the understanding of the relationships between composition, structure, and functional properties of these materials, promoting their development and use in advanced multifunctional solutions with high technological value.

Chapter 1 provides the theoretical background on nanomaterials and the coupled electrical and electrothermal models used to describe their behavior. The discussion

includes both pure graphene systems and graphene-based composites, extending to bulk materials and their macroscopic modeling approaches.

Chapter 2 presents the materials investigated in this work, including details of their manufacturing process and the experimental and modeling activities carried out to characterize the samples and estimate their electrical and thermal properties.

Chapter 3 focuses on the applications proposed for these materials, combining experimental investigations and numerical modeling to evaluate their performance as de-icing heaters and electromagnetic shielding coatings, as well as their integrated sensing functionalities.

Finally, the Conclusions summarize the main findings of the work.

CHAPTER 1
Multiphysics Models of Advanced Materials

1.1 Advanced Materials

Scientific research and industry are constantly oriented toward the realization and development of new ideas and products. At the same time, a significant part of research focuses on the optimization and continuous improvement of existing solutions, aiming to enhance efficiency, promote miniaturization, and foster sustainability. This approach naturally leads to the exploration of new materials capable of offering superior performance or being integrated into established technologies to strengthen their functional characteristics. Within this framework, particular attention has been given to nanomaterials, thanks to their distinctive properties and the possibility of tuning them by manipulating matter at the nanometric scale.

Their development and characterization are central to nanotechnology, which deals with the understanding and utilization of materials at dimensions typically below 100 nanometers. It has a wide range of potential applications, from nanoelectronics to optics, from nanobiology to medicine, and even in the creation of nanometric materials.

For nanometric materials, the physical, chemical, mechanical, and electronic properties can change radically compared to the same materials in macroscopic form. For example, a material can become stronger, lighter, or more chemically reactive.

Furthermore, it may acquire new electronic or optical properties that are not present in its traditional form.

One of the most fascinating aspects is the emergence of quantum effects, which do not occur on larger scales and allow phenomena such as superconductivity or colour changes depending on particle size. Another key feature is the large surface area relative to volume, which makes these materials particularly suitable for applications such as chemical catalysis, energy storage, or molecular filtration.

The possibility of working on the nanometric scale makes it possible to create materials with tailored properties.

1.1.1 Carbon Nanomaterials

In the field of nanotechnology, many of the most widely used innovative materials have carbon as their main element. Carbon is the basic element of organic chemistry, making it the raw material of life. Thanks to the flexibility of its bonds, carbon-based materials can take on various structures with different physical properties. It can be a good metallic conductor in the form of graphite, a good semiconductor in the form of diamond, or even an insulator when it reacts with hydrogen (Charlier, 2007). The changes in physical properties are largely due to the dimensionality of these structures.

Depending on the number of dimensions greater than the nanometric scale, the material is referred to as 0-D, 1-D, 2-D, or 3-D. For example, fullerene is an allotrope of carbon that appears as a hollow sphere made up of carbon atoms and, being nanometric in all three dimensions, is defined as a 0-D material. Other forms in which carbon can be found, used in

nanotechnology, include quantum dots: semiconductor nanocrystals that emit light and are used in applications such as medical imaging or diagnosis (Abdellatif, 2022), and photonics (Lee, 2012; Prabhakaran, 2012), carbon nanotubes (CNTs) (Shariatinia, 2021) (1-D cylindrical structures that are highly strong and conductive) and graphene (Mbayachi, 2021) (a single layer of carbon atoms in a 2-D honeycomb structure), widely used in electronics, sensors, batteries, and composite materials.

The nanomaterial that this thesis has focused on is graphene itself. Graphene is the name given to a two-dimensional sheet of sp2-hybridized carbon. Its extended honeycomb network is the basic building block of other important allotropes; it can be stacked to form 3D graphite, rolled to form 1D nanotubes, and wrapped to form 0D fullerenes. In the graphene structure each carbon atom is covalently bonded to three other carbon atoms in a hexagonal array, leaving one free electron per each carbon atom. This free electron exists in a p-orbital that sits above the plane of the material. Each hexagon in the graphene sheet exhibits two pi-electrons, which are delocalized, allowing for an efficient conduction of electricity. The corresponding resistivity of graphene sheets is in the order of 10^{-6} Ωcm.

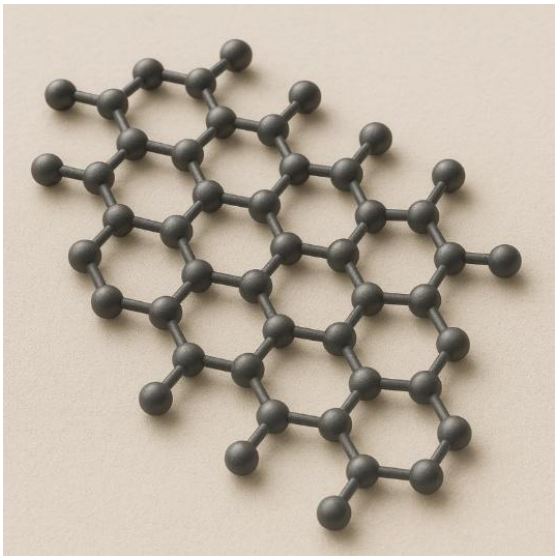

Figure 1. Single layer graphene.

Graphene also has great optical, thermal and mechanical properties. Single sheet graphene is a highly transparent material but each layer absorbs up to 2.3% of incident light (Bonaccorso, 2010), with less than 0.1% reflectance. There is also a linear absorbance increase with respect to the number of layers stacked on top of each other. A suspended graphene sheet can exhibit a thermal conductivity of 3000-6000 $Wm^{-1}K^{-1}$ at room temperature.

However, this can drop to as low as 600 $Wm^{-1}K^{-1}$ when it is attached to another substrate. The drop is caused by a scattering of phonons at the interface which impedes their movement, whereas in free standing graphene the phonon path is uninterrupted. Even at this lower conductivity, the thermal conductivity is still twice as high as copper. Graphene is also known to be a material with high tensile stress, with a Young's modulus of 1 TPa and Poisson's ratio of 0.416 (Xu, 2018).

1.1.2 Nanocomposite Materials

From a technological perspective, the discussion of nanomaterials naturally extends to nanocomposites (Omanović-Mikličanin, 2020), which represent one of their most significant fields of application.

In general terms, a composite material consists of two or more distinct phases, each characterized by specific chemical and physical properties. These phases are commonly classified into two categories: the matrix and the reinforcement (see Figure 2).

The matrix constitutes the continuous phase and serves as the primary component of the composite. Depending on the intended application, it may be polymeric (Wang, 2011), metallic (Hu, 2016), or ceramic (Peigney, 2000). The reinforcement, instead, is typically present in smaller proportions and can take the form of fibers or particles. Although the constituent materials remain separate and are not connected through formal chemical bonds, their combination results in a composite material exhibiting enhanced properties compared to those of the individual components (Lange, 1973; Siegel, 2001).

However, for the composite material to effectively exhibit the desired new properties, the amount of reinforcement must reach a critical concentration known as the percolation threshold. Below this threshold, the reinforcing phase is dispersed as isolated entities within the matrix, contributing only marginally to the overall performance. Once the percolation threshold is reached, a continuous network of reinforcement forms throughout the matrix, enabling efficient transfer of stress, heat, or electrical charge. The exact value of this threshold depends on several factors, including the size (Zhang, 2022), orientation, and

dispersion (Rahman, 2025) of the reinforcement, as well as the nature of the matrix and the interfacial interactions between the two phases. In nanocomposites, where the reinforcements have nanometric dimensions and high specific surface area, the percolation threshold is often significantly lower than in conventional composites.

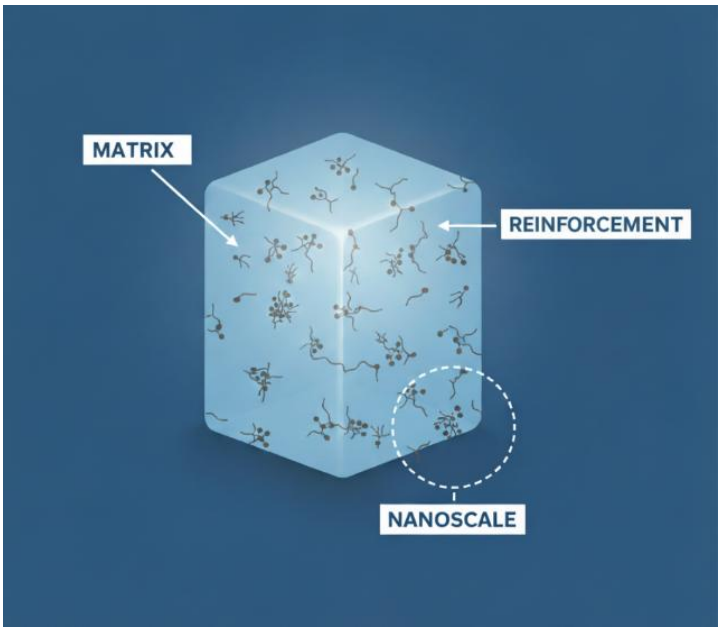

Figure 2. Explanatory illustration of the nanocomposite concept, highlighting the matrix and the nanometric reinforcement.

1.2 Theoretical Models for Nanomaterials

1.2.1 Electrical and Thermal Transport Model for Graphene

In pure graphene, each carbon atom is in the sp^2 configuration. This means that the 2s, 2px, and 2py orbitals are hybridized, forming strong σ bonds, which are responsible for the hexagonal lattice structure and the mechanical properties of graphene. The 2pz orbitals, on the other hand, are not hybridized and extend out of the plane, forming π bonds, which are responsible for the electronic properties of graphene. The σ and π orbitals are orthogonal and do not directly interact with each other; this condition changes when the graphene sheet undergoes mechanical modifications, such as bending or rolling, which cause the two orbitals to interact with each other, even partially.

In pure graphene, the conduction band and the valence band touch, giving the material a semimetallic behavior; the coupling between these orbitals can lead to the formation of a gap between the two bands, causing the material to change behavior, making it more similar to a semiconductor. Bending operations, therefore, lead to a reduction in electrical conductivity.

Different models are used to describe the electronic behavior of the nanomaterial.

Tight-Binding

The Tight-Binding (TB) (Reich, 2002) model is a framework that allows the electronic properties of graphene to be described in a simple way. The method focuses on the π electrons, which are associated with wave functions localized on the atoms. The Hamiltonian of the system accounts for two terms: the intrinsic energy of each electron on the individual carbon atom, and the hopping energy, associated with the movement of the electron from one atom to another. Generally, this second parameter is considered only for the interactions of the electron with its nearest atoms; with this approximation, one speaks of nearest-neighbour hopping. By applying the model, both the valence band and the conduction band are obtained, successfully capturing the peculiarities of graphene (namely the Dirac points), where the two bands touch and the material behaves as a semimetal, and the Dirac cones, where the particles behave like massless Dirac fermions, with very high carrier mobility and an energy dispersion with linear behavior.

Kubo Model

A more general description of the electrical behavior of graphene is provided by the Kubo model, which is based on linear response theory. This model allows the calculation of the complex conductivity of the material as a function of frequency, temperature, Fermi level, and electron scattering time (Falkovsky, 2007; Gusynin, 2007).

The total conductivity is expressed as the sum of two main contributions:

$$\sigma(\omega) = \sigma_{intra}(\omega) + \sigma_{inter}(\omega) \quad (1)$$

where σ_{intra} represents intraband transitions, i.e., the motion of electrons within the same energy band, while σ_{inter} describes interband transitions, corresponding to the transfer of electrons between the valence and conduction bands.

The conductivity of graphene depends on several fundamental physical parameters, such as the Fermi level, temperature, average scattering time, and signal frequency. At low frequencies, in the terahertz or microwave regime, the intraband contribution dominates and graphene behaves as a two-dimensional conductor. At higher frequencies, in the infrared and visible range, the interband contribution becomes significant, leading to optical absorption of the incident radiation.

Drude Model

To obtain a simpler but still accurate description in the low-frequency regime, the Drude model (Horng, 2011) is often employed as an approximation of the Kubo formulation. This model is valid when $\hbar\omega \ll 2|\mu\_c|$, where the interband transitions can be neglected and the conductivity is dominated by the intraband processes. Under this assumption, graphene's complex conductivity can be expressed as:

$$\sigma(\omega) = \frac{e^2}{\pi\hbar^2}\frac{i|\mu_c|}{\omega + {}^{i}/_{\tau}} \quad (2)$$

where e is the electron charge, $\hbar$ is the reduced Planck constant, μ_c is the Fermi level and τ is the mean scattering time. This equation shows that graphene's conductivity is a complex

quantity: the real part of σ(ω) corresponds to resistive losses, while the imaginary part describes the inductive behavior responsible for surface plasmon propagation.

Boltzmann Model

In graphene, electrical transport properties can be analysed through the Boltzmann equation, which provides a semiclassical description of charge carrier dynamics (Min, 2011). The linear dispersion relation of its electronic bands, expressed as:

$$E = \pm \hbar v_F |k| \tag{3}$$

leads to an unusually high carrier mobility, while the overall transport behavior is mainly determined by scattering with phonons, impurities, and substrate irregularities. The general form of the Boltzmann transport equation can be expressed as:

$$\frac{\partial f}{\partial t} + v_k \nabla_r f + \frac{eE}{\hbar} \nabla_k f = \left(\frac{\partial f}{\partial t}\right)_{coll} \tag{4}$$

where *f(r, k, t)* is the electronic distribution function, v_k the group velocity, *E* the applied electric field, and the collision term represents all scattering events that drive the system toward equilibrium. Since the exact expression of the collision term is complex, it is commonly simplified through the Relaxation Time Approximation (RTA), which assumes that each electronic state relaxes back to the equilibrium distribution f_0 over an average relaxation time τ. With this assumption, the equation becomes:

$$\frac{\partial f}{\partial t} + v_k \nabla_r f + \frac{eE}{\hbar} \nabla_k f = -\frac{f - f_0}{\tau(k, T)} \tag{5}$$

Under steady-state conditions and for small electric fields, the distribution function can be linearized around equilibrium, allowing the derivation of the current density and, consequently, the electrical conductivity. Integration over the Brillouin zone leads to the well-known expression:

$$\sigma = \frac{e^2 |E_F| \tau(E_F)}{\pi \hbar^2} \quad (6)$$

where E_F denotes the Fermi energy and $\tau(E_F)$ the relaxation time at that energy. This relation highlights the dependence of conductivity on both carrier density and the mean time between scattering events, which in turn are influenced by charged impurities, acoustic and optical phonons, and surface roughness effects.

Electrical-Thermal Transport Relationship in Graphene

In metals, the relationship between electrical and thermal transport is well described by the Drude model, where the same free electrons are responsible for both charge and heat conduction. In this model, the proportionality between the two processes is expressed by the Wiedemann–Franz law, which links the electrical and thermal conductivities through the Lorenz constant (approximately 2.44×10^{-8} W·Ω·K^{-2}).

$$k_e = L \sigma T \quad (7)$$

A similar relationship can also be obtained from the Boltzmann transport equation when the relaxation time of the charge carriers does not vary significantly with energy, meaning

that the same scattering mechanisms control both electrical and thermal conduction (Ashcroft, 1976).

1.2.2 Electrothermal Modelling of Nanocomposites

The electrothermal behavior of nanocomposites is inherently complex, since both electrical and thermal transport depend on a combination of intrinsic material properties and microstructural factors such as filler distribution, particle shape, interfacial resistance, and matrix–filler interactions (Bilisik, 2022). A wide range of modelling approaches has been developed to capture these phenomena, each suited to a specific range of filler concentrations, morphologies, and coupling mechanisms.

From an electrical point of view, nanocomposites are generally treated using two main conceptual strategies: effective-medium approaches (Sevostianov, 2019) and network or percolation-based models (Wang, 2015).

In effective-medium theory (EMT or EMA), the composite is regarded as a statistically homogeneous material whose overall electrical conductivity results from the averaged contribution of conductive fillers dispersed within an insulating matrix (Choy, 2015). Classical models such as Maxwell–Garnett and Bruggeman represent the two fundamental forms of this approach (Nan, 1993), and their variants are widely used to account for high-aspect-ratio fillers, anisotropic morphologies, or interfacial barriers. These models are most effective when the filler fraction is below or moderately above the electrical percolation threshold and the dispersion remains statistically uniform.

In contrast, percolation-based and resistor-network models become essential when the filler distribution leads to discrete conductive clusters separated by thin insulating gaps. In this regime, conduction occurs through the formation of connected pathways that span the composite volume once a critical filler concentration (percolation threshold) is exceeded (Stauffer, 1992).

The effective electrical conductivity typically follows a power-law behavior as predicted by the Kirkpatrick model (Kirkpatrick, 1973), while more advanced formulations, such as the Balberg tunnelling–percolation model (Balberg, 1987), include electron tunnelling between adjacent fillers separated by nanometre-scale gaps, often described using the Simmons formulation (Simmons, 1963). Hybrid approaches, such as the McLachlan GEM model (McLachlan, 1987), combine effective-medium and percolation concepts, allowing continuous descriptions across a wide range of filler loadings. Thermal transport in nanocomposites follows analogous principles but involves distinct mechanisms. At low and intermediate filler loadings, the overall thermal conductivity is strongly affected by interfacial thermal resistance which limits the transfer of phonons across matrix–filler boundaries. Classical models such as Hasselman–Johnson (Hasselman, 1987) and Nan et al. (Nan, 1997) incorporate this effect into extended versions of Maxwell-type effective-medium formulations. In such coupled models, the local power density generated by Joule heating is incorporated into the heat-transfer equations, enabling the study of temperature-dependent effects, self-heating, or thermal runaway phenomena in conductive polymer composites and other nanostructured systems (Sherman, 1983).

Overall, the modelling of nanocomposites progresses from microscopic representations (where transport is governed by

filler topology, contact quality, and interfacial resistance) to homogenised effective-medium descriptions that capture the bulk response through averaged parameters. The choice of model depends on the filler concentration and connectivity: percolation and network approaches are appropriate near or slightly above the critical threshold, whereas effective-medium and electrothermal continuum formulations become suitable once a statistically homogeneous conductive network is established.

Maxwell–Garnett Model

The Maxwell–Garnett model is one of the foundational formulations of effective-medium theory and describes the effective properties of a composite composed of discrete inclusions embedded in a continuous host matrix. The inclusions are assumed to be small spheres, uniformly dispersed, and sufficiently separated so that their mutual interactions can be neglected. Under these assumptions, the effective conductivity (electrical or thermal) can be expressed as a function of the filler volume fraction and the intrinsic conductivities of the two phases (Sevostianov, 2019).

The effective conductivity σ_{eff} can be expressed as:

$$\sigma_{eff} = \sigma_m \frac{2\sigma_m + \sigma_f + 2f(\sigma_f - \sigma_m)}{2\sigma_m + \sigma_f - f(\sigma_f - \sigma_m)} \tag{8}$$

where σ_f and σ_m are the conductivities of the filler and matrix, respectively, and f is the filler volume fraction.

This model is asymmetric, as it explicitly distinguishes between the continuous matrix and the dispersed inclusions. It is particularly accurate for composites with low to moderate filler

concentrations, where the conductive phase does not form a continuous network and the matrix still governs the overall transport behavior. Despite its simplifying assumptions, the Maxwell–Garnett model provides an intuitive analytical framework that captures the influence of filler loading and contrast between the constituent phases on the effective transport properties.

Bruggeman Model

The Bruggeman model extends the effective-medium approach to composites in which both phases contribute comparably to transport, and no single phase can be regarded as a continuous host. In this symmetric and self-consistent formulation, each phase is treated as if it were embedded in a medium with the same effective property to be determined. The Bruggeman equation for the effective conductivity σ_{eff} can be expressed as (Stroud, 1975):

$$(1-f)\frac{\sigma_m - \sigma_{eff}}{\sigma_m + 2\sigma_{eff}} + f\frac{\sigma_f - \sigma_{eff}}{\sigma_f + 2\sigma_{eff}} = 0 \tag{9}$$

where f denotes the filler volume fraction, σ_f the filler conductivity, and σ_m the matrix conductivity.

Because of its self-consistent nature, this model is more accurate for intermediate and high filler loadings, where the conductive phase begins to form interconnected paths. It can qualitatively predict the transition from an insulating to a conductive state (corresponding to the percolation threshold) and thus represents a more general description of transport in composites with a complex, interconnected microstructure. The

Bruggeman model is therefore particularly suitable for nanocomposites containing carbon-based fillers such as graphene, where both matrix and filler phases significantly influence the overall electrical and thermal response.

Kirkpatrick Model

The Kirkpatrick model represents the fundamental formulation of classical percolation theory applied to transport phenomena in heterogeneous materials (Kirkpatrick, 1973).

It provides a statistical framework to describe the abrupt transition from an insulating to a conductive state that occurs when the volume fraction of the conductive phase exceeds a critical value, known as the percolation threshold (f_c).

In a disordered composite, conductive fillers are randomly distributed within an insulating matrix. As the filler fraction increases, isolated conductive clusters begin to connect, eventually forming a continuous network that spans the entire material. This process can be described as a second-order phase transition, where the macroscopic conductivity σ_{eff} grows according to a power law (Bauhofer, 2009):

$$\sigma_{eff} = \sigma_0 (f - f_c)^t \text{ for } f > f_c \tag{10}$$

where f is the filler volume fraction, f_c is the percolation threshold, σ_0 is a scaling constant related to the intrinsic filler conductivity, t is the critical exponent, determined by the system's dimensionality and topology (typically $t \approx 1.6 - 2.0$in three-dimensional systems).

Below the percolation threshold ($f < f_c$), the composite remains insulating, since the conductive clusters are isolated and do not form continuous paths.

The value of f_c depends strongly on the shape, aspect ratio, and spatial arrangement of the filler: elongated or planar particles such as carbon nanotubes or graphene sheets exhibit very low percolation thresholds, owing to their high connectivity even at low concentrations.

1.3 Electrical and Thermal Model of Bulk Materials

In this thesis, the materials investigated are composites based on Graphene Nanoplatelets (GNP), which are used as a reinforcing phase within matrices of different types. These materials contain GNP loadings significantly higher than the typical percolation thresholds and the filler content is well above this limit. Therefore, the focus is not on the formation of conductivity or percolation effects, but rather on characterizing the overall behavior of the material once it already behaves as a conductive and thermally active system.

Although these are multiphase materials, they are industrial products manufactured through standardized processes that ensure high homogeneity and good reproducibility of their properties. This is particularly important, as it reduces uncertainties related to nanoparticle dispersion and microstructural variations, which are often present in laboratory-prepared composites. As a result, these materials can be reliably analyzed and described at the macroscopic scale. Consequently,

their analysis and modeling can be performed using the same theoretical approaches and models typically applied to conventional bulk such as copper or aluminum.

Their electrical and thermal properties can be studied through constitutive models, without the need to account for nanoscale effects or percolation behavior. This approach simplifies the analysis and allows for a direct comparison between experimental data and theoretical prediction.

1.3.1 Electrical Model for Bulk Materials

A material is defined as *bulk* when it is large enough to be considered a continuous and homogeneous medium, in which surface and size effects can be neglected. In this case, its electrical behavior can be described through macroscopic quantities such as current density and electric field. At the macroscopic level, Ohm's law provides the simplest and most direct description of the relationship between these two physical quantities and can be expressed as:

$$J = \sigma E, \tag{11}$$

where J is the current density, E the electric field, and σ the electrical conductivity of the material.

To apply this law in the description of a material's electrical behavior, the system must satisfy a series of assumptions. Specifically, the material must operate within the linear response regime, where the current density is directly proportional to the applied electric field; the medium is assumed to be homogeneous and isotropic, so that the electrical conductivity is constant and

direction-independent; the transport process must occur under steady-state conditions, with the average acceleration of charge carriers balanced by their interactions with the lattice; finally, the temperature and material properties are considered uniform, ensuring that the conductivity remains constant during conduction.

At the microscopic level, the most basic description of electrical conductivity is provided by Drude model, that can be expressed as:

$$\sigma = \frac{ne^2\tau}{m} \tag{12}$$

where n is the number of charge carriers per unit volume, e the elementary charge, m the electron mass, and τ the mean time between collisions.

In this model, electrons are treated as a gas of charged particles that move randomly and are accelerated by the applied electric field. Collisions with lattice ions interrupt this motion at regular intervals, characterised by a mean relaxation time τ, which represents the average time between two successive interactions. This finite relaxation time limits the electron acceleration and leads to an average drift velocity that gives rise to a measurable current.

When applied to a finite body, Ohm's law can be expressed in its macroscopic form

$$V = RI \tag{13}$$

which describes the potential difference V required to drive a current I through a resistance R.

1.3.2 Electro-Thermal Behavior and Temperature Dependence of Resistivity

Electrical conduction in conventional materials is strongly influenced by temperature. As temperature increases, the atoms in the lattice vibrate with greater amplitude, enhancing the probability of electron scattering and thereby affecting the overall resistivity of the material. This coupling between electrical and thermal effects is described through electro-thermal models, which relate the electrical resistivity (or conductivity) to temperature and, in some cases, to the heat generated by the current itself (Joule heating).

For most metals, the resistivity increases approximately linearly with temperature over a wide range. The linear approximation is valid as long as the material remains in the same phase and no significant structural changes occur. This behavior can be expressed empirically as:

$$\rho(T) = \rho_0[1 + \alpha(T - T_0)] \tag{14}$$

where:

- $\rho(T)$ is the resistivity at temperature T,
- ρ_0 is the resistivity at a reference temperature T_0 (usually 20°C)
- α is the temperature coefficient of resistivity (TCR), which quantifies how strongly the material's resistivity varies with temperature.

TCR can be defined as:

$$TCR(T) = \frac{1}{R(T)} \frac{dR(T)}{dT}. \quad (15)$$

In conventional material is generally positive but in material that involve carbon nanomaterial, positive temperature coefficient is not obvious. From a theoretical point of view, the mobility of charge carriers in carbon nanomaterials is affected by two competing mechanisms: thermal activation and carrier scattering. The first one increases carrier mobility by enabling more carriers to conduct, and the second one reduces mobility due to phonon interactions. Thermal activation dominates semiconducting systems, leading to decreased resistance as temperature rises; carrier scattering dominates in metallic systems, where resistance increases with temperature (Rahman, 2014).

In nanoscale structures such as individual carbon nanotubes (CNTs) and graphene nanoribbons (GNRs), as well as in aligned CNT bundles or GNR arrays, the distributed resistance R_d can be described as a function of temperature T.

$$R_d(T) = \frac{R_0}{l_{mfp}(T)\, M(T)}\, len \quad (16)$$

here, *len* denotes the length of the structure, $R_0 = 12.9$ kΩis the quantum of resistance, $M$is the effective number of conducting channels, and l_{mfp}represents the mean free path of charge carriers.

In this model, thermal activation influences the number of conducting channels, which tends to increase with temperature in multi-walled CNTs and GNRs, while remaining nearly

constant in single-walled CNTs (Forestiere, 2010; Forestiere, 2011; Maffucci, 2013). In contrast, scattering processes intensify with increasing temperature, leading to a reduction of the mean free path l_{mfp} (Maffucci, 2017).

According to Eq. (1), the temperature dependence of resistance can therefore exhibit either a positive or negative sign, depending on the balance between these two competing mechanisms. When thermal activation dominates over scattering, the material exhibits a Negative Temperature Coefficient (NTC) behavior, meaning that electrical resistance decreases with increasing temperature. For instance, in metallic single-walled CNTs, the number of conducting channels M is almost temperature-independent (Forestiere, 2011). In this case, thermal activation has negligible influence, and resistance increases with temperature due to scattering. On the other hand, in multi-walled CNTs or GNRs, the effective number of conducting channels M increases with temperature due to thermal activation, counteracting the scattering-induced resistance increase and leading to NTC behavior. This phenomenon has been experimentally observed, for example, in (Maffucci, 2017).

From a microscopic perspective, the Drude model can also be extended to include temperature effects through the relaxation time τ. As temperature increases, electron–phonon scattering becomes more frequent, reducing τ and thus the conductivity σ. This results in a total resistivity often expressed as:

$$\rho(T) = \rho_0 + \rho_{ph}(T) \tag{17}$$

where ρ_0 represents temperature-independent contributions (e.g., from defects or impurities) and $\rho_{ph}(T)$ accounts for phonon scattering, which generally increases with temperature.

This electro-thermal coupling plays a crucial role in determining the performance and stability of conductive materials under operating conditions, especially in systems where both electrical and thermal transport are strongly interdependent.

1.3.3 Electro-Thermal Model for Bulk Materials

Based on the previous considerations, it is evident that, in order to accurately describe the behavior of a material, it is necessary to simultaneously account for its electrical and thermal properties as well as the effects associated with both domains. For this reason, the heat generation term due to the Joule effect is introduced into the thermal balance equation, giving rise to a model capable of accounting for the mutual influence between the electrical and thermal fields. The equation in its general form is the following:

$$\rho c_p \frac{\partial T}{\partial t} = \nabla \cdot (k \nabla T) + q'' + q''' \tag{18}$$

Where ρ is the density of the material, c_p is the specific heat capacity, k is the thermal conductivity, while q'' is the is the volumetric heat generation rate, which, depending on the forcing, while q''' is related to the interaction with the external environment.

The individual contributions are discussed in detail below.

- Density ($\frac{kg}{m^3}$) is a basic property of materials, defined as the ratio between mass and volume;

$$\rho = \frac{m}{V} \tag{19}$$

the knowledge of this parameter is fundamental for correctly modeling the thermal or mechanical behavior of an object.

- The specific heat capacity $[J/(kgK)]$ is formally defined as (20) and represents the amount of heat required for 1 kg of material, at constant pressure, to increase its temperature by 1 K.

$$c_p = \frac{1}{m}\left(\frac{\delta Q}{dT}\right)_p \tag{20}$$

This parameter can be determined either by direct calorimetric measurements or indirectly estimated through experimental approaches that derive its value from other physical tests, and also through theoretical models grounded in microscopic principles. For conventional materials, parameters of this type are often tabulated.

- The thermal conductivity $[W/(mK)]$quantifies the ability of a material to conduct heat and defines the proportionality between the heat flux and the temperature gradient, according to Fourier's law of heat conduction:

$$\mathrm{q} = -\,k\,\nabla T \tag{21}$$

This property expresses how efficiently thermal energy is transferred through the material when a temperature difference

is applied. A high value of $k$indicates that heat can easily flow, while low values correspond to insulating materials.

The thermal conductivity can be determined by direct experimental methods, which measure the heat flux under a controlled temperature gradient, or can be indirectly estimated from other thermal or structural measurements. Various experimental setups are used depending on the material and temperature range, including steady-state methods (e.g., guarded hot plate or heat flow meter) and transient methods (e.g., laser flash analysis). In addition, theoretical or semi-empirical models based on microscopic heat transport mechanisms (such as phonon and electron scattering theories) can be used to estimate k from the material's microstructural and compositional characteristics. For most conventional materials, reference values of thermal conductivity are tabulated as a function of temperature.

- The contribution q'', when heat generation is due to the flow of current in the material, is modeled according to the Joule effect and represents the parameter that couples the electrical model with the thermal one. It is defined on the basis of Ohm's law and can be expressed as follows:

$$q'' = J^2/\sigma \tag{22}$$

The interaction with the environment can take different forms and is modeled using the heat transfer theory, considering the possible heat fluxes observed between the surface of the material and its surroundings. The three main modes of heat transfer are conduction, convection, and radiation.

- When the surface of the object is in physical contact with another body at a lower temperature, the transfer occurs by conduction. The amount of dissipated heat follows Fourier's law (21). By particularizing the equation to consider heat dissipation along a single direction, it becomes (23).

$$q''' = \frac{kA}{\Delta x}(T_2 - T_1) \tag{23}$$

Where k is the thermal conductivity, Δx is the thickness of the body in contact with the heat-exchanging surface (A), and T_1 and T_2 are the temperatures of the body and the surface.

- When heat transfer occurs from the surface to the surrounding fluid, the thermal exchange takes place by convection. If the fluid motion is induced by external components (e.g., fans or pumps), the convection is called forced; if the fluid motion is a consequence of its density variation due to the temperature increase, then the convection is called free or natural.

The convective contribution is expressed through Newton's law (24), written in its general form as:

$$q''' = h(T_s - T_\infty) \tag{24}$$

Where q'' is the heat flux per unit area, h is the heat transfer coefficient, and T_∞ is the temperature of the fluid far away, that is, the temperature of the fluid not in the vicinity of the surface, which is immediately influenced by the surface temperature.

- The heat transfer coefficient $[W/m2]$ thus represents the proportionality factor between the driving thermal gradient and the actual rate of convective heat transfer.

The value of h depends on several factors, including the nature of the fluid (gas or liquid), its thermophysical properties (density, viscosity, specific heat, and thermal conductivity), the type of flow (laminar or turbulent), the relative velocity between the surface and the fluid, and the geometry and orientation of the surface. Because of this complexity, $h$is not a material constant but an effective parameter that must often be evaluated for each specific configuration. In practice, the heat transfer coefficient can be determined experimentally using controlled convection tests, or estimated indirectly through empirical correlations derived from dimensional analysis and experimental data, which express $h$as a function of dimensionless groups such as the Nusselt, Reynolds, and Prandtl numbers. For example, in forced convection over a flat plate, a typical correlation takes the form:

$$Nu = C\,Re^{m}\,Pr^{n} \tag{25}$$

from which h can be obtained as:

$$h = \frac{\mathrm{Nu}\,k_f}{L} \tag{26}$$

where k_f is the thermal conductivity of the fluid and L is a characteristic length of the system. For conventional fluids and flow regimes, reference values and empirical correlations for $h$are commonly tabulated.

- Finally, radiative heat transfer is associated with the emission and absorption of electromagnetic radiation between

the surface and its surroundings, and becomes particularly significant at high temperatures. In this case, q''' is described through Stefan–Boltzmann law, expressed as:

$$q''' = \varepsilon\sigma(T_s^4 - T_\infty^4) \tag{27}$$

where ε is the surface emissivity, σ is the Stefan–Boltzmann constant $[W/(m^2K^4)]$.

- The emissivity, denoted by ε(dimensionless, $0 \leq \varepsilon \leq 1$), quantifies the ability of a real surface to emit thermal radiation compared to that of an ideal blackbody ($\varepsilon = 1$), while real materials, instead, have lower emissivity. Emissivity depends on several factors, including the material composition, surface finish (smooth, rough, or oxidized), temperature, and wavelength of the emitted radiation. For example, polished metals typically exhibit very low emissivity ($\varepsilon \approx 0.02$–0.1), while oxidized or painted surfaces, ceramics, and non-metals can reach much higher values ($\varepsilon \approx 0.8$–0.95).

The emissivity of a material can be measured experimentally using specialized devices such as emissometers or infrared spectrometers, or it can be estimated from empirical correlations and tabulated data available in the literature for standard materials and surface conditions.

1.4 COMSOL Multiphysics Models

The aim of this chapter is to illustrate how COMSOL Multiphysics can be used as a simulation tool for studying electrical and electro-thermal phenomena in multifunctional materials and devices. The approach adopted is deliberately

practical: the emphasis is placed on the computational and modeling choices rather than on pure theoretical analysis, with the goal of providing an operational perspective on the implemented simulation procedures and the rationale behind them.

Numerical simulations play a central role in the context of this work. Rather than a theoretical study, the simulations are designed to complement and support the experimental work. The models developed in COMSOL are calibrated (fitted) using experimental data, in order to estimate physical parameters that are difficult to measure directly (such as electrical conductivity, heat transfer coefficients, or coupled material properties).

Once validated and consolidated on known cases, these models can be used to:

- predict the system's response under operating conditions that have not been experimentally explored or are difficult to reproduce in the laboratory;
- optimize the design of components and materials by varying geometries, boundary conditions, or physical properties in a controlled manner;
- evaluate the interaction between electrical, thermal, and, when necessary, mechanical phenomena within a consistent multiphysics framework.

In this context, the use of COMSOL offers significant advantages compared to other more specialized simulation environments. The wide range of physical modules that can be integrated and the ability to handle complex couplings between different fields make it possible to model multifunctional systems

within a single framework, where electrical and thermal variables are not independent but strongly interconnected.

This approach avoids the need for multiple separate software tools and reduces the risk of inconsistencies between different models, while ensuring greater efficiency in both the development phase and the subsequent analysis of results.

1.4.1 Modeling and Simulation Workflow in COMSOL Multiphysics

In the context of this research activity, the use of COMSOL Multiphysics serves as an analytical and predictive tool based on a coherent workflow that enables the translation of a real physical problem into a numerical model capable of describing its dominant phenomena. The modeling process is not conceived as a simple sequence of technical steps, but rather as an iterative path of interpretation, calibration, and validation, in which the geometric, physical, and numerical choices are driven by the specific requirements of representing the studied system. In Figure 3 a schematic representation of the workflow used to implement a simulation in COMSOL Multiphysics is shown.

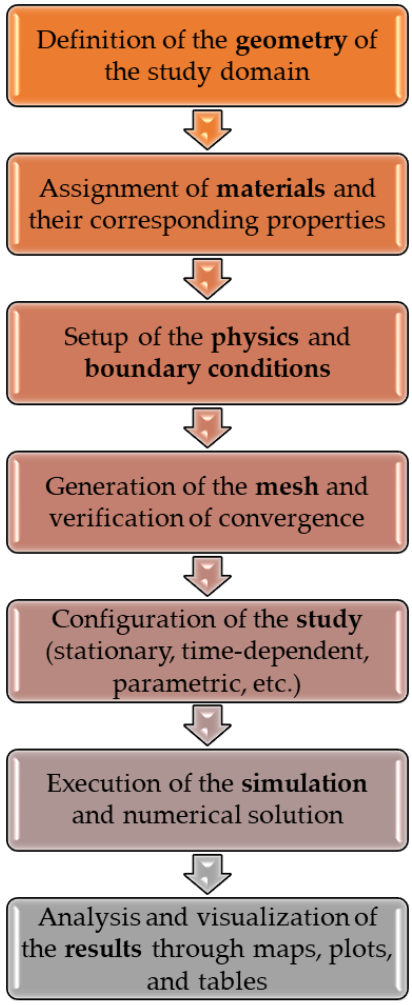

Figure 3. Operational workflow in COMSOL.

Figure 4 shows the COMSOL interface screen, displaying the *Model Builder*, through which all the model settings and parameters can be defined and managed.

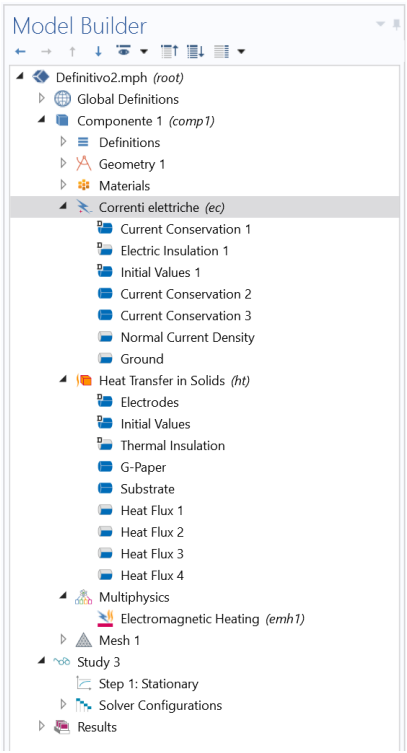

Figure 4. Model Builder interface of COMSOL, showing an example of an electrothermal multiphysics model.

The construction of the model begins with the definition of the geometry of the study domain, which determines how closely the formulated numerical problem reflects the experimental reality.

Depending on the complexity of the phenomenon and the objectives of the simulation, the geometry can be simplified by removing structural details that do not significantly affect the results of interest. It can be represented in two dimensions, providing a simplified but computationally efficient description, or in three dimensions, allowing the capture of the most relevant spatial effects. The choice between a 2D or 3D model, as well as

the possible use of symmetry conditions or geometric reductions, therefore represents a compromise between physical fidelity and computational sustainability.

Once the geometry has been defined, each domain is assigned the corresponding materials and physical properties, which can be either constant or dependent on varying quantities such as temperature. In COMSOL, there is a library of predefined materials, each of which includes a set of standard physical properties already integrated. When the characteristics of the material under investigation are not available in the database, or when a specific behavior needs to be introduced, it is possible to define a custom material by manually specifying the relevant properties and, if necessary, expressing their functional dependence on other physical variables.

This flexibility is particularly important in the study of multifunctional materials, where the interactions between electrical and thermal phenomena require a model capable of accurately describing the local variation of the material properties. Moreover, material parameterization allows for sensitivity analyses and fitting procedures with respect to experimental data, aimed at estimating uncertain parameters and refining the numerical model based on real observations.

The core of the simulation process lies in the definition of the physical interfaces and multiphysics couplings, which make it possible to describe coherently the governing equations of the different physical domains. In electrothermal problems, for instance, the Electric Currents and Heat Transfer in Solids interfaces can be combined through the Joule Heating module, allowing the simultaneous consideration of electrical conduction and heat transfer due to the Joule effect. This coupling enables a

realistic representation of energy dissipation processes and the resulting thermal effects.

Once the most appropriate modules for the specific case have been selected, a fundamental step is the definition of the boundary conditions, which determine the behavior of the system at the limits of the computational domain. In practice, they allow the model to represent the interactions with the external environment, for example by imposing an electric potential, a fixed temperature, or a heat flux. Their proper definition is essential to ensure that the simulation reproduces the operating conditions of the real system in a physically consistent manner.

The discretization phase, carried out through the Finite Element Method (FEM), represents a crucial step in the numerical modeling process, as it allows the continuous domain of the physical problem to be converted into a discrete representation composed of a finite set of elements. Within each element, the field variables are approximated using predefined shape functions, and the differential equations describing the phenomenon are thus transformed into an algebraic system that can be solved numerically. For example, a function u, that may be the dependent variable in a PDE (i.e., temperature, electric potential, etc.), an be approximated by a function u_h using linear combinations of basis functions according to the following expressions:

$$u \approx u_h \tag{28}$$

and

$$u_h = \sum_i u_i \psi_i \tag{29}$$

Where ψ_i are the basis functions and u_i are the coefficients of the functions that approximate u with u_h.

The definition of the mesh, that is the spatial discretization of the domain, has a direct influence on both the accuracy of the results and the computational efficiency of the model. A mesh that is too coarse may fail to properly capture the local variations of the physical fields, leading to significant errors in the estimation of the quantities of interest; conversely, an excessively fine mesh increases the number of degrees of freedom of the system and, consequently, the computation time. The optimal choice of discretization therefore represents a compromise between accuracy and computational speed.

In COMSOL Multiphysics, mesh generation can be performed either automatically, through the physics-controlled mesh option, which adjusts the mesh density according to the selected physics, or manually, by specifying the size and spatial distribution of the elements within the different domains.

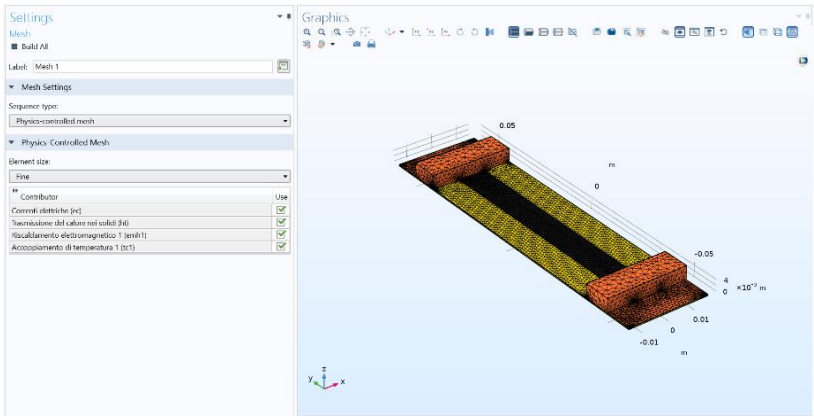

Figure 5. COMSOL interface showing the mesh settings and visualization of the resulting mesh applied to the CAD geometry under analysis.

A fundamental aspect of this phase is the mesh assessment. This procedure involves performing multiple simulations with progressively finer levels of discretization and evaluating how the quantities of interest vary with the element size. When the difference between two consecutive solutions becomes negligible, the mesh can be considered sufficiently refined. This type of analysis is essential to ensure the reliability of the results and to avoid numerical errors.

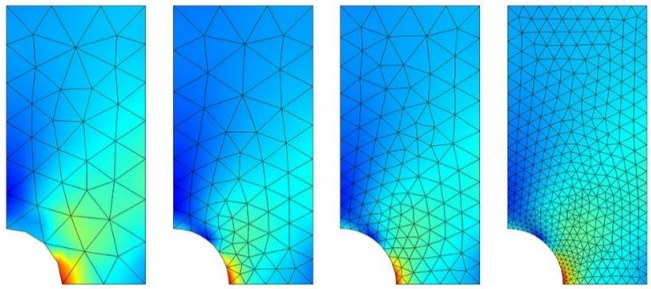

Figure 6. Example of mesh refinement in COMSOL (https://doc.comsol.com, accessed on September 27, 2025).

Once the model has been completed, the next step is the definition of the type of study to be performed. If the goal is to analyze the system behavior once it has reached its steady-state condition, a stationary study is defined. Conversely, if the aim is to observe the time evolution of the quantities under investigation, a time-dependent (transient) study must be set up. Alternatively, or in combination with these, a parametric analysis can be performed to evaluate how the system's response varies with changes in one or more model parameter (such as physical quantities, material properties, or geometric dimensions) in order to assess the system's sensitivity.

Finally, the result analysis phase allows the obtained data to be visualized in different ways depending on the purpose of the study. The results can be displayed in tables to extract numerical values, in graphs and profiles to observe the variation of quantities over time or along specific directions, or as two- and three-dimensional field maps, which provide spatial distribution view of the main physical variables related to the module used for the analysis.

Figure 7 shows an example of the result of a multiphysics simulation coupling the electrical and thermal modules, enabling the prediction of the surface temperature distribution reached by the object under analysis as a result of Joule heating.

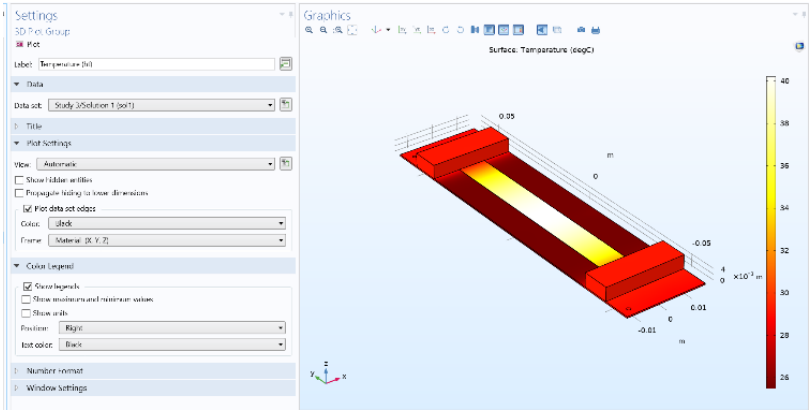

Figure 7. COMSOL interface showing the temperature field on the surface of the object under analysis, obtained from an electrothermal multiphysics simulation.

1.4.2 Electrical and Thermal Module in COMSOL Multiphysics

During this thesis work, two main modules belonging to the physics interfaces of COMSOL Multiphysics were used. For the modeling of the electrical part, the AC/DC module was employed, both in the section dedicated to Electric Currents and in the one related to Electrostatics phenomena. For the thermal part, the Heat Transfer in Solids module was used, which was then coupled with the electrical physics to take into account the mutual influences between electrical and thermal parameters, in particular the Joule effect and the related dissipation phenomena.

AC/DC Module

The *AC/DC Module* of COMSOL Multiphysics provides a comprehensive environment for the numerical modeling of

electric and magnetic fields under static, low-frequency, or transient conditions.

Simulations performed with this module are based on Maxwell's equations, which form the fundamental basis for describing electromagnetic phenomena. Depending on the type of analysis, the module either solves the full set of Maxwell's equations or applies simplified formulations consistent with the assumptions of stationary or quasi-stationary regimes.

The complete equations are:

$$\nabla \cdot \boldsymbol{D} = \rho$$

$$\nabla \cdot \boldsymbol{B} = 0$$

$$\nabla \times \boldsymbol{E} = -\frac{\partial \boldsymbol{B}}{\partial t} \tag{30}$$

$$\nabla \times \boldsymbol{H} = \boldsymbol{J} + \frac{\partial \boldsymbol{D}}{\partial t}$$

where E and H represent the electric and magnetic fields, respectively, D and B are the electric displacement and magnetic flux density vectors, ρ is the free charge density, and J is the current density.

These quantities are linked to the material properties through constitutive relations:

$$\boldsymbol{D} = \varepsilon \boldsymbol{E}, \qquad \boldsymbol{B} = \mu \boldsymbol{H}, \qquad \boldsymbol{J} = \sigma \boldsymbol{E} \tag{31}$$

where ε, μ, and σ denote the electric permittivity, magnetic permeability, and electrical conductivity of the material, respectively. These relations take a linear form in the case of homogeneous and isotropic materials, but nonlinear or

anisotropic behaviors can also be introduced, as well as spatial and temporal variations of the material properties.

Depending on the operating regime, the module can apply different approximations of Maxwell's equations. According to these approximations, different physics interfaces are available within the software, such as *Electrostatics* or *Electric Currents* (https://doc.comsol.com, accessed on September 27, 2025).

Heat Transfer Module

The Heat Transfer Module of COMSOL Multiphysics provides a comprehensive environment for the numerical modeling of heat transport phenomena under stationary or transient conditions. Simulations performed with this module are based on the principles of energy conservation, which describe heat conduction, convection, and radiation within and between solids, fluids, and gases. Depending on the selected physical assumptions, the module can solve the full heat transfer equation or apply simplified formulations suitable for steady-state or quasi-steady-state analyses.

The general form of the heat transfer equation is given by:

$$\rho\, c_p\, \frac{\partial T}{\partial t} = \nabla \cdot (k\, \nabla T) + Q \tag{32}$$

where ρ is the material density, $c_p$the specific heat capacity, $k$the thermal conductivity, $T$the temperature field, and Qrepresents internal heat sources such as Joule heating or chemical reactions. Additional terms can be included to account for convective heat transfer in fluids, radiative exchange between surfaces, and phase change phenomena.

These quantities are linked to the material's thermophysical properties, which can vary spatially and temporally or exhibit nonlinear behavior depending on temperature and other field variables.

Depending on the physical regime and the phenomena of interest, the module applies different formulations of the heat transfer equations.

According to these formulations, several dedicated physics interfaces are available within the software, such as *Heat Transfer in Solids* or *Heat Transfer in Fluids* (https://doc.comsol.com, accessed on September 27, 2025).

CHAPTER 2
Fabrication and Characterization of GNP-Based Industrial Materials

Graphene exhibits remarkable electrical, thermal, and mechanical properties, which make it an attractive material for industrial, aerospace, and biomedical applications.

The use of materials produced on an industrial scale, as opposed to those synthesized in laboratory environments, is of strategic importance from both a technological and an economic perspective. Laboratory-scale production is subjected to several limitations: complex and often non-optimized processes, high synthesis costs, difficulties in large-scale reproducibility, and issues related to batch stability. These critical aspects make the use of "lab-made" materials not always sustainable when moving from preliminary research to industrial applications.

By contrast, industrial-grade materials are generally the outcome of consolidated and optimized processes, capable of ensuring uniformity, reliability, and availability at competitive costs. The standardization of production procedures also helps reduce critical variables, improve the overall quality of the product, and enhance compatibility with existing manufacturing technologies. From an economic standpoint, adopting industrially produced materials enables the reduction of both procurement and processing costs, thereby facilitating the transition from laboratory research to large-scale production.

In this chapter, the focus will be on the fabrication of GNP-based composite strips obtained from thin sheets produced through an industrial process and their electro-thermal characterization. This type of study is essential to highlight the properties of the investigated materials, with the aim of assessing and integrating them into different kinds of industrial applications.

2.1 Fabrication of Nanomaterials

Although it exhibits outstanding properties, graphene does not exist in nature as an isolated material but rather as the fundamental structural unit of graphite, where it constitutes the elementary two-dimensional layer. In graphite, individual graphene sheets are stacked and held together by weak Van der Waals interactions, which prevent the spontaneous occurrence of graphene in a free-standing form. To obtain graphene suitable for technological and scientific applications, it is therefore necessary to employ controlled laboratory processes. These methods are typically categorized as either top-down or bottom-up approaches: in the former, graphene is extracted from bulk graphite, whereas in the latter it is synthesized directly through dedicated growth techniques. The most widely adopted fabrication strategies include graphite exfoliation, chemical vapor deposition (CVD), and epitaxial growth on suitable substrates.

Graphite exfoliation is a top-down technique, in which graphene is isolated by overcoming the Van der Waals interactions between adjacent layers of the graphite. Another approach involves immersing the material in a liquid medium. In

this case, the potential energy between adjacent layers is significantly reduced in the presence of a solvent compared to vacuum. Exfoliation can also be promoted by applying external forces strong enough to overcome these attractive interactions. Commonly employed techniques include ultrasonication and thermal treatment. During ultrasonication, shear forces and cavitation phenomena - arising from the growth and collapse of micrometer-sized bubbles - act on the bulk material, thereby inducing layer separation. In the thermal processing of graphite oxide and graphite intercalation compounds, the pressure generated by the decomposition of functional groups and intercalated species between layers exceeds the van der Waals attractions, ultimately leading to exfoliation (Cai, 2012).

To reduce the attraction, it is possible to increase the distance between two layers using oxidation, chemical intercalating reactions or even perform exfoliation using adhesive tape.

Among the bottom-up techniques there is Chemical vapor deposition (CVD), used for the growth of thin films of materials. In the specific case of graphene, the process takes place in a reaction chamber where gases such as methane, which provides the carbon atoms, and hydrogen, which plays a supporting role in controlling the reaction, are introduced. The substrate, generally made of metals such as copper or nickel, is heated to very high temperatures, in the range of 900–1050 °C. Under these conditions, methane decomposes and the released carbon atoms deposit on the metal surface, self-organizing into a two-dimensional graphene lattice. Once the growth is complete, the system is cooled and the obtained graphene can be transferred onto other supports, such as silicon or glass, to be integrated in specific devices.

The technological complexity of graphene fabrication methods, combined with the challenges in reproducing the material and integrating it into devices or larger systems, has led to the search for solutions that make it possible to exploit the properties of the nanomaterial while simplifying production and making it feasible on an industrial scale.

An analysis of different low-cost graphene derivatives, considering both cost and performance, can be found in (Kovtun, 2019). The study highlights that materials based on graphene nanoplatelets (GNPs) provide a promising compromise, offering good physical properties, industrial scalability, and reasonable production costs.

GNPs consist of irregular flakes of few-layer graphene (Jiménez-Suárez, 2020) and can be produced through several scalable techniques that operate through distinct mechanisms. wet-jet milling. Microwave irradiation (Dabrowska, 2014; Maffucci, 2016) is a technique in which graphite or graphene oxide is rapidly heated by microwave energy, leading to a sudden thermal expansion that causes the exfoliation of graphene layers. In ball milling (Zhang, 2016), the material is subjected to repeated impacts and shear forces generated by the motion of balls inside a rotating chamber, which progressively break down graphite particles and delaminate the sheets. While in wet-jet milling (Malik, 2020) instead, relies on dispersing graphite in a liquid medium that is forced at very high pressure through micro-nozzles, where intense shear forces separate the stacked layers into thinner platelets.

2.1.1 Materials Under Test

The materials analyzed in this work are nanocomposite films based on GNPs, produced by Nanesa S.r.l. Their fabrication process follows a standardized industrial protocol to ensure reproducibility and to obtain the desired electrical, thermal, and mechanical properties. The tailoring of these properties is achieved by selecting the type of material combined with the GNPs and by adjusting the relative proportions of the two constituents.

The production process begins with a low-cost graphitic precursor, namely intercalated expandable graphite. The synthesis of the GNPs follows an industrial three-step process: thermal expansion, liquid exfoliation, and final sonication. During thermal expansion, the intercalated graphite is rapidly heated, causing the layered structure to expand and weaken the interlayer bonds. Liquid exfoliation then disperses the expanded graphite in a suitable solvent, promoting the separation of individual flakes. Finally, sonication applies ultrasonic energy to further delaminate the material, yielding few-layer graphene nanoplatelets with improved uniformity.

The morphology of the GNPs strongly influences the properties of the final product. Thinner GNPs have been demonstrated to enhance both mechanical and thermal performance, while changes in the size/thickness aspect ratio significantly influence the electrical percolation threshold. Furthermore, larger lateral dimensions and higher surface areas are generally correlated with improved electrical conductivity. Therefore, maintaining strict control over GNP dimensions is necessary to ensure consistent film behavior. In this case, the

GNPs employed exhibit an average lateral size of 30 ± 5 μm and an average thickness of 12 ± 3 nm, values that reflect the stability of the industrial production process.

In Figure 8 a SEM (Scanning Electron Microscope) image of a single GNP is shown.

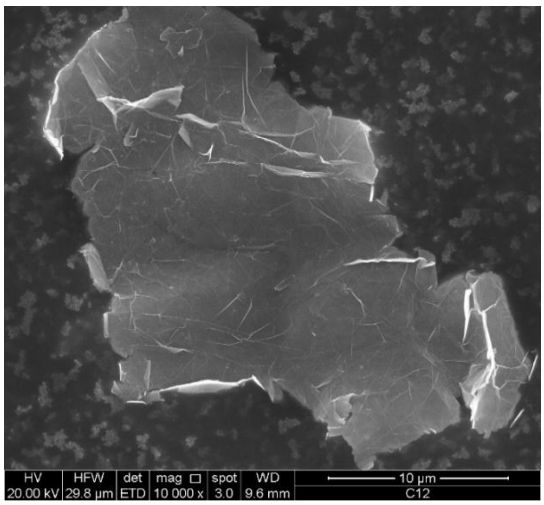

Figure 8. Scanning Electron Microscope image of a single flake of GNP (Lahbacha, 2022).

Subsequently, the controlled fabrication process adopted by Nanesa s.r.l. also consists of several steps:

- First, a mixture is formulated by dispersing GNP particles in a solvent (either acetone or an aqueous solution), assisted by magnetic stirring and a final sonication step. When required, a polymeric binder is introduced during the sonication stage.

- Second, the mixture is deposited by means of a customized semi-automatic spraying system, based on a Computer Numeric Control (CNC) plotter (EXTREMA CNC,

model Basic, working area 400 × 600 × 100 mm) combined with a full-cone air spray nozzle (NCS). The spraying operation is performed at controlled pressure, with the possibility of using either solvent-based or aqueous dispersions, and ensures accurate deposition through a 3-axes pantograph.

- Finally, a controlled calendering step, optionally combined with annealing, is carried out to compact the deposited layers, optimize thickness, and improve the alignment of the GNPs within the structure.

The resulting graphene sheets are freestanding, paper-like materials, consisting of highly oriented nanometric GNPs with a very high reinforcement content.

The Raman spectrum of the industrial material is shown in **Figure 9**, from which it can be seen that the material exhibits a low defect density.

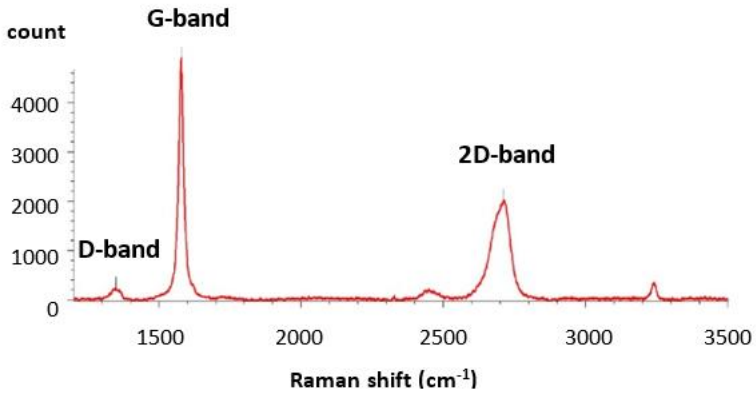

Figure 9. Raman spectroscopy characterization of the GNPs, highlighting a low intensity of the D band and a high intensity of the G band (Sibilia, 2021).

Different composite formulations were prepared for this study. They differ in both the percentages and the types of binder. The resulting sheets exhibited different thicknesses, and some of them was subjected to subsequent heat treatments at different temperatures. Their main characteristics are presented in Table 1.

Table 1. Composition of the materials under test.

Material	GNP %	Binder	Annealing T [°C]
G-paper	100	-	-
G-Preg (95/5)	95	Polyurethane	200
G-Preg (80/20)	80	Polyurethane	200
G-Preg (70/30)	70	Epoxy resin	180
G-Preg (50/50)	50	Boron nitride	150
G-Preg (30/70)	30	Boron nitride	150
G-Preg (25/65-10)	25	Boron nitride-Epoxy resin	180

The industrial graphene films obtained through this method were prepared in the form of strips (Figure 10), with lateral dimensions of 1 cm, lengths ranging from 10 to 18 cm and having a thickness in the range of 50-100 μm. This form allows the material to be properly characterized, while maintaining dimensions suitable for potential applications that will be presented later.

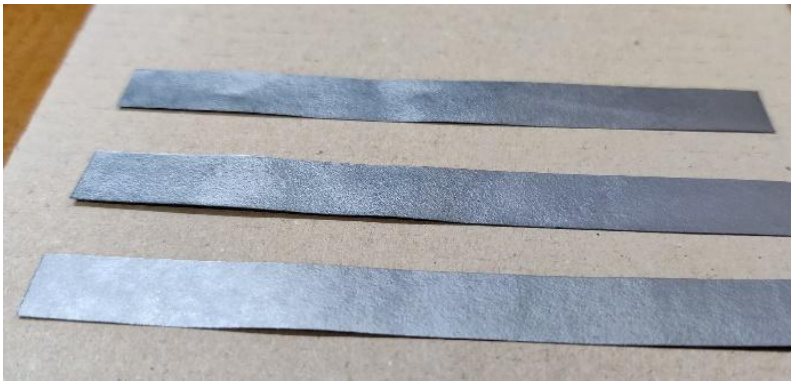

Figure 10. Nanocomposite strips derived from macroscopic graphene nanoplatelet sheets (Giovinco, 2023).

2.2 Electrical Characterization

The electrical characterization was carried out with the aim of determining how the resistivity of the tested materials varies with temperature, starting from experimental measurements of electrical resistance. To ensure the reliability of the results, a series of preliminary tests were first performed. These included verifying the linearity of the voltage–current (V–I) relationship to confirm the ohmic behavior of the materials, and conducting specific measurements on the custom-designed test fixture to evaluate possible additional contact resistances that could influence the accuracy of the main measurements.

Once the setup and measurement procedure were validated, resistance measurements as a function of temperature were performed, allowing the R–T behavior of each sample to be obtained. From this trend, the Temperature Coefficient of Resistance (TCR) was then calculated for each material. Finally, a

3D numerical model was developed to support the analysis, enabling the optimization of the resistivity estimation process and providing a useful comparison with the experimental data.

2.2.1 Voltamperometric Method

In the context of electrical characterization of materials, the measurement of resistance represents a fundamental step. It finds expression in the macroscopic form of Ohm's law, which, under constant physical conditions (e.g., fixed temperature and mechanical stress) and assuming a linear medium, establishes that the potential difference (V) across a conductor is proportional to the current (I) flowing through it:

$$V = RI \tag{33}$$

where R is the proportionality constant, namely the electrical resistance.

Based on this principle, resistance can be determined from the ratio of voltage to current. However, these quantities are not simultaneously known a priori. In practice, one of them may be imposed, while the other is measured using appropriate instruments such as a voltmeter and an ammeter.

To carry out the measurement, two standard configurations are commonly adopted:

Voltmeter connecter before the ammeter, in which the ammeter is placed in series with the resistor under test and the voltmeter is connected in parallel across both the resistor and the ammeter. It is commonly employed when the resistance of the sample is significantly higher than that of the voltmeter.

Ammeter connected before the voltmeter, in which the voltmeter is connected directly across the resistor under test, while the ammeter measures the current flowing into both the resistor and the voltmeter. It is commonly employed when the resistance of the sample is significantly lower than that of the voltmeter.

Once the resistance is determined, the electrical resistivity (ρ) (a material-specific parameter that is independent of geometrical dimensions at the macroscale) can be analytically obtained. In its simplest form, resistance is modeled as directly proportional to the conductor length l and inversely proportional to its cross-sectional area (wh):

$$R = \rho \frac{l}{wh} \tag{34}$$

Experimentally, two main approaches are employed for resistance measurements: the two-probe technique and the four-probe technique (Figure 11).

The two-probe method is among the most widely adopted techniques, particularly suited for samples with relatively high resistance. The principle is simple: both the voltage drop across the specimen and the current through it are measured, and the resistance is then determined from equation (34).

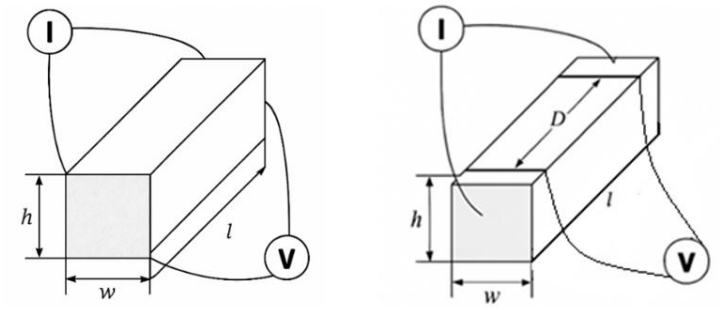

Figure 11. Schematic of two prove (left) and four-prove (right) measurement method.

The four-probe method is instead the preferred choice for low-resistance samples, where accuracy is critical. In this configuration, a known current is injected through the outer contacts, located at the extremities of the sample, while the potential difference is measured exclusively across the inner contacts. The resistance can then be expressed as:

$$R = \rho \frac{D}{wh} \tag{35}$$

where D represents the spacing between the inner voltage probes, rather than the overall length of the specimen. By decoupling current injection and voltage measurement, this technique effectively eliminates the influence of contact resistance between the electrodes and the material, thus enabling highly accurate low-resistance characterization (Singh, 2013).

2.2.2 Experimental Set-up

In order to accurately carry out electrical and electro-thermal characterization (i.e., resistance variation as a function of ambient temperature), a dedicated fixture was designed and manufactured (Figure 12). It was specifically designed to enable resistance measurements either through a two-probe configuration, where the voltage probes coincide with the current electrodes, or through a four-probe configuration, employing dedicated voltage electrodes. In the latter case, the voltage probes could be positioned at different spacings along the sample, allowing the estimation and subtraction of contact resistance, a factor that can significantly influence measurements at carbon interconnect/conventional electrode interfaces (Todri-Sanial, 2016) Furthermore, for shorter strips a dedicated version of the fixture was adopted, featuring only two voltage contacts.

To obtain the V-I characteristic, the full set-up includes a power supply to choose the current value and ensure that it is maintained constant during the whole test by means of the current control option, and a multimeter to measure the voltage drop across the voltmetric contacts.

To measure the resistance at different ambient temperatures, the full set-up includes a multimeter set for 4-wire acquisition and a climatic chamber to control the temperature value and the humidity percentage in the environment (Figure 13).

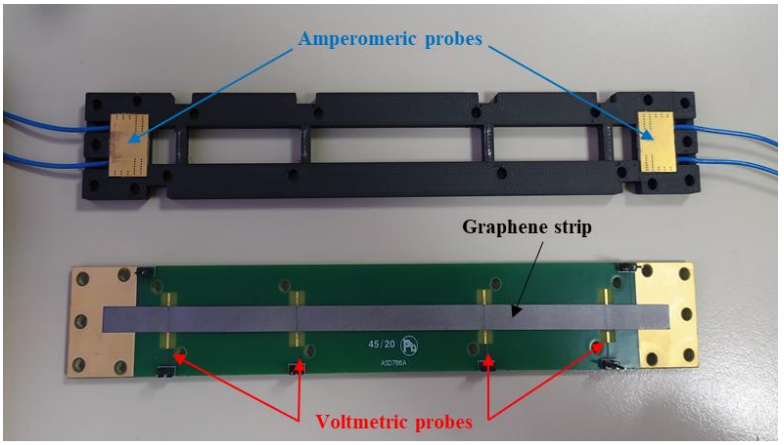

Figure 12. The text-fixture realized for the electro-thermal characterization, with a 2- or 4-probe measurement of the electrical resistance (Lahbacha, 2022).

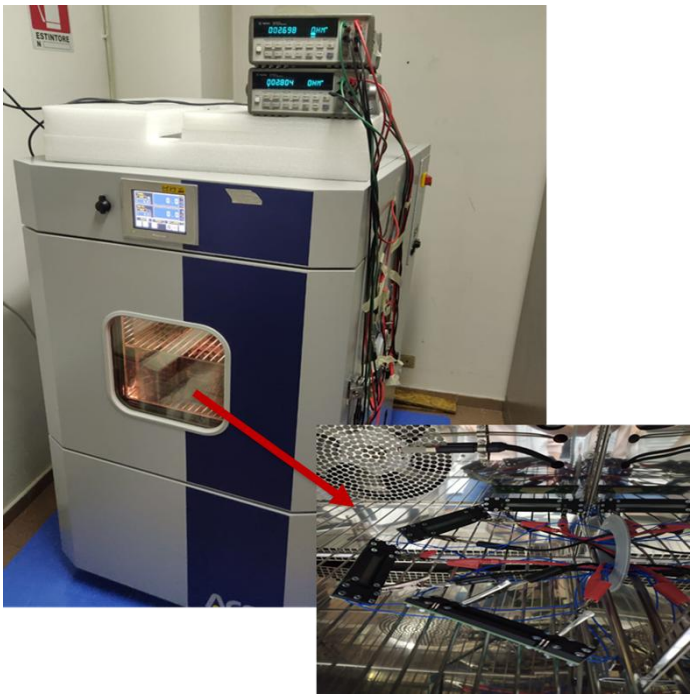

Figure 13. Full set-up for the measure of the resistance at different environmental temperature.

2.2.3 Preliminary Tests

A preliminary electrical characterization was carried out (Sibilia, 2021) at uncontrolled room temperature with several objectives: verifying the correct operation of the experimental setup, estimating the contact resistance contributions, assessing the repeatability and reproducibility of the measurements, checking the linearity of the V-I characteristic. The four-probe technique enabled the determination of the resistance in DC conditions, already corrected for the contribution of the contact resistance between the graphene strip and the copper amperometric electrodes. The measured resistance can be model as follows:

$$R_m = \frac{\rho_m}{S} \cdot L_v + R_c \tag{36}$$

Given the dimensions of the graphene strips, the impact of the contact resistance R_c. due to the voltmetric contacts is not expected to be significant, but this assumption has been experimentally verified. The voltage drop was measured directly onto the strip at different distances and the contact resistance was estimated by Generalised Least Squares algorithm. The value was found to be of the order of mΩ, whereas the resistance of the strip is of the order of Ω.

The resistance was measured 10 times on the same sample and by testing 7 different strips made of the same material in order to evaluate repeatability and reproducibility. The corresponding average values and standard deviations are reported in Table *2*, confirming a high level of repeatability and reproducibility.

Table 2. Estimated values of the contact resistance at room temperature.

Material	Repeatability		Reproducibility	
	R_{AV} (Ω)	STD (Ω)	R_{AV} (Ω)	STD (Ω)
G-paper	1.085	0.002	1.155	0.045
G-Preg (95/5)	2.162	0.001	2.214	0.223
G- Preg (70/30)	2.660	0.004	2.720	0.065

The linearity of the V-I characteristic was verified by measuring the voltage drop while the injected current. The current range analysed was from 10 mA to 500 mA or 1 A according to the material formulation, in order to achieve the Joule heating effect without deteriorate the material. In Figure 14 is reported the response of pure G-paper; the linear response is performed by all the samples.

Finally, in-plane resistivity isotropy was confirmed by room-temperature measurements of G-paper. The test was performed on two sample strips of identical dimensions, cut from the same sheet of material but oriented along two orthogonal directions. The results showed a variation in resistance below 1% (Sibilia, 2021).

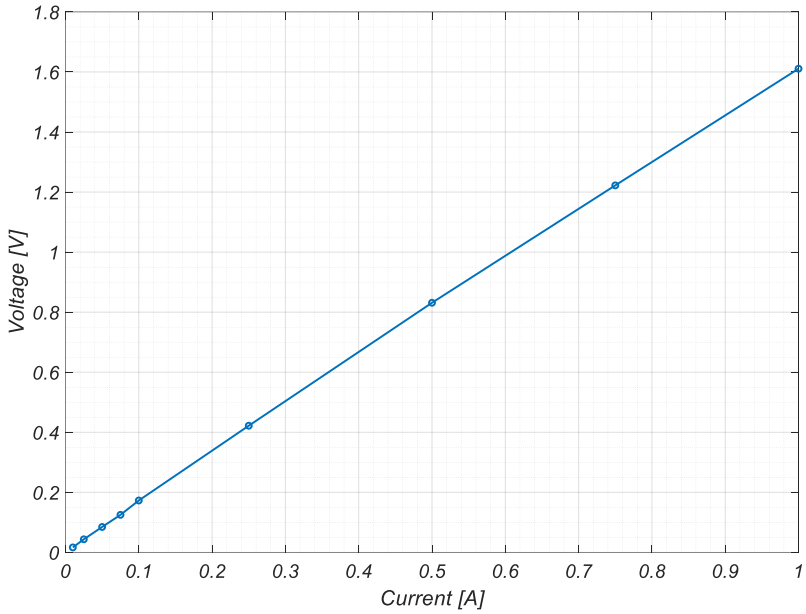

Figure 14. Linear V-I response at room temperature, for G-paper.

2.2.4 Resistance–Temperature Characterization

The electrical resistance of the samples was measured in a wide temperature range, which was from -40 °C up to +60 °C. A complete thermal cycle was performed, consisting of two phases: in the first, the resistance was measured while the temperature was decreased, whereas in the second, measurements were repeated during the heating phase. The resistance was measured with temperature steps of 20 °C.

At each step, the measurement was taken after the climatic chamber had reached thermal equilibrium, which typically required 20–30 minutes. This procedure ensured reliable and reproducible measurements and allowed the evaluation of possible hysteresis effects, by comparing the resistance values measured at the same temperatures during the cooling and heating phases. In Figure 15 is reported the R-T characteristic for a G-Paper sample.

Repeated measurements were found to be stable after thermal equilibrium was reached, and the hysteresis between heating and cooling cycles was negligible. Overall, the material exhibits a Negative Temperature Coefficient (NTC) behavior. Same results were observed for the other tested materials.

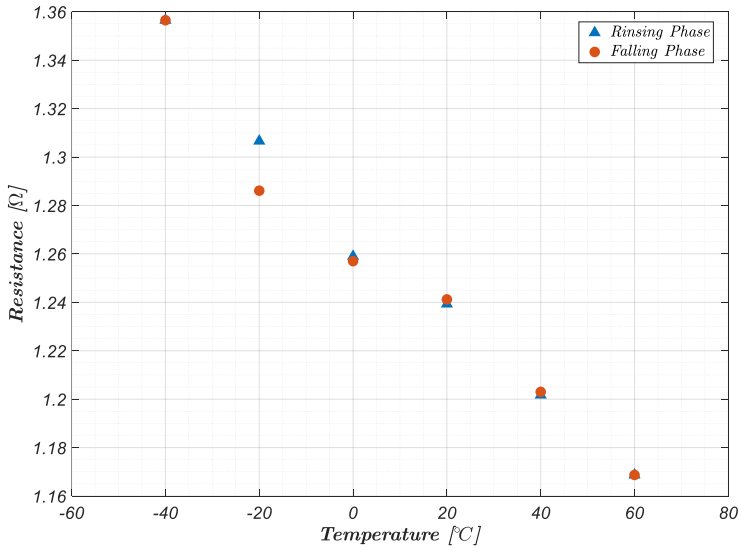

Figure 15. Electrical resistance measured when the temperature is cycling between -40 and +60 °C.

2.2.5 Numerical Model

The modeling of the graphene strip's electrical resistivity was carried out by comparing the experimental resistance measurements with the results of a three-dimensional electro-thermal model implemented in COMSOL Multiphysics. Figure 16. reports the computational domain adopted for the simulations, which includes both the test board and the graphene nanoplatelet (GNP) strip.

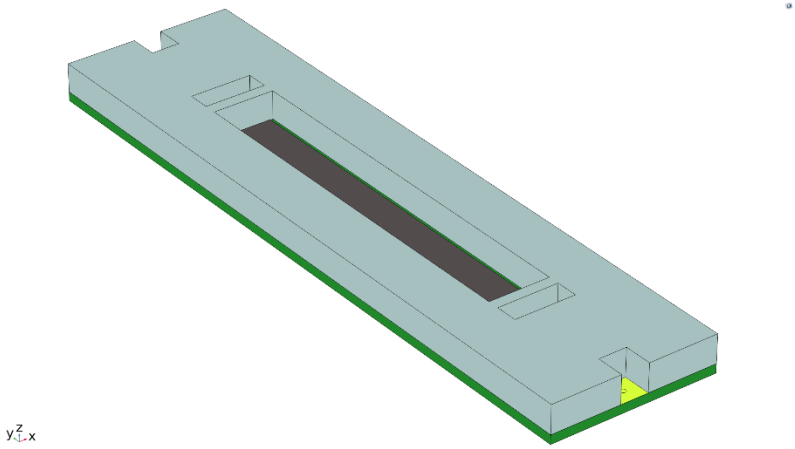

Figure 16. 3D CAD model of the strip including the test fixture used to model the electrical resistance of the material.

The model calculates both the distribution of temperature, $T(\boldsymbol{r}, t)$, and the electric potential, $V(\boldsymbol{r}, t)$, as they change over time and space. These two fields are closely linked: the local temperature influences the resistivity of the material, and this, in turn, affects the amount of Joule heating produced by the current. The mathematical description is based on the Fourier equation for

heat conduction, coupled with the Poisson equation for the electric potential:

$$C_{TH}(T)\frac{\partial T(\boldsymbol{r},t)}{\partial t} = \nabla\kappa(T)\nabla T(\boldsymbol{r},t) + F(\boldsymbol{r},T), \tag{37}$$

$$\nabla^2 V(\boldsymbol{r},t) = 0 \tag{38}$$

Here, κ is the thermal conductivity and C_{TH} the heat capacity of the material, while equation (3) has been written in a region without electrical sources. The coupling term F represents the heat generated inside the strip by the Joule effect and is expressed as:

$$F(\boldsymbol{r},T) = \rho(\boldsymbol{r},T)J^2(\boldsymbol{r},t), \tag{39}$$

where $J(\boldsymbol{r},t)$ is the current density.

The system of equations (37)–(39) was solved numerically using the finite element method. An adaptive tetrahedral mesh was used for the simulations. The regular geometry of the structure makes the choice of the mesh element type not particularly critical, although a refinement of the mesh around the graphene strip was applied in order to obtain more accurate results for the temperature and potential fields.

The purpose of this numerical model is to combine its result with the experimental measurements to extract an equivalent, homogeneous resistivity that can represent the whole graphene strip. In principle, resistivity should be described by a tensor:

$$\boldsymbol{\rho}(T) = \mathrm{diag}\left[\rho_{xx}(T), \rho_{yy}(T), \rho_{zz}(T)\right] \tag{40}$$

where ρ_{xx} and ρ_{yy} are the in-plane components and ρ_{zz} is the out-of-plane one. Since with this geometry the current flows almost entirely in-plane, and since it was experimentally verified that the two in-plane contributions ca be considered equal (Sibilia, 2021), the tensor form can be simplified to a scalar resistivity. This simplification makes the analysis easier and does not introduce significant errors, while still allowing a reliable comparison between simulation and experiments.

Implementation with Electric Current interface

The implementation was made using the interface named Electric Currents, which extends the analysis to cases where charges can move and generate current.

In this work, it was used in its stationary (DC) formulation, where, in addition to the electric potential equation, the current conservation equation and the constitutive relation describing the nature of the current in the system are also included in the solution.

$$\begin{aligned} \nabla \cdot \boldsymbol{J} &= Q_{j,v} \\ \boldsymbol{J} &= \sigma \boldsymbol{E} + \boldsymbol{J}_e \\ \boldsymbol{E} &= -\nabla V \end{aligned} \tag{41}$$

The models developed with this interface were used for the optimization of the electrical properties of the materials investigated as electric heaters. In particular, the electrical conductivity was experimentally determined at different ambient temperatures. During the simulation phase, in order to reduce the

computational load, the variation in ambient temperature was accounted for through the contact resistivity, which was calculated analytically outside the model and implemented in COMSOL with its updated value. In the second phase of the study, the thermal transient triggered by the Joule effect was also investigated. In this case, the electrical model was coupled with the thermal model through the Heat Transfer Module; in particular, the Heat Transfer in Solids interface was used in combination with the multiphysics coupling for Joule heating. Since the purpose of the model is to analyze and predict the thermal evolution over time following the application of a known electric current, a time-dependent study was carried out.

$$\rho c_p \boldsymbol{u} \cdot \nabla T + \nabla \cdot \boldsymbol{q} = Q + Q_e$$

$$\boldsymbol{q} = -k \nabla T \tag{42}$$

$$Q_e = \boldsymbol{J} \cdot \boldsymbol{E}$$

The coupling between the two physics interfaces arises from the term Q_e, which represents the heat source generated by the Joule effect within the material.

In the analyzed case study, the surface temperature is influenced by the heat generation due to the Joule effect, but it also depends on the thermal interaction with the surrounding environment and on natural convection heat losses, which are inevitably present since the system is not adiabatic. To accurately simulate this phenomenon, it would be necessary to include the Heat Transfer in Fluids interface, which would allow the explicit modeling of air motion and convective heat exchange. However,

this approach would lead to a more complex model, requiring knowledge of several fluid parameters, and would also result in a significant increase in the computational cost of the simulation.

Since the main interest lies in the surface temperature of the component, the model was simplified by considering only heat transfer in solids, while applying to the surfaces exposed to the environment an equivalent heat flux that accounts for dissipative heat losses. In particular, both convective heat transfer, by estimating an appropriate heat transfer coefficient, and radiative exchange, by defining the material emissivity, were considered, following the methodology described after.

Finally, another important aspect to consider, with the aim of optimizing the computational cost of the model, concerns the choice of the solver. The default solver used by COMSOL is based on the segregated method, in which the different equations describing the involved physics are solved sequentially, dividing the variables into blocks that are updated one at a time until overall convergence is reached. This approach reduces the memory requirements and lightens the computational load at each iteration, making it suitable for large models or for problems characterized by weak couplings between the physical fields. However, when the interactions between variables are particularly strong, the segregated method may fail to converge or require an excessive number of iterations to reach a stable solution. In such cases, it is more effective to adopt a fully coupled approach, which solves all equations simultaneously, directly accounting for the interdependencies among variables. This method generally provides greater robustness and stability, although it demands higher computational resources, especially in the case of complex three-dimensional models.

To practically implement the model, once the geometry is defined, the material properties assigned to the different domains must be specified. An insulating material is considered for both the substrate below the strip and the upper mask, while the electrical and thermal properties of copper are attributed to the contacts. For the nanocomposite strip, an initial resistivity value is set based on analytical calculations (43) derived from the experimentally measured resistance under the considered environmental conditions.

$$\rho = R\frac{S}{l} \tag{43}$$

The model is initially used to optimize the estimation of the material resistivity starting from the values obtained through resistance characterization as a function of temperature. For this purpose, the simulation is implemented in such a way as to reproduce the experimental conditions. At first, the model is considered only from an electrical point of view, and the influence of the ambient temperature is taken into account by knowing the temperature coefficient (α) and calculating the resistivity of the materials through equation:

$$\rho(T) = \rho_0(1 + \alpha(T - T_0)) \tag{44}$$

Boundary conditions are applied to the domains representing the contacts at the ends of the strip: on one side, a current density is imposed, while on the opposite side a zero potential is set.

In the simulation, a parametric sweep is performed on the parameter describing the strip material resistivity. The numerical resistance is then calculated by extracting the potential difference

across the strip from the numerical results and dividing it by the imposed current.

2.2.6 Optimization Procedure and Linear Model of Resistivity

The results of numerical simulations are used to evaluate the resistance of the sample related to each value of resistivity considered during the parametric sweep (repeated for every environmental temperature analyzed). The simulated resistance (R_s) is compared with the experimental resistance, and the mean square error (MSE) is computed.

$$MSE(\rho_{eq,n}) = \sqrt{\sum_{k=1}^{n} \left(R_m(T_i) - R_s(\rho_{eq,k}, T_i)\right)^2} \tag{45}$$

where n is the number of samples chosen for the numerical simulation.

This procedure yields a curve (for each environmental temperature) representing the error as a function of resistivity; the minimum of this curve is selected as the optimized resistivity value. If the minimum error turns out to be significant, the procedure can be made iterative by progressively narrowing the resistivity range around the identified minimum. In Figure 17, the curve obtained for G-paper at 20°C is presented.

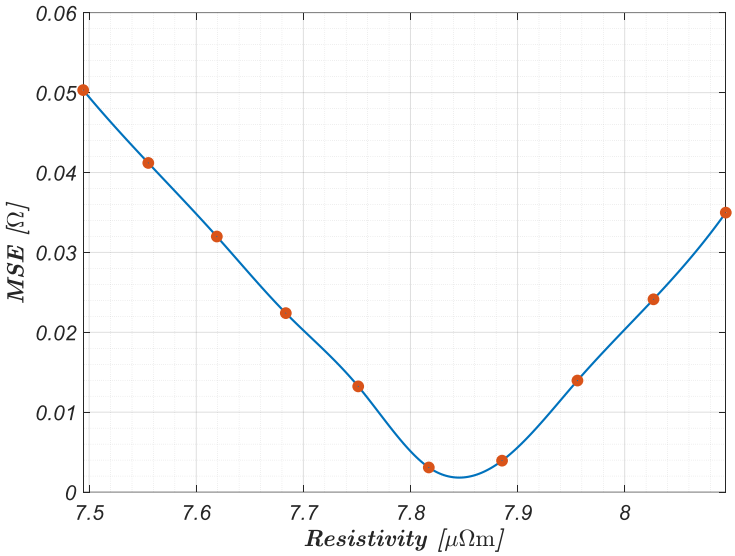

Figure 17. Mean Square Error for G-paper at 20°C. The identified equivalent resistivity corresponds to the minimum of this function.

The optimized resistivity value is still subject to a certain degree of uncertainty, which is estimated by considering the main contributing factors of uncertainties arising from both the experimental resistance measurements R_m and the numerical simulations R_s:

$$\rho = \rho(R_m, R_s) = \rho(R_m, \rho_{Cu}, \delta, L_v, m). \quad (46)$$

In particular, the uncertainty on R_s depends on the electrical resistivity of the copper electrodes ρ_{Cu}, on the graphene strip thickness δ, on its length L_v, and on the discretization of the numerical mesh m .The overall uncertainty was then derived from the propagation of these individual contributions:

$$u_\rho^2 = \sum_i \left(\frac{\partial \rho}{\partial x_i}\right)^2 x_i^2, \quad x_i \in (R_m, \rho_{Cu}, \delta, L_v, m). \tag{47}$$

Subsequently, a linear regression was performed to obtain an analytical relationship between resistivity and temperature, also providing the combined standard uncertainty as well as the regression-related uncertainty. As an example, in Figure 18 the trend obtained for G-paper is shown.

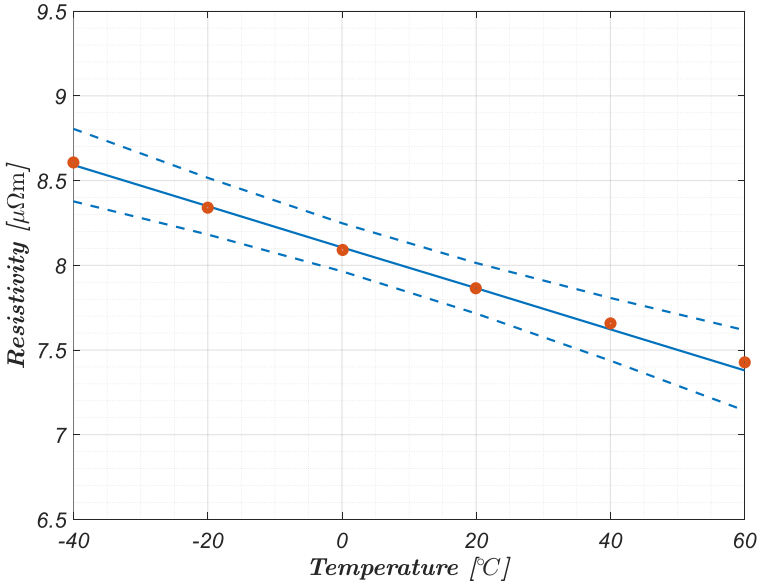

Figure 18. Linearized model of the equivalent electrical resistivity identified in the range (-40, +60) °C, for: G-paper.

The procedure was applied to all the materials listed in Table 1, which exhibit a Negative Temperature Coefficient (NTC) behavior, and whose TCR values are also reported in the Table *3*.

Table 3. Fitting parameters for the linear model of the resistivity (10), at the reference temperature of 20°C

Material	ρ_0 [m/S]	α [1/°C]
G-paper	7.8644E-06	-1.5452E-03
G-Preg (95/5)	1.5583E-05	-1.3761E-03
G-Preg (80/20)	2.0959E-05	-1.2236E-03
G-Preg (70/30)	2.3360E-05	-1.4468E-03
G-Preg (50/50)	5.3938E-05	-1.2601E-03
G-Preg (30/70)	1.7102E-04	-1.0542E-03
G-Preg (25/65-10)	9.5368E-05	-1.4009E-03

2.3 Thermal Characterization

Among the various experimental techniques developed for the evaluation of thermal properties, the laser-flash method (FM) is one of the most widely adopted. This technique, which relies on the analysis of transient temperature responses after a short thermal pulse, is particularly suited for homogeneous, isotropic, and optically opaque samples. A thin specimen is irradiated on one side by a short energy pulse, typically from a laser or a photographic flash, and the temperature rise on the opposite

surface is recorded using a contactless sensor such as a pyrometer or an infrared (IR) camera.

From the resulting temperature–time curve, once the density (ρ) and the specific heat capacity (c_p) are known, the thermal conductivity (k) can be calculated using the relation:

$$\alpha = \frac{k}{\rho c_p} \tag{48}$$

However, when applied to GNP-based materials, several limitations arise. The heterogeneous and anisotropic nature of these films is in contrast with the basic assumptions of the classical analytical models, such as those proposed by Parker and co-workers, which consider one-dimensional heat flow and instantaneous pulse absorption. Moreover, the finite duration of the pulse can lead to significant deviations in the transient temperature profile, resulting in inaccurate estimations of α. Additional complications stem from the partial transparency of GNP conglomerates: radiation penetrates the material and transfers heat internally, reaching the rear surface earlier than expected and thus leading to an overestimation of diffusivity. These effects can be mitigated by applying surface coatings (e.g., thin layers of colloidal graphite) to enhance emissivity and optical opacity, or by using correction models that account for internal radiation absorption. Nevertheless, these strategies increase the experimental complexity and introduce additional uncertainty.

Based on these considerations, a simpler approach is proposed, which still relies on the thermal transient and combines experimental testing with simulation.

2.3.1 Estimation of the Emissivity

The first step in the thermal characterization consisted in experimentally estimating the emissivity.

The set-up proposed (Sibilia, 2021) for the test consists of a power supply, used to supply the strip and trigger the thermal transient, and a multimeter, used to monitor the voltage drop, from which the resistance can be estimated given the known current. Thermal quantities are monitored by means of a thermal camera and two thermocouples: one placed directly on the strip to measure its actual temperature, and the other positioned in the environment as a reference. To minimize the influence of external conditions, the sample is placed inside a polystyrene frame, which acts as thermal insulation, and covered with a hollow cylinder painted black to exclude radiation. The thermal camera is positioned above, aligned with the opening of the cylinder.

(a)

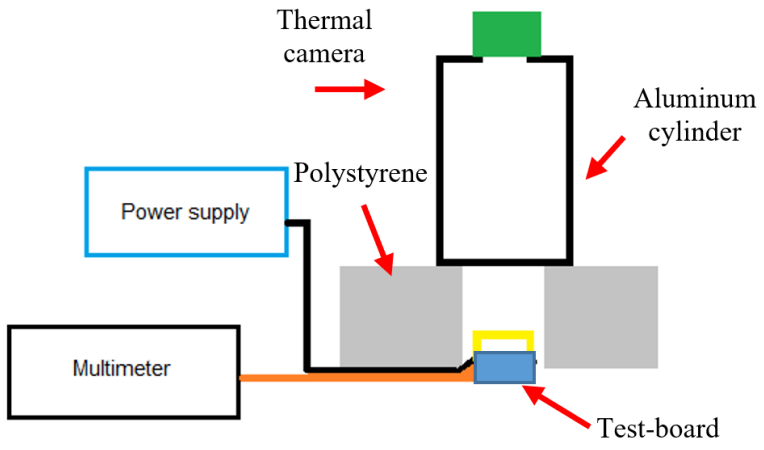

(b)

Figure 19. Schematic (a) and picture (b) of the set-up for the estimation of the emissivity of the material under test (Sibilia, 2021).

The procedure for the experiment and for estimating the emissivity is simple and effective (Sibilia, 2021). The sample is supplied with an electrical current that triggers a thermal transient and heats it until thermal steady-state conditions are reached. Once the temperature becomes stable over time, both the ambient temperature and the temperature locally measured on the material strip are taken as reference values. The ambient temperature is used as a calibration parameter for the infrared (IR) camera and is set according to the measured reference. Similarly, the emissivity of the sample surface, which is another calibration parameter, is adjusted until the temperature recorded by the IR camera matches the reference temperature. The emissivity value obtained in this way represents the final output

of the test and is subsequently used for the thermal characterization of the material.

2.3.2 Estimation of the Thermal Conductivity and Diffusivity

Experimental Set-up

The second set-up is dedicated to the estimation of thermal parameters is here described (Giovinco, 2023). The strip is placed vertically and kept stable by means of a support specifically designed with a 3D printer. The ends of the support act as electrodes which, connected to a power supply through cables, allow a constant current to be injected into the sample. The support is placed inside a black box to exclude any contribution from radiation. The thermal transient is acquired using a thermal camera, positioned at an opening on one wall of the black box. Thermocouples are also placed inside the chamber to monitor the ambient temperature.

(a)

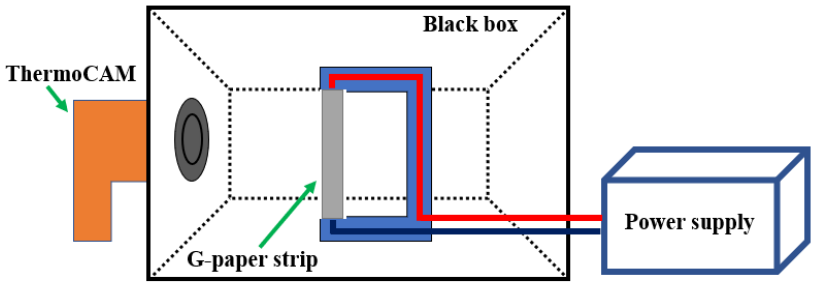

(b)

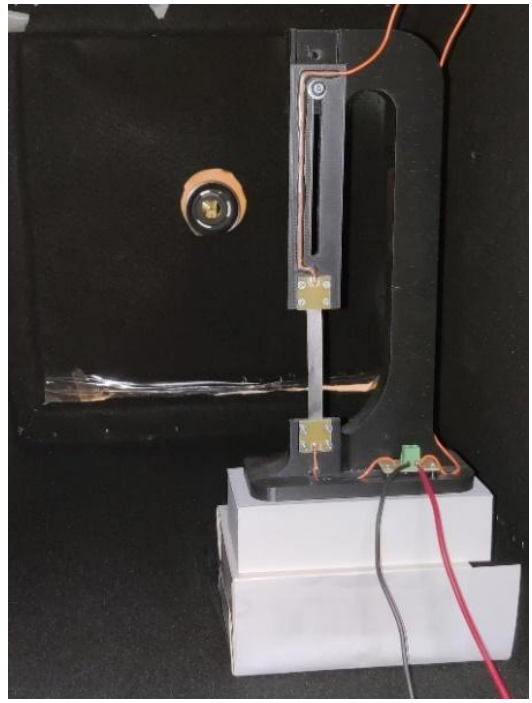

Figure 20. Schematic (a) and picture (b) of the set-up for the thermal characterization of GNP-based strips (Giovinco, 2023).

Methodology for Estimating the Thermal Conductivity and Diffusivity

The proposed methodology aims to estimate the thermal conductivity and diffusivity of graphene nanoplatelet (GNP) films by exploiting the thermal transient induced by Joule heating and monitored through infrared (IR) thermography. The approach is proposed in Giovinco *et al.* and offers a low-cost solution, since it is based on simple and easily available experimental instrumentation. It combines experimental measurements with numerical modeling and is articulated in two main steps. In the first step, the volumetric heat capacity (ρc) is evaluated; in the second step, the thermal conductivity (k) is estimated, while the thermal diffusivity (α) is subsequently derived from the following relation (48) (Bejan, 2003).

In the first phase, a small region of the GNP strip (of surface area A and thickness δ) was selected in the central part of the heated strip, where the temperature field can be reasonably assumed to be uniform. This assumption is supported by both physical and experimental considerations.

From a physical point of view, the selected region is sufficiently far from the strip edges, where boundary effects are negligible, and lies in a zone dominated by in-plane thermal diffusion, which promotes rapid homogenization of the temperature field (Yu, 2011) In thin, highly conductive materials (Balandin, 2011), heat diffusion efficiently smooths spatial temperature gradients over length scales smaller than the characteristic thermal diffusion length, leading to quasi-uniform temperature distributions in the central region of the sample (Yu, 2011). Moreover, due to the high in-plane thermal conductivity of

graphene-based materials (Balandin, 2011; Ghosh, 2008), the temperature measured by infrared thermography can be regarded as an effective, spatially averaged quantity representative of the composite medium (Yu, 2011). From an experimental standpoint, the spatial resolution of the IR camera (640 × 480 pixels, corresponding to a pixel size of approximately 0.5 × 0.5 mm²) is orders of magnitude larger than the characteristic size of individual graphene nanoplatelets (≈30 × 30 μm²). As a result, each pixel measures an effective, volume-averaged temperature that includes both the binder and the embedded nanoplatelets, justifying a continuum description of the material.

Temperature uniformity within the selected area was further validated by verifying that the maximum spatial temperature gradient remained below 0.1 °C per pixel, well above the camera thermal sensitivity (NETD ≈ 0.05 °C), thus confirming that any residual non-uniformities are below the measurement uncertainty.

In the selected region, radiative and convective heat exchanges were assumed to dominate over conduction, leading to the following energy balance equation (Tian, 2013):

$$\rho c V \frac{\partial T(\vartheta)}{\partial \vartheta} = 2A[h(\vartheta)\,(T(\vartheta) - T_\infty) + \sigma\varepsilon(T^4(\vartheta) - T_w^4)] \qquad (49)$$

where $V = A\delta$ is the volume of the region, $h(\vartheta)$ is the convective heat transfer coefficient, σ and ε are the Stefan–Boltzmann constant and the surface emissivity, respectively, T is the mean temperature of the region, $T_\infty$is the ambient air temperature, and T_w is the mean radiant temperature of the surroundings.

Experimentally, the strip was first heated by the Joule effect under a controlled current until the desired temperature was reached, then the current was switched off, and the ensuing thermal decay was recorded using the IR camera. The transient temperature evolution was used to identify the product ρc by numerically solving the differential equation above and minimizing the following squared error function:

$$E^2 = \sum_{\vartheta=0}^{\vartheta_{\max}} [T(\vartheta) - \tilde{T}(\vartheta)]^2 \tag{50}$$

where $\tilde{T}(\vartheta)$is the temperature measured by the IR camera.

Before solving the model, the emissivity ε of each GNP strip was determined experimentally by comparing the IR temperature readings with those from contact thermocouples, iteratively adjusting ε until convergence was achieved (Sibilia, 2021).

Once the volumetric heat capacity ρc was determined, the thermal conductivity k was estimated by solving the one-dimensional Fourier equation, which includes the volumetric heat generation term associated with Joule heating:

$$\begin{aligned} \rho c V_n \frac{T_n(\vartheta+1) - T_n(\vartheta)}{\Delta\vartheta} \\ = k\delta w \frac{T_{n-1}(\vartheta) - 2T_n(\vartheta) + T_{n+1}(\vartheta)}{\Delta y} \\ + 2A_n[h_n(\vartheta)(T_\infty - T_n(\vartheta)) + \varepsilon\sigma(T_w^4 - T_n^4)] \\ + \Delta R_n(\vartheta) I^2. \end{aligned} \tag{51}$$

This equation was discretized using the Finite Difference (FD) method with a 1D spatial grid along the length of the strip (Figure 21).

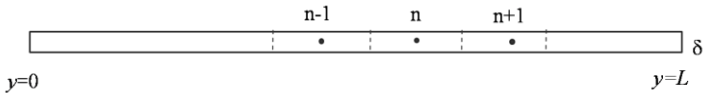

Figure 21. Domain discretization of the GNP strip in view of the evaluation of k through a Finite Difference method (Giovinco, 2023).

The IR-measured temperatures $\tilde{T}_1(\vartheta)$ and $\tilde{T}_N(\vartheta)$ were applied as boundary conditions at the strip ends, while the thermal conductivity $k$was identified by minimizing the sum of the squared deviations between the simulated and measured temperature distributions:

$$\epsilon^2 = \sum_{n=2}^{N-1} [T_n(\vartheta) - \tilde{T}_n(\vartheta)]^2 \tag{52}$$

This optimization was performed during the cooling phase until quasi-steady-state conditions were reached (about ten minutes in this study). The temperature dependence of the local electrical resistance $\Delta R_n(\vartheta)$ was introduced according to the procedure reported in Paragraph 2.2.

It is worth noting that the equivalent thermal conductivity estimated here inherently includes the effects of thermal interfacial resistances between individual nanoplatelets, since the pixel area of the IR detector is significantly larger than that of a single GNP. Moreover, by analyzing a central region of the strip, sufficiently far from the electrode contacts, the influence of

interfacial resistances at the electrode/strip interface was considered negligible.

Numerical Implementation

The differential equations described above were solved numerically using the Crank–Nicolson scheme. The IR camera frame rate (9 Hz) allowed adopting a time step of 1/900 s (i.e., 1/100 of the frame period). The temperature decay was analyzed over a time window of approximately 1/3 s to ensure that heat exchange remained primarily one-dimensional.

To identify the region of uniform temperature A, a dedicated algorithm was implemented:

1. The IR temperature distribution was de-noised using the shock filter technique (Gilboa, 2002); the filtered temperature field was denoted $\hat{T}$.

2. The temperature gradient magnitude was computed for each pixel as

$$g(i,j) = \sqrt{\left(\frac{\partial \hat{T}(i,j)}{\partial x}\right)^2 + \left(\frac{\partial \hat{T}(i,j)}{\partial y}\right)^2} \tag{53}$$

where (i,j) are the pixel coordinates.

3. The uniform region $A$was identified as the largest rectangular area where $g(i,j) \leq 0.1$, following the criterion established in (Seibold, 2020).

For each discretized sub-strip, the local mean temperature $\tilde{T}_n(\vartheta)$was evaluated and used to estimate the thermophysical properties of air, from which the local convective heat transfer

coefficient $h_n(\vartheta)$was derived following the methodology reported in (Churchill, 1975) The discretization step w in the transverse direction was chosen sufficiently small (seven pixels) to neglect boundary effects, assuming nearly adiabatic lateral conditions.

Experimental Procedure and Results

Once the product ρc was estimated, the thermal conductivity k was calculated through the solution of the Fourier equation:

$$\rho \cdot c \cdot \delta \cdot \frac{\partial T}{\partial \vartheta} = k \cdot \delta \cdot \frac{\partial^2 T}{\partial y^2} + 2 \cdot [h \cdot (T_\infty - T) + \sigma \cdot \varepsilon \cdot (T_w^4 - T^4)] + Q \tag{54}$$

where Q is the heat generation due to the Joule effect.

Under the hypotheses of uncorrelated uncertainties, the uncertainty on the value of ρc can be calculated by means of the following relation:

$$\begin{aligned} u^2(\rho c) = &\left(\frac{\partial(\rho c)}{\partial \delta}\right)^2 \cdot u^2(\delta) + \left(\frac{\partial(\rho c)}{\partial A}\right)^2 \cdot u^2(A) + \\ &+ \left(\frac{\partial(\rho c)}{\partial T_\infty}\right)^2 \cdot u^2(T_\infty) + \left(\frac{\partial(\rho c)}{\partial T_w}\right)^2 \cdot u^2(T_w) + \left(\frac{\partial(\rho c)}{\partial h}\right)^2 \cdot u^2(h) \\ &+ + \left(\frac{\partial(\rho c)}{\partial \varepsilon}\right)^2 \cdot u^2(\varepsilon) + \left(\frac{\partial(\rho c)}{\partial \tilde{T}}\right)^2 \cdot u^2(\tilde{T}) \end{aligned} \tag{55}$$

Under the same assumption, the uncertainty on k is given by:

$$u^2(k) = \left(\frac{\partial k}{\partial w}\right)^2 \cdot u^2(w) + \left(\frac{\partial k}{\partial \delta}\right)^2 \cdot u^2(\delta) + \left(\frac{\partial k}{\partial A_n}\right)^2 \cdot u^2(A_n) + \left(\frac{\partial k}{\partial \Delta y}\right)^2 \cdot u^2(\Delta y) + + \left(\frac{\partial k}{\partial T_\infty}\right)^2 \cdot u^2(T_\infty) + \left(\frac{\partial k}{\partial T_w}\right)^2 \cdot u^2(T_w) + \left(\frac{\partial k}{\partial h_n}\right)^2 \cdot u^2(h_n) + + \left(\frac{\partial k}{\partial \varepsilon}\right)^2 \cdot u^2(\varepsilon) + + \left(\frac{\partial k}{\partial \Delta R_n}\right)^2 \cdot u^2(\Delta R_n) + \left(\frac{\partial k}{\partial I}\right)^2 \cdot u^2(I) + \left(\frac{\partial k}{\partial \tilde{T}}\right)^2 \cdot u^2(\tilde{T}) + + \left(\frac{\partial k}{\partial (\rho c)}\right)^2 \cdot u^2(\rho c) + u^2(\text{mesh}) \quad (56)$$

where $u^2(\text{mesh})$ is the uncertainty associated to the spatial discretization.

In addition, the combined standard uncertainty for the thermal diffusivity can be written as:

$$u(a) = \sqrt{\left(\frac{1}{\rho c}\right)^2 \cdot u^2(k) + \left(-\frac{k}{(\rho c)^2}\right)^2 \cdot u^2(\rho c)} \quad (57)$$

As for the uncertainty of the measured temperature $\tilde{T}$, the following relation holds:

$$u^2(\tilde{T}) = u^2(\tilde{T})_{\text{noise}} + u^2(\tilde{T})_{\text{uniformity}} + u^2(\tilde{T})_{\text{IR camera}} \quad (58)$$

where $u(\tilde{T})_{\text{noise}}$ is evaluated on the basis of the mentioned de-noising procedure and it is equal to:

$$u(\tilde{T})_{\text{noise}} = \max\left(\frac{\tilde{T}_{\text{noisy}} - \tilde{T}_{\text{de-noised}}}{2\sqrt{3}}\right)_{\text{region}} \quad (59) \quad (60)$$

whereas $u(\tilde{T})_{\text{uniformity}}$ is given by:

$$u(\tilde{T})_{\text{uniformity}} = \left(\frac{\tilde{T}_{\text{de-noised,max}} - \tilde{T}_{\text{de-noised,min}}}{2\sqrt{3}}\right)_{\text{region}}$$

The results of the thermal characterization are summarized in Table 4 and Table 5.

Table 4. Measured thermal properties for pure GNP (G-paper) and for strips with a binder percentage from 5% to 30% (G-Preg).

Parameter	G-paper	G-Preg (95/5)	G-Preg (80/20)	G-Preg (70/30)
ε	0.50	0.53	0.80	0.56
u(ε)	0.01	0.01	0.01	0.01
k **(W m^{-1} K^{-1})**	453.8	295.5	268.5	162.6
$u(k)$ **(W m^{-1} K^{-1})**	67.6	51.5	56.3	41.3
$u(k)$**%**	14.9	17.4	21.0	25.4
$u(k)$**% method only**	10.3	9.9	11.9	18.4
a **(m^2/s)**	3.65E-04	2.06E-04	1.63E-04	2.40E-04

$u(a)$ (m^2/s)	6.28E-05	4.06E-05	3.72E-05	6.39E-05
$u(a)$%	17.2	19.8	22.8	26.6
$u(a)$% method only	12.3	12.5	13.9	19.6

Table 5. Measured thermal properties for strips with a binder percentage from 50% to 75% (G-Preg).

Parameter	G-Preg (50/50)	G-Preg (30/70)	G-Preg (25/65-10)
ε	0.70	0.75	0.82
u(ε)	0.01	0.01	0.01
k ($W\ m^{-1}\ K^{-1}$)	329.5	54.7	86.0
$u(k)$ ($W\ m^{-1}\ K^{-1}$)	44.9	73.9	63.0
$u(k)$%	13.6	135.2	73.2
$u(k)$% method only	7.2	100.0	46.4
a (m^2/s)	3.06E-04	6.93E-05	1.09E-04
$u(a)$ (m^2/s)	4.91E-05	9.39E-05	8.04E-05
$u(a)$%	16.1	135.6	73.8
$u(a)$% method only	10.0	100.0	46.8

CHAPTER 3
Applications of Multifunctional Nanomaterials

In recent years, the development of nanostructured materials has opened new perspectives for designing multifunctional systems capable of combining, within a single structure, different physical properties. Among the most promising nanomaterials, graphene-based materials, in particular graphene nanoplatelets, have emerged as ideal candidates for applications requiring high thermal and electrical performance, combined with lightness and mechanical robustness.

The use of an industrial-grade version of graphene, based on GNPs, represents an effective compromise between performance and production cost, thanks to the possibility of obtaining these materials through industrially scalable processes. GNPs can be incorporated into other materials matrices, resulting in materials with tunable thermal and electrical properties depending on the concentration and orientation of the nanoplatelets.

These characteristics have made GNP-based composites particularly attractive, for example, for the development of thermal interface materials (TIMs) aimed at improving heat dissipation in high-power electronic devices.

However, the solutions proposed so far still show significant limitations, such as excessive thicknesses (2–10 mm) (Shahil, 2012), incompatible with the requirements of typical TIM applications (10–100 μm), and insufficient thermal conductivity

(5–10 W/m·K) (Tian, 2013). These aspects highlight the need for further studies focused on structural optimization and on understanding the mechanisms governing thermal transport in such anisotropic systems.

At the same time, in several industrial sectors, such as aerospace (Yamazaki, 2021) energy production (Wang, 2017) and distribution (Fakorede, 2016) and transportation, the problem of ice accumulation on critical surfaces has become increasingly important. Ice formation can compromise both the efficiency and safety of structures and systems, making the development of reliable, lightweight, and energy-efficient ice detection and removal systems essential. Numerous ice-sensing techniques have been investigated in recent years, based on pneumatic, piezoelectric, magnetostrictive, acoustic, dielectric, optical, or microwave principles. However, none of these approaches is completely free of drawbacks: contact sensors, while easy to integrate, can provide partial or distorted measurements, whereas indirect methods typically require complex and expensive equipment. Furthermore, the performance of these sensors is strongly affected by environmental conditions such as temperature, humidity, and the type and thickness of ice, leading to reduced measurement reliability.

Alongside ice detection, the development of efficient de-icing systems represents another major technological challenge. Conventional solutions (mechanical, chemical, or thermal) present several disadvantages in terms of efficiency and maintainability. Among the most promising alternatives, electrothermal de-icing, based on the Joule heating effect in conductive materials, combines higher energy efficiency with easier controllability (Botura, 2025; Karim, 2018). Nevertheless,

the use of conventional metals (e.g., copper or aluminum) as heating elements introduces limitations related to weight and current density management. To overcome these issues, research has recently turned toward lightweight conductive composites, particularly those made of graphene- or graphite-based materials, which provide good electrical and thermal performance while maintaining reduced cost and complexity.

In parallel, the increasing electronic integration in aerospace and advanced transportation systems has raised new challenges concerning electromagnetic interference (EMI) shielding. The miniaturization and densification of on-board electronic components expose systems to higher electromagnetic noise levels, which can compromise their reliability and safety. Conventional metallic coatings, though effective in EMI attenuation, are typically heavy, prone to corrosion, and difficult to integrate with modern lightweight structures. For this reason, there is a growing demand for innovative, lightweight, and multifunctional EMI-shielding materials that can ensure both structural compatibility and thermal or sensing functionalities. GNP-based composites, thanks to their high electrical conductivity, low density, and processability, offer a promising route to achieve flexible coatings capable not only of electromagnetic protection but also of distributed temperature monitoring, enabling smart thermal management in critical electronic systems.

In this context, GNP-based composites stand out as highly interesting materials for the realization of multifunctional devices (Huang, 2019). Their intrinsic properties potentially allow the combination of heating, sensing, shielding, and thermal management functions within a single material, paving the way

for innovative solutions capable of overcoming the limitations of conventional technologies.

In this Chapter, the studies made about the use of industrial GNP-based material as heaters, ice-sensor, electromagnetic shield and temperature sensor are presented.

3.1 Study on the Use as a Heater

To assess the potential use of the graphene-based strip as an actuator in a de-icing system, the tests performed to estimate the thermal properties of the graphene strips were also employed to analyze the thermal transient induced by Joule heating. Crucial aspects to be considered involve both the steady-state temperature reached and the time required to achieve a significant temperature rise.

3.1.1 Experimental Analysis

The proposed experimental setup is described in the previous chapter. The main result considered is the thermal transient acquired through the thermal camera, with an example of the resulting thermal image shown in Figure 22

By using the dedicated software, it is possible to extract the temperature data corresponding to each pixel of the thermal image. This enables the acquisition of detailed and localized information on the temperature distribution across the entire graphene strip. The entire transient was recorded as a video, with an acquisition frequency of 9 Hz, corresponding to a time interval of approximately 0.111 s between consecutive frames. This

information enables the temperature evolution at a specific point within the frame to be reconstructed as a function of the test time.

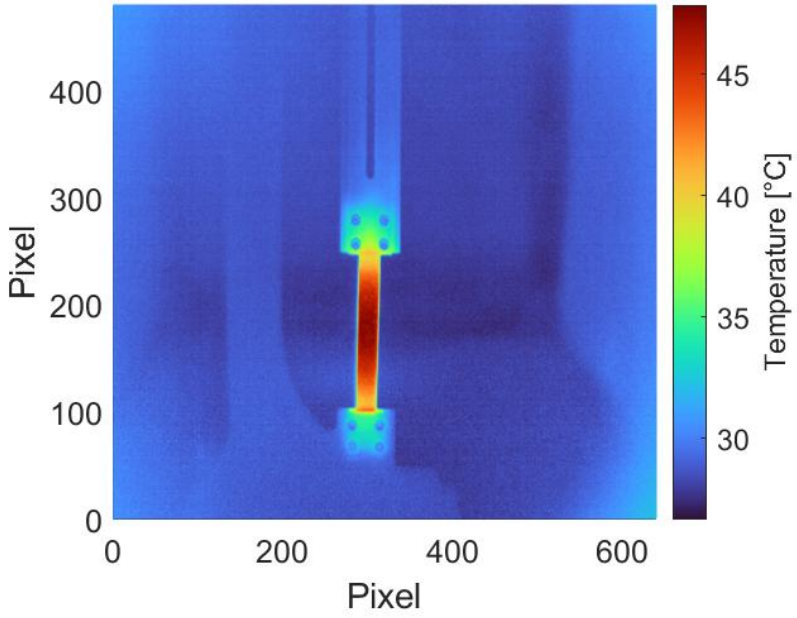

Figure 22. Thermal map of the graphene strip while it is supplied and heated because of Joule effect.

The analysis shows that the maximum temperature is reached at the center of the strip, while lower temperatures are observed at the ends due to edge effects related to the presence of the electrodes. The latter, made of conventional materials, exhibit higher heating time constants compared to the GNP-based material, resulting in a temperature gradient between the central and peripheral regions of the strip.

On this basis, the central point of the strip was selected to investigate both the heating time response and the absolute

temperature achieved by the material. The corresponding thermal transient is shown in Figure 23.

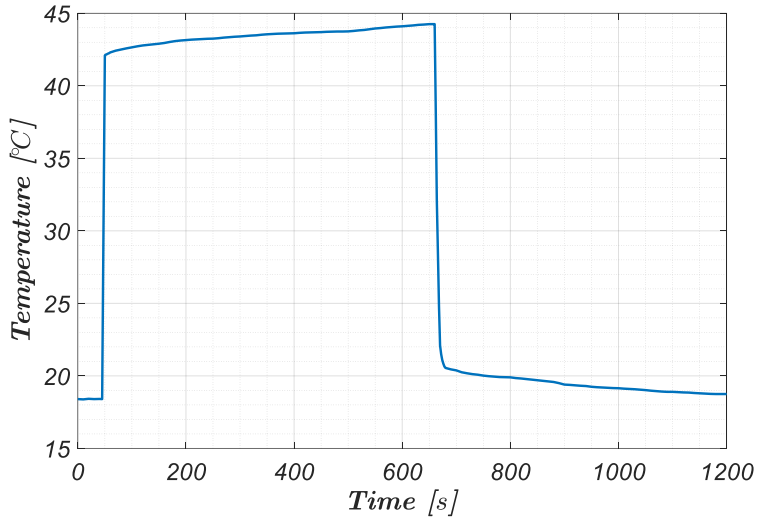

Figure 23. Temperature trend on the surface of the strip at its central point during the thermal transient.

From the thermal transient at the point of interest, the time constant associated with the heating phase was calculated, defined as the time required to reach 63.2% of the final temperature value in response to the applied current input.

The calculation was performed for the 95/5 and 50/50 formulations; for each sample, the time constant was determined as the average of five independent experiments.

For the 50/50 formulation, the analysis was also carried out on two distinct samples to verify reproducibility.

For comparison, the same analysis was conducted on a copper strip with dimensions and temperature variations comparable to those of the tested materials.

The average values and the standard deviations obtained are summarized in Table 6.

Table 6. Time constants of the thermal transients for all tests (highlighted in green) and corresponding mean values and standard deviations for each tested strip.

SAMPLE.	#TEST	τ [s]	AVERAGE VALUE [s]	σ [s]
95-5 Strip1	1	2.224	2.868	1.142
	2	4.112		
	3	4.112		
	4	2.001		
	5	1.889		
50-50 Strip1	1	1.778	3.134	0.97
	2	2.667		
	3	4.112		
	4	3.112		
	5	4.001		
50-50 Strip2	1	2.334	2.889	0.716
	2	4.001		
	3	2.223		
	4	2.778		

	5	3.112		
Cu Strip1	1	25.08	21.514	4.111
	2	21		
	3	19.49		
	4	16		
	5	26		

The results obtained confirm that the graphene-based strip can serve as an excellent heating element, offering high efficiency and fast thermal response.

In particular, the low time constants observed highlight a rapid transition to steady-state temperature, demonstrating the material's ability to quickly achieve stable operating conditions. These features make the graphene strip highly promising for controlled heating applications, such as de-icing systems or other solutions requiring fast thermal reactivity and uniform heat distribution.

3.1.2 Numerical Model

To validate the experimental results and to study the heater behavior under other operating conditions, as well as for analyse its response when other type of materials is integrated, the numerical model described in the previous chapter was used.

The heating behavior of the graphene strip was than simulated using the coupled electro-thermal model. This approach allowed the simultaneous solution of the electrical and thermal fields, thus capturing the interaction between Joule heating and heat

dissipation mechanisms. The simulations were carried out under steady-state conditions to reproduce the long-term thermal response of the system and validate the model against the experimental measurements.

Figure 24(a) shows the temperature profiles along the graphene strip axis at successive time steps, starting from the baseline condition (blue curve) corresponding to the instant when the current was first applied. The profiles were collected every 10 seconds. After one hour, the system reached steady state; this experimental profile is compared in Figure 24(b) with the result of the numerical simulation. In the model, the resistivity of the G-paper was described using equation (44) with the parameters specified in Table *3*. The comparison reveals an overall excellent agreement, with only minor deviations at the strip ends, most likely caused by local thermo-mechanical interactions with the copper electrodes that were not included in the numerical model.

(a)

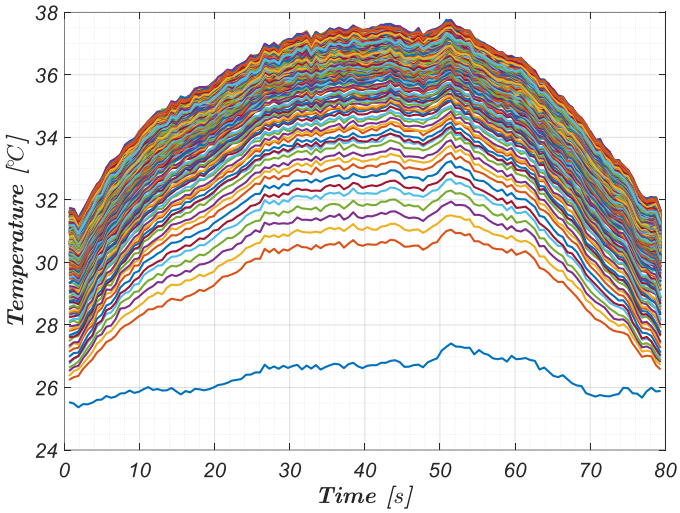

(b)

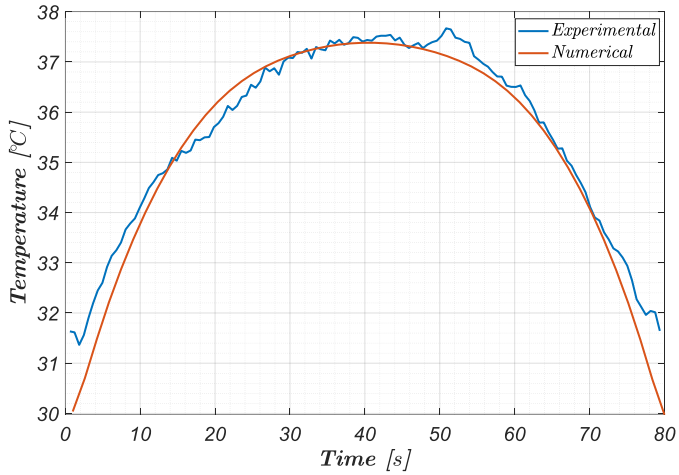

Figure 24. Spatial distribution of the temperature along the axis of the graphene strip (G-paper), for a current of 0.7 A: (a) experimental curves taken during the transient (each 10 s); (b) steady state condition reached after 3600 s (1 hour): measured vs simulated.

3.2 Study on the Use as an Ice Sensor

3.2.1 Operating Principle

The operating principle of the sensor is based on the variation of the electrical capacitance of a planar capacitor as a function of the dielectric properties of the material located above its electrodes. Unlike a traditional parallel-plate capacitor, where the electrodes are placed on opposite planes and the electric field lines are uniform and perpendicular to the surfaces, in a planar capacitor the two conductive electrodes are positioned on the same plane, side by side.

In this configuration, the electric field lines develop partly between the facing inner surfaces of the two electrodes, but a significant portion of them extends into the space above the electrodes and then closes back onto the opposite conductor. These lines that extend outside the plane of the capacitor are known as fringe field lines. These fields play a crucial role in the sensor's operating principle, as they directly pass through the material located above the sensitive surface.

The resulting capacitance of the system therefore depends not only on the geometry of the electrodes but also on the dielectric permittivity of the medium through which the field lines propagate. When the material above the electrodes changes (for instance, from air to ice or water) the field distribution and thus the measured capacitance also vary. The frequency-dependent behavior of the dielectric permittivity for air, ice, and water is shown in Figure 25.

Specifically, the permittivity of ice is significantly higher than that of air at low frequencies but decreases with increasing frequency, reducing to values close to that of air beyond approximately 10^5 Hz. Water, on the other hand, maintains a much higher permittivity up to higher frequencies, around 10^7 Hz.

By exploiting this difference in dielectric behavior, the planar sensor can distinguish between different states of the material above it, allowing the detection of ice formation or the presence of water through capacitance measurements at an appropriately chosen frequency.

The fringe field lines therefore represent the key element in the sensor's operation, as they enable the device to interact with the external environment and to convert the physical changes of the overlying layer into a measurable electrical signal.

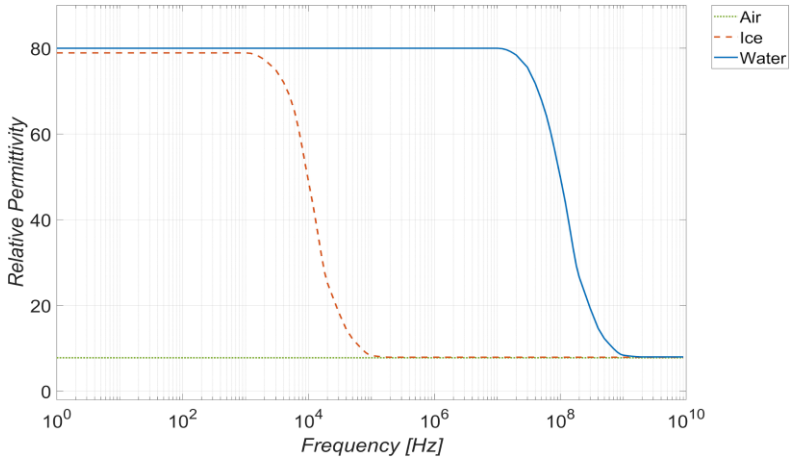

Figure 25. Trend of the permittivity of air, water, and ice as a function of frequency (Sibilia, 2023).

3.2.2 Analyzed Architectures

In this study, two sensor prototypes based on the same operating principle but designed with different topologies were tested.

First Prototype

The first prototype is a planar capacitive sensor in which the sensing electrode is a graphene-based strip acting as the central plate. The strip is placed on a multilayer PCB and contacted at its ends by metallic electrodes, which provide mechanical clamping and electrical connection. The PCB integrates a guard ring surrounding the sensing area and an array of through vias on both sides of the central electrode, electrically connected to form the second plate of the capacitor. In Figure 26 and Figure 27 the cross section and a picture of the realized sensor are respectively shown.

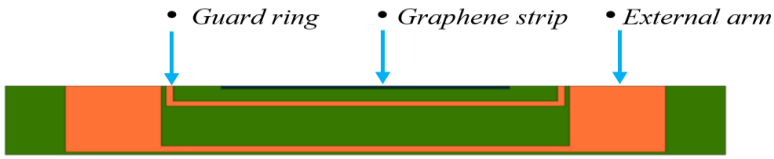

Figure 26. Cross-section of the designed ice sensor (planar capacitor) (Sibilia, 2023).

In this configuration, the electric field lines close primarily between the graphene strip and the via array, with a contribution of fringing fields extending above the surface; consequently, the resulting capacitance is modulated by the permittivity of the overlying medium (air, ice, water). The guard ring, driven at the measurement input potential, reduces parasitic capacitances and

confines the field to the active region, improving measurement stability and repeatability. Using graphene as the central electrode provides minimal thickness and low-profile sensing surface well suited for PCB integration.

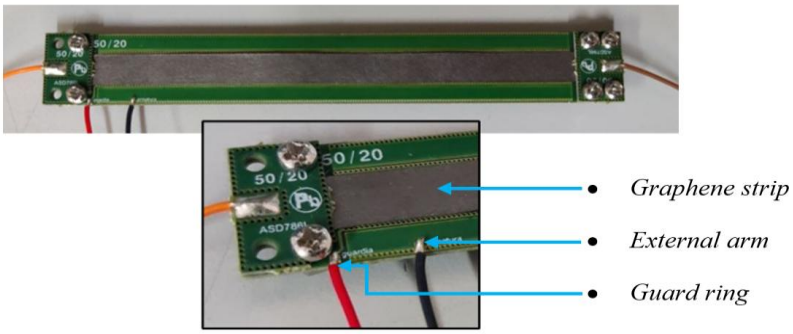

Figure 27. Realization of the ice sensor with a PCB structure. The central gray strip is the graphene element. The amperometric cables (orange and brown cables) are separated from the voltmetric ones (black and red) to enable the 4-probe measurement technique (Sibilia, 2023).

The sensor behavior can be theoretically described using the circuit model shown in Figure 28. In this model, the GNP arm is represented by a parallel RC branch, which accounts for the high sensitivity of graphene's complex permittivity to environmental conditions. The resistance R_{GNP} also includes the contact contribution.

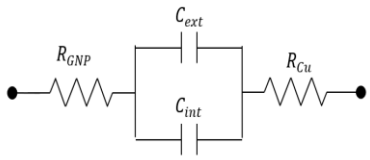

Figure 28. Equivalent electrical circuit for the proposed ice sensor, prototype 1.

The arms formed by vias, on the other hand, are modeled solely by their equivalent resistance R_{Cu}, which likewise includes the contact term. The core of the sensor is described by two parallel capacitances: C_{int}, associated with the internal region of the PCB (FR4 dielectric), and Cext, related to the displacement field lines extending outside the capacitor.

The element most affected by the presence of air or ice is C_{ext}; however, temperature variations can also influence R_{GNP}, since the resistivity of the strip can be influenced by the environmental temperature..

Second Prototype

The second prototype implements a planar capacitor consisting of two identical graphene strips placed on an FR4 substrate, functioning as coplanar electrodes in the same plane. Several strips were placed on the same substrate at varying distances from each other, in order to create distinct sensors and analyze the influence of the gap on their sensitivity. The assembly is covered with a Kapton film applied above the strips to protect the graphene electrodes from environmental degradation (e.g., humidity/condensation, dust and other contaminants, abrasion

and scratching during handling). The device operates according to the same physical principle previously described for the capacitive sensor; it differs in the electrode topology (dual-strip coplanar configuration) and in the presence of the protective Kapton overlayer.

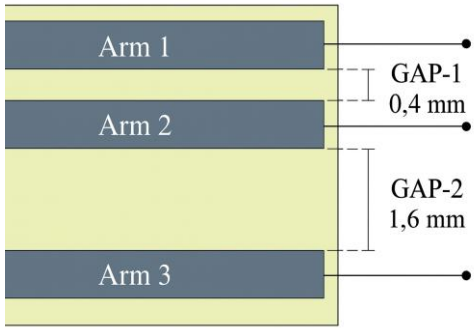

Figure 29. Top view of the conceptual schematic of the planar capacitor (Tari, 2025).

In this case, since the strips are mechanically protected by the Kapton layer, the direct influence of the environment on their electrical properties can be neglected. Therefore, in the equivalent circuit model, only the sensor capacitance is considered.

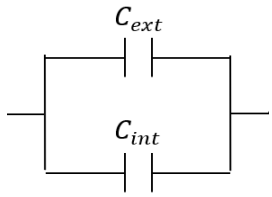

Figure 30. Equivalent electrical circuit for the proposed ice sensor, prototype 2

$$C_{eq} = C_{ext} + C_{int} \tag{61}$$

3.2.3 Numerical Model

To study the sensor behavior under varying environmental and operating conditions, as well as for use during the design phase aimed at optimizing the sensor geometry, a numerical model was implemented for both sensors.

Since both sensor prototypes have a structure in which the boundary conditions and the properties of the materials are the same along the entire length, it is sufficient to define a two-dimensional model representing the cross section of the sensor. The result obtained per unit length can then be analytically multiplied by the total length of the sensor to determine its effective capacitance.

The classic electrostatic problem is solved to derive the distribution of the electrical field, E, and the electric displacement field D, according to :

$$\nabla \cdot \boldsymbol{D} = \rho_v, \quad \boldsymbol{D} = \varepsilon_0 \varepsilon_r \boldsymbol{E}$$
$$\boldsymbol{E} = -\nabla V \tag{62}$$

After solving the electrostatic problem, the bulk capacitance is obtained by calculating the electrical energy U stored within the entire simulation domain. In this model, three conductors are considered: the two sensor arms and a reference conductor, represented by an external box placed sufficiently far from the arms, whose electrical potential is set to zero. Three partial

capacitances are associated with this configuration: the capacitance between the two arms (C_{12}) and the capacitances between each arm and the reference conductor (C_{10} and C_{20}).

Denoting the electrical potentials of the two arms with respect to the reference conductor as V_1 and V_2, the total energy stored in the domain can be expressed as follows:

$$U = \frac{1}{2}C_{11}V_1^2 + C_{12}V_1V_2 + \frac{1}{2}C_{22}V_2^2. \quad (63)$$

The partial capacitance values in Equation XX can be calculated by evaluating the energy associated with the following potential distributions:

$$V_1 = 1V, V_2 = 0V$$
$$V_1 = 0V, V_2 = 1V \quad (64)$$
$$V_1 = 1V, V_2 = -1V$$

Finally, in order to obtain the capacitance value of the 3D structure, the result can be multiplied by the length of the sensor.

Implementation With Electrostatics Interface

The Electrostatics interface is used to describe static electric fields, that is, situations in which no current flows and the field quantities do not vary with time.

Through this module, it is possible to calculate the electric field distribution within a dielectric, the capacitance between conductors, the surface charge density, and the electrostatic energy or forces.

The application case analyzed in this thesis concerned a planar capacitor designed to operate as an ice sensor for de-icing applications. The interface was used with the aim of developing a numerical model capable of validating the operating principle of the device through the simulation of the electric field and its capacitive behavior.

In the analyzed case study, the simulation was configured by applying electric potentials to the capacitor electrodes. Since the model is based on the partial capacitance theory, it was necessary to define a reference conductor placed at a sufficiently large distance from the system to represent the zero-potential condition. This conductor was implemented through an external box enclosing the main geometry, positioned far enough to avoid significantly influencing the field distribution in the region surrounding the object of interest. The model was developed in two dimensions, as the structure is uniform along the longitudinal direction. In Figure 31 the full 2D simulation domain is shown.

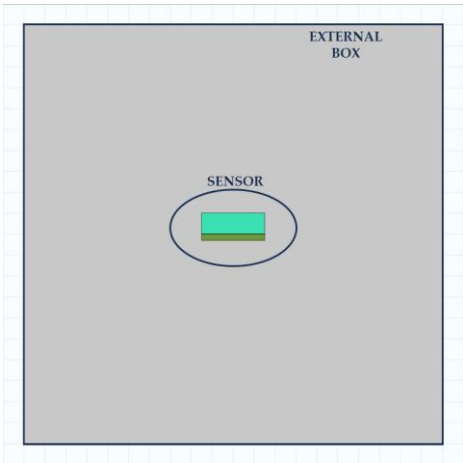

Figure 31. Full 2D simulation domain: central sensor and external box.

To obtain the information required for the evaluation of the system's equivalent capacitance, three separate simulations were carried out, varying the potentials applied to the conductors. From these simulations, the capacitance can be determined either from the induced charges on the electrodes or by calculating the total electrostatic energy of the system. In this work, the energy-based approach was adopted, as the distribution of the fringing electric field plays a key role in understanding the sensor's behavior and validating its operating principle. Once the energy associated with each simulated configuration was obtained, the analytical determination of the capacitances was performed based on the numerical results. By using this simplified representation of the structure and a hybrid approach that combines numerical simulation and analytical calculation, it is possible to achieve reliable results with an extremely low computational cost.

3.2.4 Experimental Analysis

This paragraph illustrates the methodology and the measurement procedures adopted for the experimental characterization of the ice sensor.

Prototype 1: Set-up and Characterization

The capacitance of the sensor was evaluated by measuring its electrical impedance through the experimental setup schematically shown in Figure 32a. In this configuration, the

sensor was connected to a GW-INSTEK LCR-8101G impedance analyzer (GW Instek, Taipei, Taiwan), while a personal computer was used to control the instrument via an RS-232C interface (Sanwa Supply, Okayama, Japan).

To investigate the sensor behavior as a function of frequency, Impedance Spectroscopy was employed. The impedance was measured between the external arm of the planar capacitor (Figure 27) and the graphene strip, which was set at the same potential as the guard ring. This configuration provided the highest sensitivity, as it corresponded to the smallest gap between the arms (0.1 mm). Consistent with the sensor model shown in Figure 28, a parallel R–C model was selected in the impedance analyzer to directly determine the capacitance value.

Before performing the measurements, an *open* and *short* calibration is carried out to remove all parasitic effects caused by the cables and the surrounding environment, ensuring a more accurate sensor measurement.

The measurements were carried out in the frequency range between 20 Hz and 1 MHz, acquiring three data points per decade with logarithmic spacing (e.g., 1–2–5–10, etc.). As reported in the setup diagram, the connection between the impedance analyzer and the sensor was realized using a four-probe configuration, in accordance with the design features of the PCB-based sensor (Figure 27).

When required, the sensor was placed inside a climatic chamber (ACS DY110, Angelantoni, Massa Martana, Italy) to accurately control temperature and humidity during the measurements, thus reproducing realistic operating conditions.

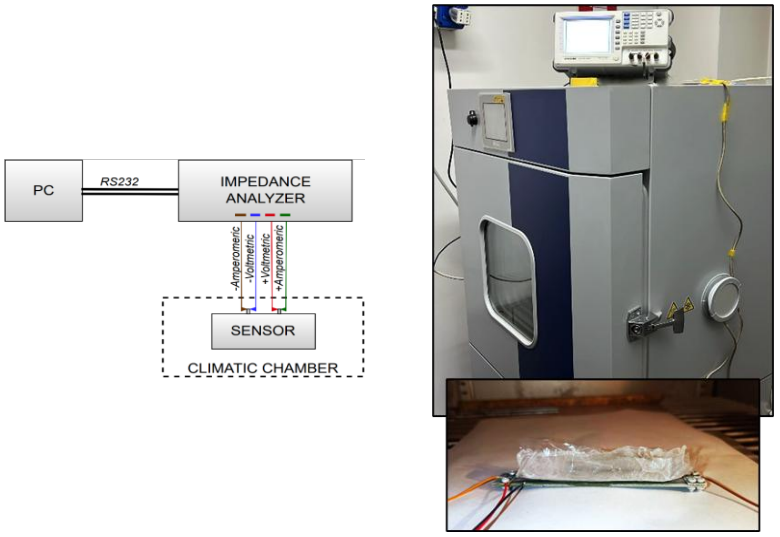

(**a**) (**b**)

Figure 32. The measurement set-up, where the electrical impedance of the sensor (placed inside a climatic chamber) is measured by an impedance analyzer, supervised by a PC via an RS232C interface: (a) schematic; (b) picture of the whole setup (top), with the detail of the sensor covered by ice (bottom) (Sibilia, 2023).

The ice sensor is tested under controlled environmental conditions, where temperature and relative humidity are regulated during the experiments through a climatic chamber. Controlling these parameters ensures repeatable and reliable measurements, allowing a consistent evaluation of the sensor's performance. This is particularly important given the sensor's intended application at high altitude, where variations in temperature and humidity can strongly influence its behavior.

The sensor was initially characterized by varying only the environmental conditions. The temperatures examined were −40,

−20, 0, and 20 °C, while the relative humidity levels were set to 0%, 10%, 25%, and 50%.

Each test was repeated 30 times in order to obtain a statistically reliable dataset and to define the baseline behavior of the sensor, that is, in the absence of any ice formation on its surface. Subsequently, tests were carried out with different types of ice, which shared the same composition but differed in their width and thickness. The decision to test different ice widths was made to investigate various configurations in which the sensor is covered by ice in different ways, whereas varying the ice thickness aimed to identify a thickness that can be effectively detected by the sensor.

Table 7 reports the dimensions of the three ice samples tested, which are identified with the labels Type A, Type B, and Type C.

Table 7. Dimensions of the ice samples used.

Ice Sample	Thickness (mm)	Width (mm)
Type A	3	12
Type B	12	28
Type C	15	10

The sensor's possible operating ranges, when used as an ice detection device, were assessed considering three distinct coverage factors ($K \cdot \sigma$). The coverage factor K defines the confidence level, that is, the likelihood that a measurement result falls within a given uncertainty interval. Under the assumption of normally distributed random errors, the probability that the actual value of the measurand lies within this interval

corresponds to approximately 68.4% for K = 1, 95.4% for K = 2, and 99.7% for K = 3.

The Figure 33 shows the variation of the sensor capacitance as a function of frequency under baseline operating conditions, that is, in the absence of ice. The plot reports the curves obtained at different ambient temperatures, with a relative humidity of 0% (except for the condition at 20 °C, where humidity was set to 10%, which is the minimum value achievable by the climatic chamber at positive temperatures).

For the temperature of −20 °C, three curves acquired under identical conditions but on different days are also shown, in order to assess the repeatability of the sensor's behavior. The figure, instead, shows the basic behavior of the sensor at the same ambient temperature of 20 °C, but with different levels of relative humidity. In this case as well, three curves obtained under the same conditions are reported.

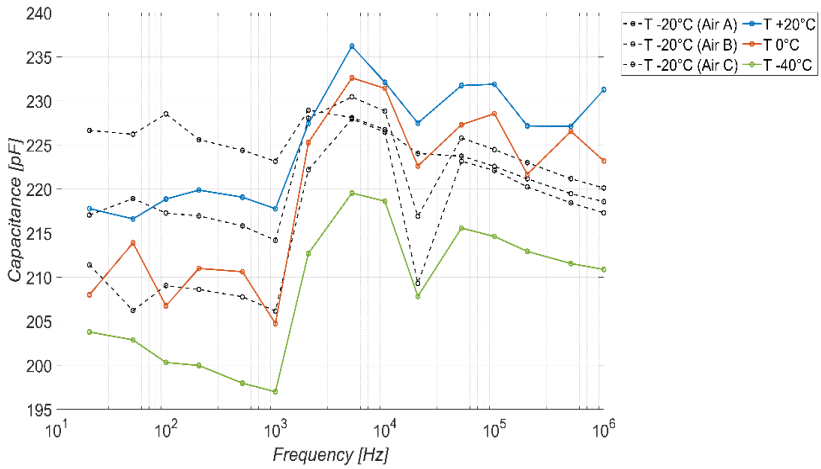

Figure 33. Response of the ice sensor as a function of frequency for different ambient temperatures (Sibilia, 2023).

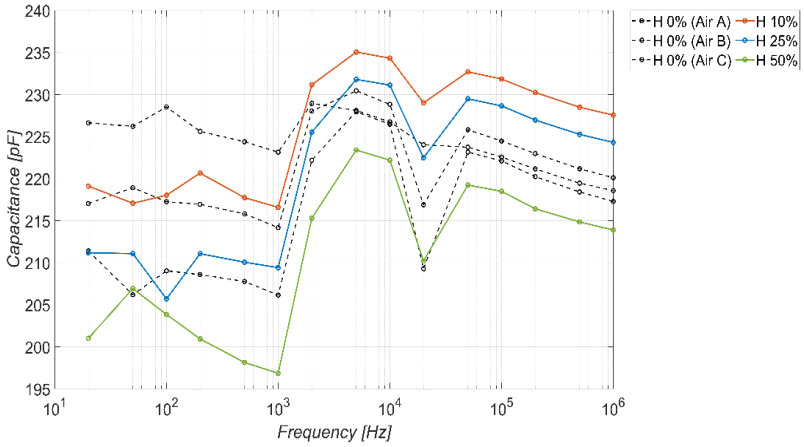

Figure 34. Response of the ice sensor as a function of frequency for different ambient humidity percentage (Sibilia, 2023).

Once the variability of the sensor due to changes in environmental conditions had been assessed, the sensor response was subsequently tested by introducing ice into the system.

Figure 9 shows how the sensor capacitance varies with frequency, for the case of a coverage factor $K = 1$, both with and without the presence of ice, for the three ice samples defined in Table 7 (labeled "A", "B", and "C"). Figures 10 and 11 report the results obtained using coverage factors of $K = 2$ and $K = 3$, respectively, to highlight how different confidence levels affect the identified operating ranges of the sensor.

To allow a direct comparison, the same labels were used for the corresponding air measurements performed on the same test days. All experiments were carried out in the climatic chamber at a fixed temperature of −20 °C. In the plots, solid lines represent the measurements with ice, while dashed lines refer to those in air. For each condition, 30 repeated tests were performed: lines

with markers indicate the mean capacitance values, and those without markers show the corresponding standard deviation.

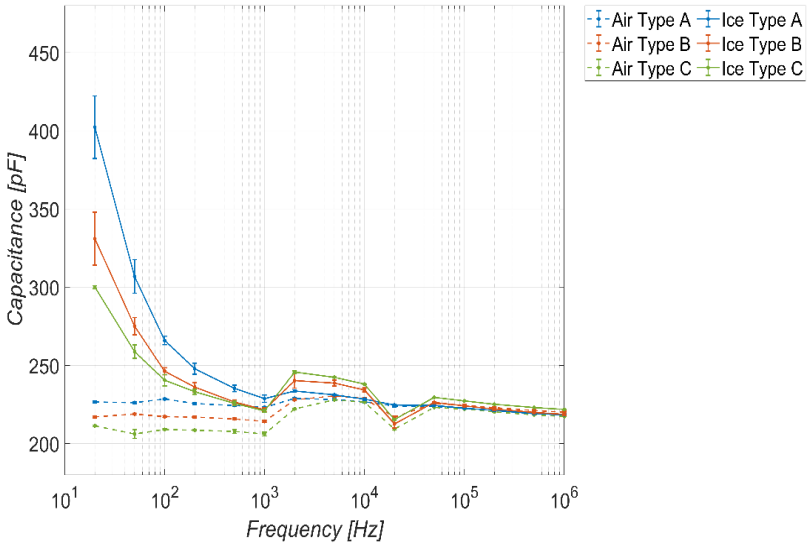

Figure 35. Measured capacitance of the sensor versus frequency, in the absence and presence of different types of ice. Temperature −20 °C, coverage factor K = 1 (Sibilia, 2023).

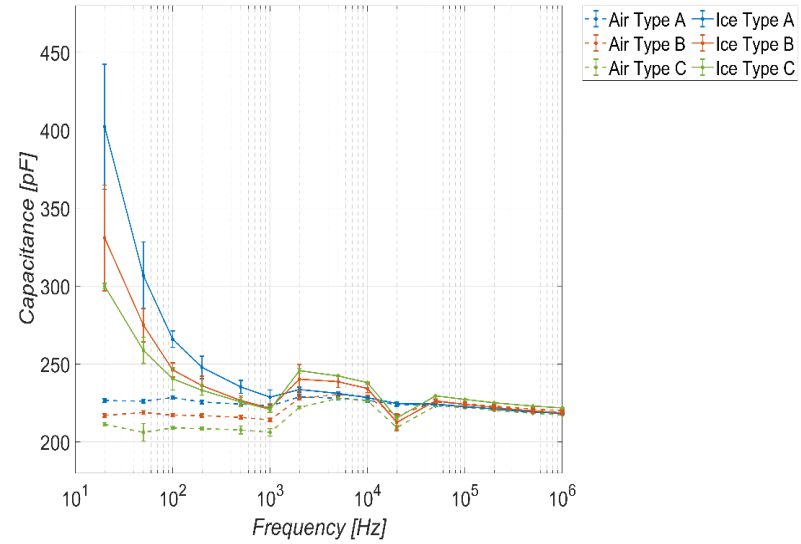

Figure 36. Measured capacitance of the sensor versus frequency, in the absence and presence of different types of ice. Temperature −20 °C, coverage factor K = 2 (Sibilia, 2023).

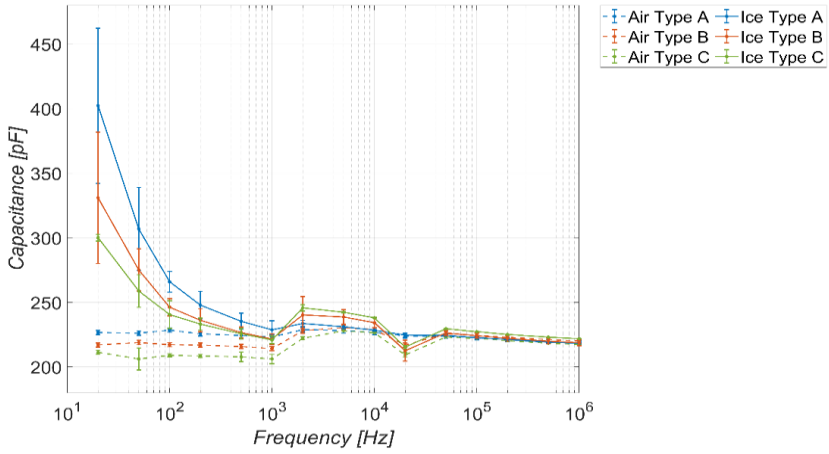

Figure 37. Measured capacitance of the sensor versus frequency, in the absence and presence of different types of ice. Temperature −20 °C, coverage factor K = 3 (Sibilia, 2023).

As a final step, Figure 38–Figure 40 illustrate, for each coverage factor K, the operating range in which the sensor functions as an ice detector. These ranges were obtained from the average capacitance trends and their maximum deviations ($\pm K \cdot \sigma$) shown in Figure 35-Figure 37. The intervals indicate the expected capacitance values with confidence levels of approximately 68.4%, 95.4%, and 99.7% for K = 1, 2, and 3, respectively. The frequency range where the curves with and without ice do not overlap identifies the region in which the sensor can reliably detect ice.

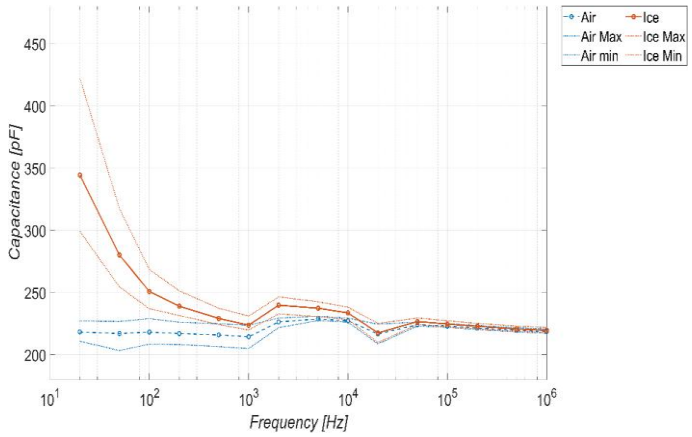

Figure 38. Sensor response in the presence and absence of ice with a coverage factor K=1, corresponding to a confidence level of 68.4% (Sibilia, 2023).

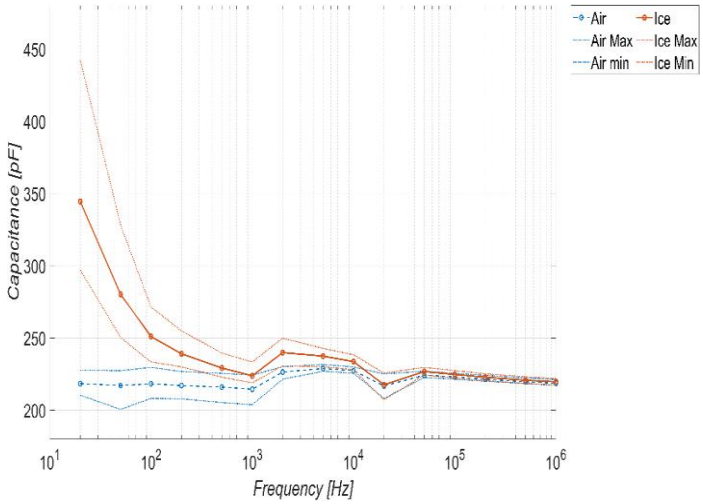

Figure 39. Sensor response in the presence and absence of ice with a coverage factor K = 2, corresponding to a confidence level of 95.4% (Sibilia, 2023).

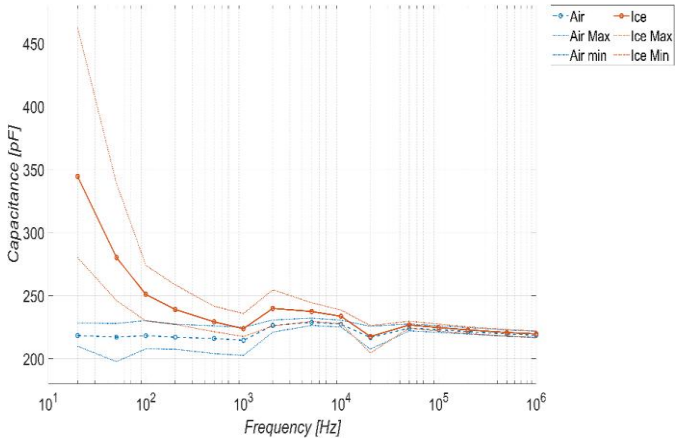

Figure 40. Sensor response in the presence and absence of ice with a coverage factor K = 3, corresponding to a confidence level of 99.7% (Sibilia, 2023).

Based on the experimental results and their interpretation with respect to the considered confidence levels, Table 8 summarizes the conditions under which the prototype is (value 1) or is not (value 0) able to operate as an ice sensor. This behavior is strongly affected by the selected confidence level. Specifically, for the most stringent confidence level, the device is capable of functioning as a sensor only at frequencies of 20 and 50 Hz.

Table 8. Summary of operating conditions of the sensor as an ice detector (value 1) at various K.

Frequency	K		
	1	**2**	**3**
20 Hz	1	1	1
50 Hz	1	1	1
100 Hz	1	1	0
200 Hz	1	1	0
500 Hz	0	0	0
1 kHz	0	0	0
2 kHz	1	1	0
5 kHz	0	0	0
10 kHz	0	0	0
20 kHz	0	0	0

50 kHz	0	0	0
100 kHz	0	0	0
200 kHz	0	0	0
500 kHz	0	0	0
1 MHz	0	0	0

Prototype 2: Set-up and characterization

As for the previous prototype, the sensor behavior was analyzed by measuring its impedance. The measurements were carried out using a GW Instek LCR-8110G impedance analyzer connected to a computer via a GPIB-488 interface, which enabled automated data acquisition and management. To minimize parasitic effects caused by the experimental setup and environmental conditions, an open and short calibration procedure was performed prior to the measurements. The characterization was conducted using a four-point measurement configuration, and to assess the stability and repeatability of the measurement system, 30 acquisitions were performed for each test condition. The investigated frequency range extended from 20 Hz to 100 kHz, with a logarithmic step, ensuring adequate resolution across the entire analyzed spectrum.

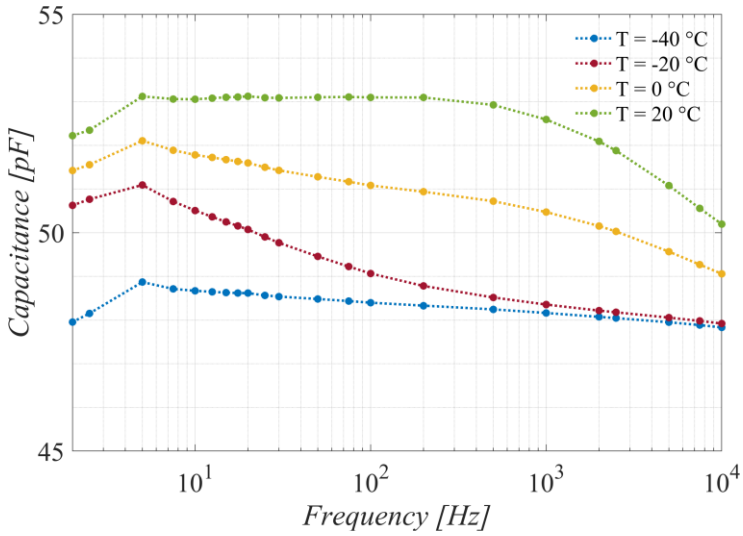

Figure 41. Capacitance vs frequency for different ambient temperature for Gap-1 = 0.4 mm (Sibilia, 2023).

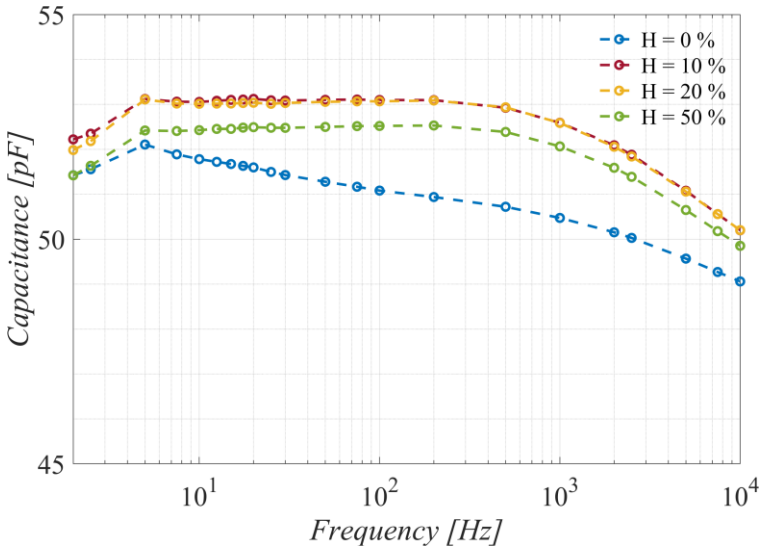

Figure 42. Capacitance vs frequency for different ambient humidity percentage for Gap-1 = 0.4 mm (Sibilia, 2023).

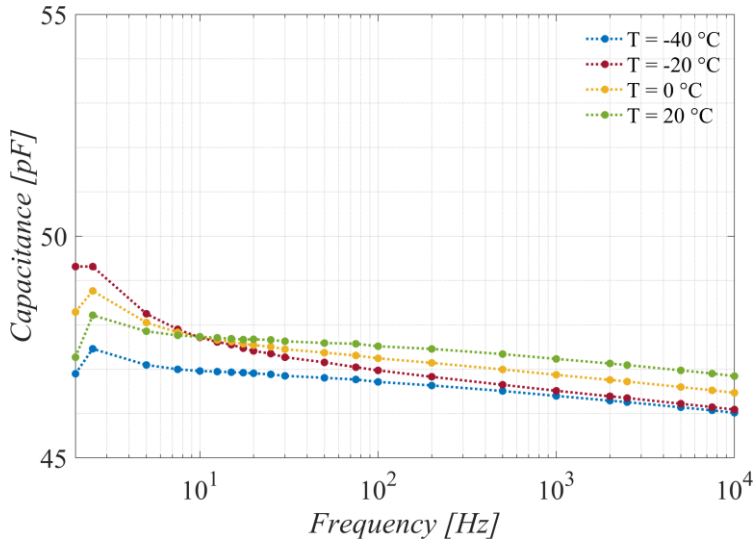

Figure 43. Capacitance vs frequency for different ambient temperature for Gap-2 = 1.6 mm (Sibilia, 2023).

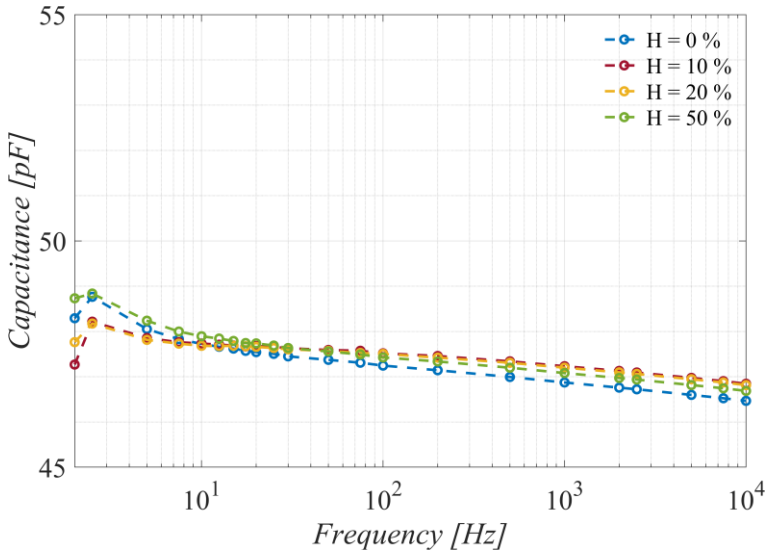

Figure 44. Capacitance vs frequency for different ambient humidity percentage for Gap-2 = 1.6 mm (Sibilia, 2023).

A preliminary study was conducted to evaluate how fringing capacitance varies as a function of ice formation on the sensor surface. This investigation aims to provide an approximate estimation of the capacitive variations induced by environmental factors and to define the corresponding design requirements for the signal conditioning circuitry.

The estimation of fringing capacitance was carried out using the Palmer formulation (Palmer, 1937), which relates the capacitance to both the geometrical configuration of the electrodes and the dielectric properties of the surrounding medium. Since the sensor geometry remains constant, variations in capacitance are primarily linked to changes in the dielectric characteristics of ice. These characteristics depend on several parameters, including temperature, density, crystal structure, level of impurities, and the frequency of the applied signal. Moreover, due to Debye relaxation effects, the permittivity of ice tends to decrease with frequency, showing higher values at low frequencies (below approximately 10 kHz).

Because of the high variability of these physical parameters, the development of an exact analytical model would not be meaningful for design purposes. Instead, a conservative assumption has been adopted, supported by literature data and preliminary multiphysics simulations: an ice layer can be considered to increase the sensor capacitance by roughly 5 pF per millimeter of thickness. This assumption is consistent with the range of values reported in recent experimental works on ice detection (Dong, 2025; Xie, 2024).

Theoretical considerations discussed in the previous section were further validated through numerical simulations performed in COMSOL Multiphysics. The simulations were carried out by

modelling the sensor both in the presence of air and with a 1 mm ice layer deposited on its surface. Figure 45 reports the simulation results for the configuration corresponding to GAP-1, where the influence of the fringing field can be clearly observed from the distribution of the electric field lines and the associated colour map.

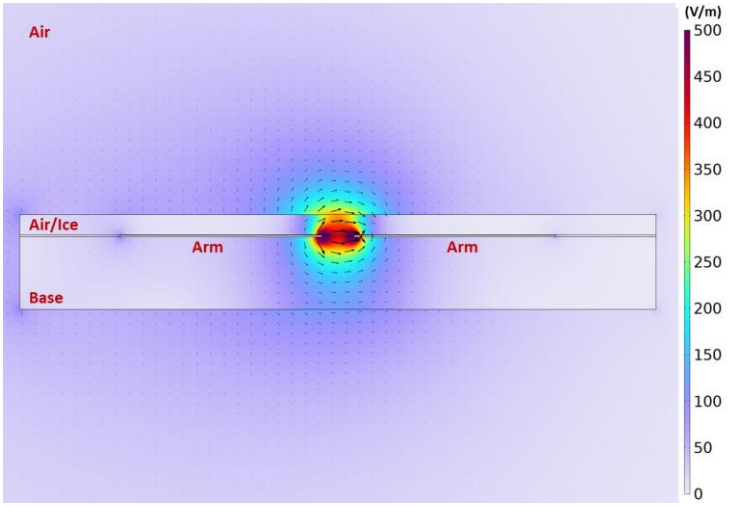

Figure 45. Result obtained from the COMSOL simulation of the sensor GAP1. It shows: Electric field norm [V/m] by means of a colour map representation and electric field distribution by means of lines.

The computed variation in capacitance as a function of ice thickness resulted in 8.55 pF/mm for GAP-1 and 4.72 pF/mm for GAP-2. These outcomes are consistent with the theoretical analysis previously discussed, confirming that the adopted modelling approach provides a reliable estimation of the sensor's capacitive response under different ice conditions.

3.3 Study on the Use as Electromagnetic Shield

3.3.1 Sample Preparation

The samples used for the evaluation of electromagnetic shielding effectiveness consist of ULTEM tiles, a high-performance thermoplastic material, fabricated by 3D printing. Each tile was subsequently coated with a graphene nanoplatelets (GNP)-based layer to impart electromagnetic shielding properties.

Several different coating formulations were developed, containing high GNP loadings combined with other constituents such as polymeric matrices (e.g., polyurethane or epoxy resin) or metallic particles (such as ferrites), in order to optimize the performance in terms of electromagnetic wave attenuation and reflection.

The coating deposition on the ULTEM samples (Figure 46) was carried out either by adhesion or by spray deposition. In the case of adhesion, films made as described in Chapter 2 were applied.

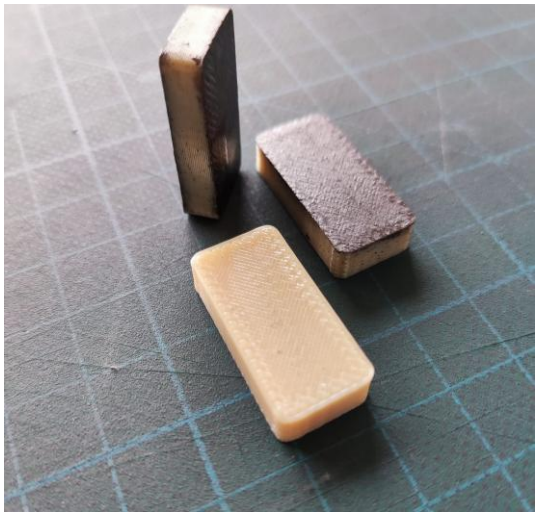

Figure 46. Sample of ULTEM with GNP-based coating for waveguide measurements.

Two sets of samples were produced: one with the coating applied on a single side of the ULTEM tile, and another with the coating on both sides, to assess the influence of the coating configuration on the overall shielding effectiveness. In Table 9 the characteristics of the realized samples are resumed.

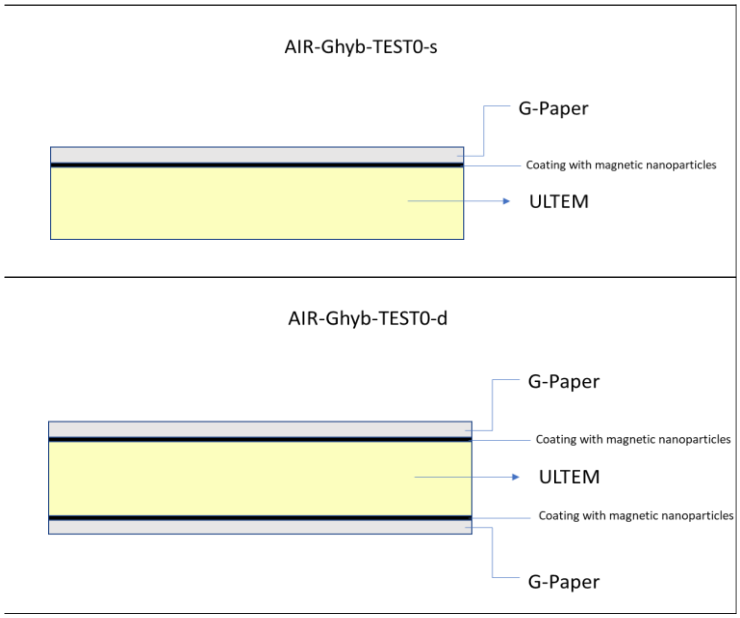

Figure 47. Schematic of the coating integration: single layer coatin (top), double-layer coating (bottom).

Table 9. Main characteristic of the sample under test.

ID	Composition	GNP/Binder wt%	Thickness [um]	Integration
AIR-GPaper	GNP	100/0	72	Adhesion
AIR-GP95	GNP/PU	95/5	70/75	Adhesion
AIR-50C	Gnp/epoxy	50/50	50-60	Spray deposition
AIR Ghyb	Gnp/ferrite	50/50	50-60	Spray deposition

3.3.2 Measurement Method

In order to characterize the behavior of a linear multi-port network operating in the microwave frequency range, the entire system can be represented ad a black box and described by means of the scattering parameters matrix, or S-matrix. The S-matrix is a mathematical construct that quantifies how radio frequency (RF) energy propagates through a multi-port network.

The scattering parameters (S-parameters) are complex quantities, since the network affects both the magnitude and phase of the incident signals. For an n-port network, the S-matrix contains n^2 elements, each representing a possible input–output path:

$$\begin{pmatrix} S_{11} & \cdots & S_{1n} \\ \vdots & \ddots & \vdots \\ S_{n1} & \cdots & S_{nn} \end{pmatrix} \tag{65}$$

For S-parameter S_{ij}, the subscript j stands for the input port, while the subscript i denotes the output port; if $i = j$, the S-parameter represents the reflection coefficient, otherwise it represents the transmission coefficient. Considering a generic two port system (Figure 48), composed of port 1 and port 2, whose reference impedances are respectively Z_{01} and Z_{02}. The phasor V_1^+ and V_2^+ correspond to the incident waves, while V_1^- and V_2^- correspond to the reflected waves.

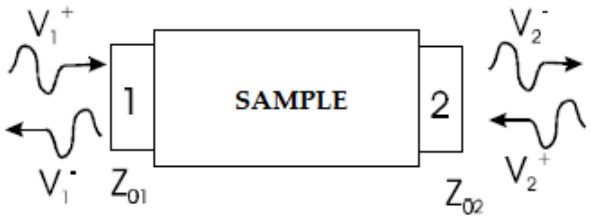

Figure 48. Transmitted and reflected waves in a two-port system.

The measurement of the shielding effectiveness (through the measurement of S-parameters) was carried out in the frequency range from 7 GHz to 15 GHz using the waveguide technique, which involves inserting the sample into the waveguide by means of a suitable sample holder.

The conceptual diagram of the measurement setup is shown in Figure 49.

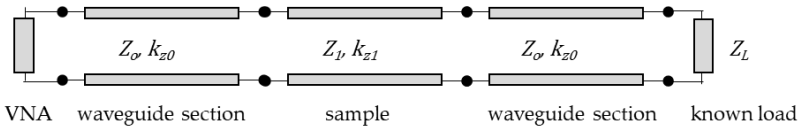

Figure 49. Layout of the measurement setup for scattering parameter characterization using the waveguide technique.

Using the waveguide technique, what is actually measured is the scattering parameter (S) matrix of the waveguide in which the specimen with the nanomaterial coating has been inserted. Through the procedures described below, the S-parameter matrix corresponding to the sample under test is extracted. The S-parameters describe transmission and reflection according to the classical relationship (Orfanidis, 2002):

$$\begin{cases} V_1^- = S_{11}V_1^+ + S_{12}V_2^+ \\ V_2^- = S_{21}V_1^+ + S_{22}V_2^+ \end{cases} \quad (66)$$

Where V+ e V- represent the forward and reflected voltage wave components, respectively, at the ends of the sample. Once these parameters are known, the shielding effectiveness (SE) can be obtained using the following formula:

$$SE_{dB} = 10\log_{10}\left(\frac{1}{|S_{12}|^2}\right) \quad (67)$$

3.3.3 Experimental Set-up and Calibration

The waveguide measurements were performed using an Anritsu 37347C Vector Network Analyzer (VNA) connected to ATM-P/N 90-120A-6-6-6 waveguides. The connection between the VNA and the waveguides was established using semi-rigid cables to ensure mechanical stability and minimize connection losses. The set-up is shown in Figure 50.

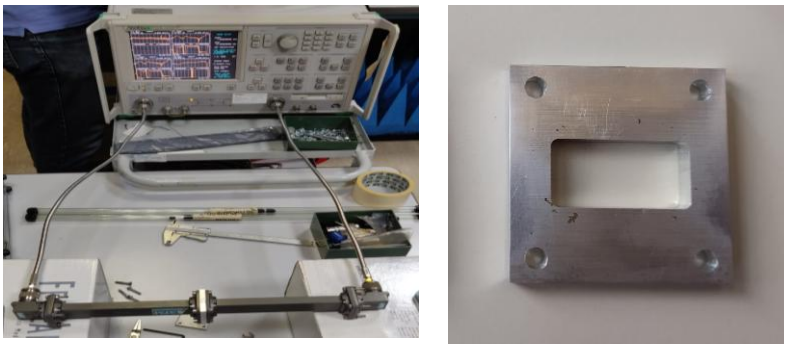

Figure 50. Picture of the used waveguide measurement set-up.

The sample was mounted in a custom-designed sample holder equipped with a slot matching exactly the dimensions of the specimen, ensuring proper alignment and optimal coupling with the waveguide walls.

The instrument calibration, required to remove the effects of cables and mechanical discontinuities, was carried out using the "TRL" (Thru-Reflect-Line) method, which consists of three main steps:

- Reference Line 1 (Thru): direct connection between the two waveguide sections with zero length (Figure 51a).
- Reflect: obtained by short-circuiting one end of the waveguide (Figure 51b).
- Reference Line 2 (Line): achieved using the empty sample holder with a known length of 5.8 mm (Figure 51c).

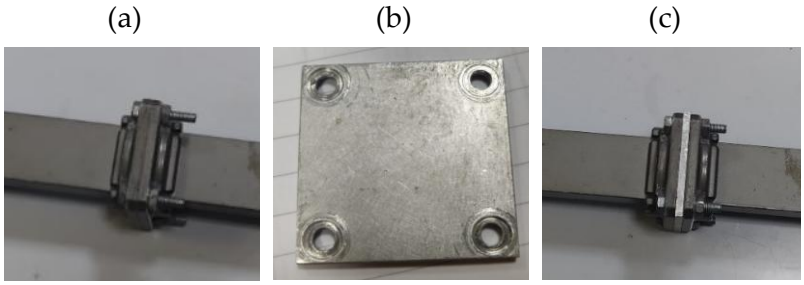

Figure 51. Waveguide connection during the TRL calibration: Thru (a), Reflect (b), Line (c).

This calibration procedure ensures an accurate reference for the system, allowing precise extraction of the scattering parameters of the sample inserted into the waveguide.

3.3.4 Experimental Results

The following figures show the scattering parameter (S-parameter) trends for two reference configurations: the bare ULTEM sample, without any coating, and the ULTEM sample coated with a copper layer, a conventional material typically used for electromagnetic shielding applications.

These two cases serve as reference benchmarks for evaluating the shielding performance of the tested materials: the bare ULTEM (**Figure 52**) represents a non-shielding dielectric substrate, while the copper-coated sample (Figure 53) provides an ideal upper limit in terms of shielding effectiveness.

Comparison with these references allows assessing the quality and effectiveness of the nanomaterial-based coatings developed in this study.

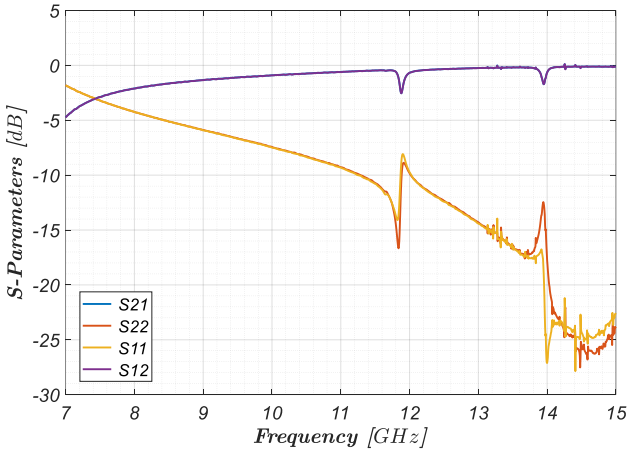

Figure 52. S-parameter of a sample of ULTEM without any coating.

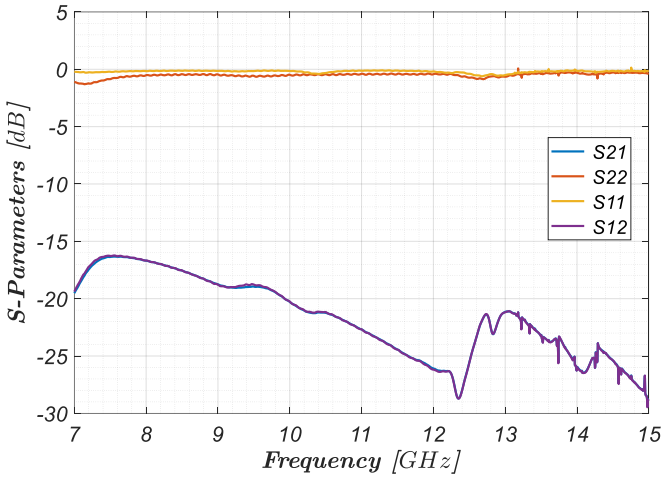

Figure 53. S-parameter of a sample of ULTEM with 1 layer of coating of copper.

S-parameter trends for a selected type of formulation are shown for 1-layer coating (Figure 54) and double-layer coating (Figure 55). Table 10 summarizes the Shielding Effectiveness (SE) values measured for the various samples, enabling a direct comparison among the different coating formulations and coating configurations investigated.

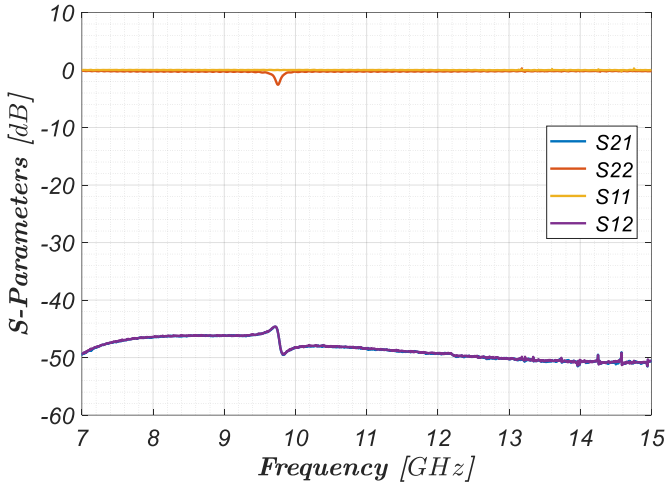

Figure 54. S-parameter of a sample of ULTEM with 1-layer coating of AIR G-PAPER.

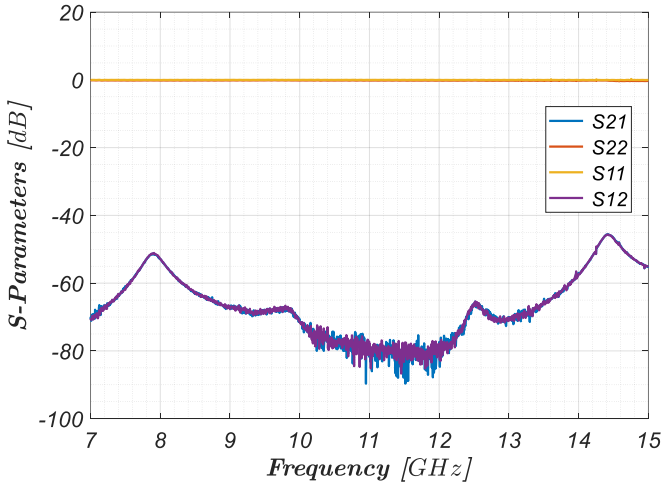

Figure 55. S-parameter of a sample of ULTEM with double-layer coating of AIR G-PAPER.

Table 10. Shielding Effectivness for the sample tested.

ID	Integration	coating layers	SE (min-max) in dB
ULT_CU		1	18 – 28
GPAPER	Adhesive	1	48 – 52
GP95	Adhesive	1	32 – 42
AIR 50C	Spray	1	28 – 38
AIR Ghyb	Spray	1	44 – 48
ULT_CU		2	22 – 56
GPAPER	Adhesive	2	45 – 80
GP95	Adhesive	2	50 – 80
AIR 50C	Spray	2	40 – 75
AIR Ghyb	Spray	2	50 – 90

3.4 Study on the Use as a Temperature Sensor

Based on the methodologies described in the previous chapter, some of the materials presented have been studied in order to evaluate their potential use as temperature sensors. Since these materials are available in the form of thin sheets, the goal is not to develop point sensors, such as thermocouples, but rather to design distributed sensors capable of combining temperature

sensing functionality with other properties, such as electromagnetic shielding.

The materials investigated for this type of application are G-PREG 95/5, G-PREG 70/30, and G-PREG 50/50. These three compositions differ both in the percentage of GNP (Graphene Nanoplatelets) and in the type of binder used; in Table 11 the main characteristics of the materials are summarized.

Table 11. Characteristics of the graphene strips analyzed for temperature sensor application.

Material	%GNP	Binder	Thickness (μm)	Length (cm)	Width (cm)
G-PREG (95/5)	95	Polyurethane 5%	94	10	1
G-PREG (70/30)	70	Epoxy 30%	85	10	1
G-PREG (50/50)	47.5	Boron nitride 47.5%, Polyurethane 5%	100	10	1

The operating principle of the sensor is based on the variation of the electrical resistance of the film as a function of temperature. Specifically, an increase in temperature causes a change in the resistance of the strip, and the analysis of the resistance–temperature trend allows the determination of an TCR (Temperature Coefficient of the Resistance), which relates the two quantities according to the following equation often used in its approximated version (69)

$$TCR(T) = \frac{1}{R(T)}\frac{dR(T)}{dT} \tag{68}$$

$$TCR(T) = \frac{\Delta R(T)}{R(T_0)\Delta T} = \frac{1}{R(T_0)}\frac{R(T) - R(T_0)}{T - T_0} \tag{69}$$

3.4.1 Set-up and characterization

A first experimental setup was used to perform preliminary analyses.

The measurement was based on the ammeter–voltmeter method, implemented using a SIGLENT SPS5041X DC power supply and two Agilent 34401A multimeters connected in a downstream voltmeter configuration. The power supply applied different current levels to the nanostrip, while one multimeter measured the current and the other the corresponding voltage drop. All instruments were remotely controlled via a GPIB-488 interface to ensure repeatability and automated data acquisition. A key element of the measurement system is a test fixture specifically designed and manufactured for the characterization of this type of material, as previously described in Chapter 2.

Through this setup, a preliminary V–I characterization was performed within the current range of interest, confirming a linear relationship between the applied current and the measured voltage drop. This result demonstrates the ohmic behavior of the material and its suitability for subsequent thermo-electrical characterization.

For the electro-thermal characterization, the sensor resistance was measured at different controlled temperature set points. Measurements were performed using an Agilent 34401A multimeter in a four-wire configuration to minimize the influence of contact resistances. The instrument was remotely controlled via a GPIB-488 interface, while environmental conditions were managed through an ACS DY110 climatic chamber (Angelantoni, Massa Martana, Italy), allowing precise control of temperature and humidity.

The chamber's built-in sensors provided reference values for temperature and humidity. The procedure included an initial phase where temperature was varied without humidity control, followed by measurements performed at fixed humidity levels.

Each temperature was reached during both heating and cooling cycles to evaluate possible hysteresis effects. Once steady-state conditions were achieved, resistance readings were averaged to obtain the final values. Temperature stability was verified using a Fluke Hydra data logger with K-type thermocouples positioned on the nanosensor surface.

The trends of the resistance as a function of temperature for the three tested materials are shown in Figure 56.

(a)

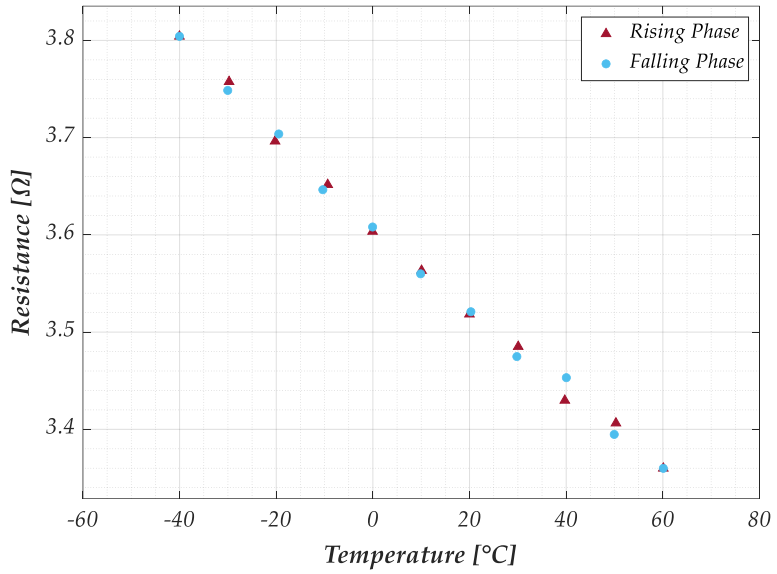
Rising Phase
Falling Phase
Resistance [Ω]
3.8
3.7
3.6
3.5
3.4
-60
-40
-20
0
20
40
60
80
Temperature [°C]

(b)

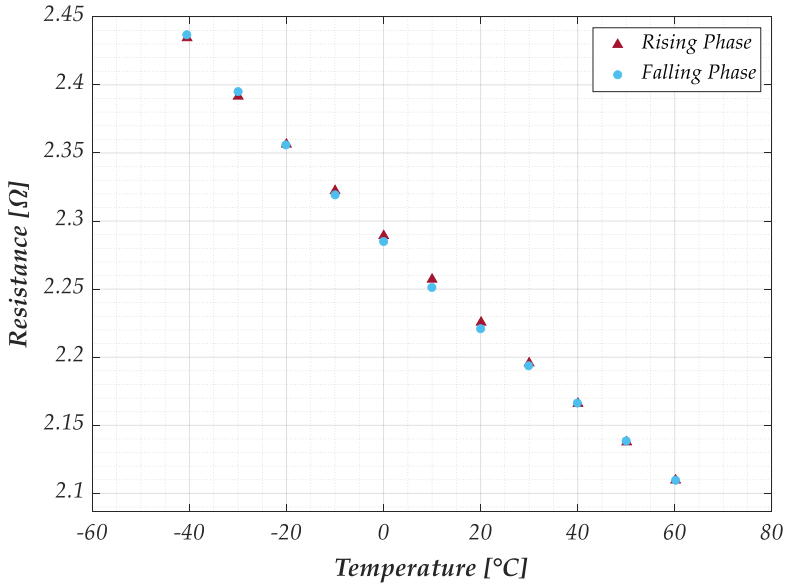
Rising Phase
Falling Phase
Resistance [Ω]
2.45
2.4
2.35
2.3
2.25
2.2
2.15
2.1
-60
-40
-20
0
20
40
60
80
Temperature [°C]

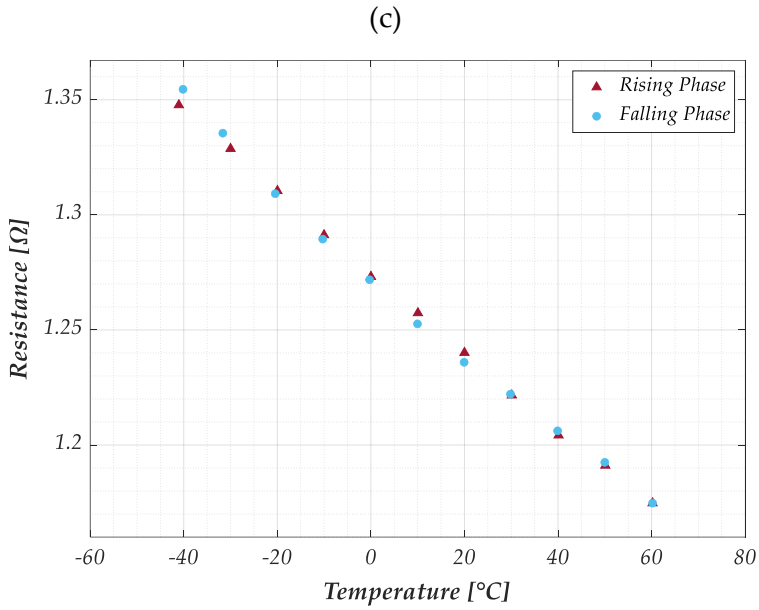

Figure 56. Measured electrical resistance of the graphene samples with temperature cycling in the range -40°C to 60°C: (a) G-PREG 50/50; (b) G-PREG 70/30; (c) G-PREG 95/5 (Siconolfi, 2025).

A repeatability analysis of the resistance measurements was carried out by evaluating the Type B uncertainty over ten consecutive measurements performed at different temperature levels, without humidity control. This analysis was conducted for each sample and formulation during both the heating and cooling cycles.

The nanomaterial exhibited excellent repeatability under all tested conditions. As an example, Table 3 reports the Type A and Type B uncertainties obtained for a G-PREG 50/50 sample during the heating phase at each temperature level. The results indicate that the contribution of Type B uncertainty, related to measurement repeatability, is negligible when compared to the

Type A component, confirming the high stability and consistency of the experimental setup. Comparable behavior was observed for the other two materials.

Table 12. Type A and type B uncertainties estimated for a sample of the G-PREG 50/50 strip under rising conditions.

R [Ω]	u_B (R) [Ω]	u_A (R) [Ω]	T [°C]	u_B (T) [°C]	u_A (T) [°C]
3.804	0.000	0.004	-40.030	0.014	0.230
3.758	0.001	0.004	-29.760	0.029	0.230
3.705	0.001	0.004	-19.480	0.053	0.230
3.652	0.000	0.004	-9.350	0.055	0.230
3.608	0.000	0.004	-0.060	0.021	0.230
3.563	0.000	0.004	10.070	0.014	0.230
3.521	0.000	0.004	20.280	0.044	0.230
3.485	0.000	0.004	30.070	0.040	0.230
3.453	0.000	0.004	40.030	0.028	0.230
3.406	0.000	0.004	50.290	0.026	0.230
3.360	0.000	0.004	60.100	0.000	0.230

Even though all three materials displayed a comparable thermal–electrical response, G-PREG 50/50 was chosen for further analysis of its temperature-sensing capabilities, as it exhibited the lowest relative uncertainty among the tested formulations (Table 13). For each sample and material composition, the combined standard uncertainty was calculated at every temperature level during both the heating and cooling phases, under conditions without humidity control.

The overall uncertainty assessment accounted for both Type A and Type B contributions, as previously defined in Table 12. To provide a conservative evaluation, the highest recorded uncertainty value for each sensor strip was considered as the reference.

Table 13. Relative uncertainty (%) for each material.

Material	Relative uncertainty [%]
G-PREG (50/50)	0,13
G-PREG (70/30)	0,21
G-PREG (95/5)	0,36

The resistance as a function of temperature for the G-PREG 50/50 sample is shown in Figure 57, highlighting the influence of different controlled humidity levels on the sensor's electrical response.

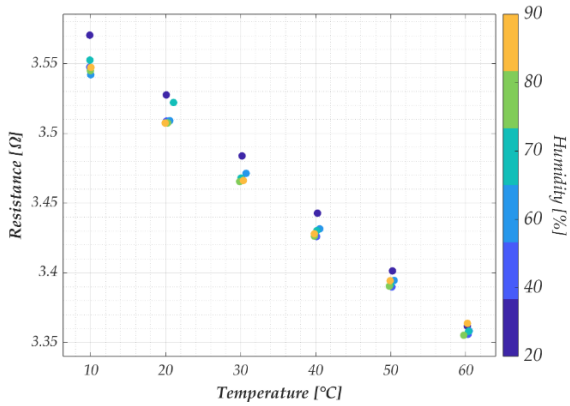

Figure 57. Trend of resistance as a function of temperature for different humidity levels for the G-PREG 50/50 sample (Siconolfi, 2025).

Based on the experimental results, a linear model can be adopted to describe the calibration curve of the proposed temperature sensor.

$$T(R) = \alpha_0 + \alpha_1 R \quad (70)$$

This linear formulation, which involves only two parameters, represents a specific case of the more general polynomial model.

$$T(R) = \alpha_0 + \alpha_1 R + \alpha_2 R^2 + \cdots + \alpha_p R^p \quad (71)$$

The choice of a first-order model is supported by the experimental data (Figure 57), which exhibit a nearly linear correlation between resistance and temperature.

The parameters α_0 and α_1 were identified using resistance measurements collected at six temperature set points: −40°C, −20°C, 0°C, 20°C, 40°C, and 60°C. Model validation was then performed using additional data obtained at intermediate temperature levels of −30°C, −10°C, 10°C, 30°C, and 50°C. For each calibration and validation point, the resistance values were averaged over multiple measurements after reaching steady-state thermal conditions.

The influence of ambient humidity on the sensor's electrical response was also investigated. To this purpose, tests were conducted within the temperature interval of 10°C–60°Cat controlled relative humidity levels of 20%, 40%, 60%, 70%, 80%, and 90%. Each combination of temperature and humidity was maintained until thermal and hygrometric equilibrium was reached, after which the corresponding resistance values were recorded.

The sensor model was finally expressed in differential form to allow the analysis of temperature variations, according to the relation:

$$\Delta T = \alpha_1 \cdot \Delta R \tag{72}$$

Uncertainty propagation for this differential model was evaluated by considering the correlation between the measured quantities. The combined standard uncertainties were calculated using the following expressions:

$$u(\Delta R) = \sqrt{(u(R_2)^2 + u(R_1)^2 - u(R_1) \cdot u(R_2))} \tag{73}$$

$$u(\Delta T) = \sqrt{([u(\alpha_1) \cdot \Delta R]^2 + [\alpha_1 \cdot u(\Delta R)]^2)} \tag{74}$$

where $u(R_1)$ and $u(R_2)$ represent the standard uncertainties of the resistance measurements, and $u(\alpha_1)$ is the uncertainty associated with the model coefficient α_1.

Figure 58 shows the plots of the temperature versus electrical resistance trends according to the proposed linear model for two different G-PREG 50/50 samples. Table 14 reports the estimated composite and model uncertainties calculated for the same films.

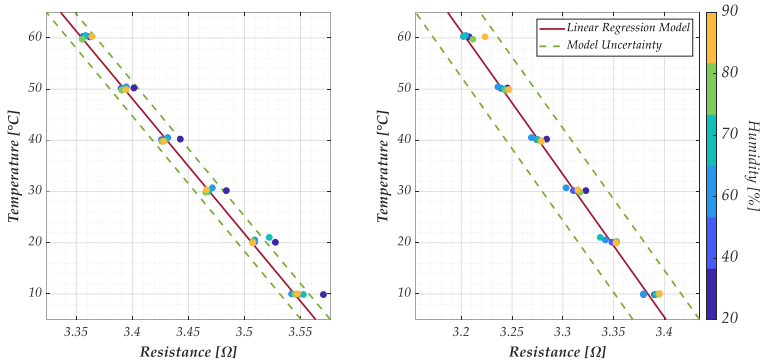

Figure 58. Plots of the temperature versus the electrical resistance according to the proposed linear model, for samples 1 (left) and 2 (right) of the G-PREG 50/50 films for different values of relative humidity from 20% to 90%. Coloured dots are the measured values, whereas the solid red line is the sensor response, and the green dashed lines represent the model uncertainty (Siconolfi, 2025).

The plots show a clear linear correlation between resistance and temperature for all tested samples, confirming the suitability of a first-order model to describe the sensor behavior. The experimental data used for calibration and validation fall within the uncertainty bounds, demonstrating good agreement between the measured and predicted values.

The comparison between different humidity levels highlights a slight dependence of the sensor response on ambient humidity. For relative humidity values between 40% and 60%, the effect remains within the uncertainty range, while at higher humidity levels, a modest deviation from linearity can be observed.

Table 14. Estimated composite and model uncertainties of the G-PREG 50/50 films

R [Ω]	u_B (R) [Ω]	u_A (R) [Ω]	T [°C]	u_B (T) [°C]	u_A (T) [°C]
3.899	0.004	-40.03	0.230	3.900	2.923
3.794	0.004	-20.24	0.230	3.790	2.922
3.683	0.004	-0.06	0.230	3.680	2.922
3.583	0.004	20.28	0.230	3.580	2.922
3.485	0.004	39.71	0.230	3.480	2.922
3.399	0.004	60.10	0.230	3.400	2.923

The estimated uncertainties associated with the resistance and temperature measurements indicate that the G-PREG 50/50 strips can operate reliably within the investigated range, with an overall temperature prediction uncertainty of approximately ±3°C. When used to detect relative temperature variations, the same configuration allows a resolution of about 2°C.

CONCLUSIONS

This thesis has presented a comprehensive experimental and numerical investigation of the electrical, thermal, and multifunctional properties of thin films and macroscopic strips made of graphene nanoplatelets (GNPs), with the aim of assessing their potential use in electrothermal and sensing applications. The work integrates analytical modeling, numerical simulation, and advanced experimental characterization, leading to a consistent understanding of the physical behavior of industrial-grade graphene-based materials under various operating conditions.

1. Electrical Behavior and Electrothermal Modeling

- A temperature-dependent analytical model of electrical resistivity was developed and validated for GNP-based strips. The model, derived from combined experimental and numerical analyses, follows a linear temperature law similar to that of conventional metals but with a Negative Temperature Coefficient (NTC). The numerical electrothermal model was verified through Joule-heating experiments, showing that the predicted temperature distributions accurately match the experimental IR thermography results. This confirms the consistency between electrical and thermal characterizations and the reliability of the proposed modeling framework.

2. Thermal Characterization and Modeling Methodology

- A simplified experimental–numerical methodology was proposed and validated for the estimation of thermal

conductivity (k) and thermal diffusivity (α) of thin GNP strips The method is based on the analysis of transient thermal responses induced by Joule heating and recorded by IR thermography. Compared to standard techniques such as the laser-flash method it requires less complex equipment and can be easily implemented for fast and low-cost industrial quality control. The methodology was applied to various GNP-based strips with different binder contents and thicknesses, showing a clear dependence of the thermal parameters on the filler percentage. The applicability range of the method was identified between 150 and 1000 W/(m·K) for thermal conductivity and 1.5–8 × 10^{-4} m^2/s for thermal diffusivity, with an overall uncertainty below 20% (Giovinco, 2023).

3. Multifunctional Properties and Potential Applications

- The studied GNP-based materials exhibit a stable and reproducible NTC behavior, which enables their use as temperature-sensing elements. A linear temperature–resistance model was proposed and validated, achieving a prediction uncertainty of ±2–3 °C in the range –40 to +60 °C. Sensitivity to humidity was found negligible within 40–60% RH, confirming the robustness of the sensors for environmental applications (Siconolfi, 2025).

- The same GNP films, when electrically biased, demonstrated excellent Joule-heating capabilities, meeting the requirements for de-icing and anti-icing systems in aeronautical environments. The uniformity and stability of the temperature field, both in transient and steady-state regimes,

make these materials highly suitable for electrothermal surface heating applications.

- The dual functionality of GNP coatings was further demonstrated by integrating the same material into a planar capacitor configuration for ice detection. The impedance variation between frozen and non-frozen conditions provided reliable detection up to 200 Hz, suggesting the feasibility of self-sensing de-icing systems, where the same graphene strip can detect and remove ice (Sibilia, 2023; Tari, 2025).
- Additional studies confirmed that thin GNP coatings can provide effective electromagnetic shielding when integrated into polymeric structures, with 30–50 dB attenuation in the 7 GHz–15 GHz range, while maintaining low weight and high conductivity.

REFERENCES

- Abdellatif, A. A. H., Younis, M. A., Alsharidah, M., Al Rugaie, O. and Tawfeek, H. M. (2022) 'Biomedical applications of quantum dots: Overview, challenges, and clinical potential', International Journal of Nanomedicine, 17, pp. 1951–1970. https://doi.org/10.2147/IJN.S357980
- Ashcroft, N. W., & Mermin, N. D. (1976). Solid State Physics. Saunders College
- Balandin AA. Thermal properties of graphene and nanostructured carbon materials. Nature Materials. 2011;10(8):569–581. doi: 10.1038/nmat3064.
- Balberg, I. (1987) 'Tunneling and nonuniversal conductivity in composite materials', Physical Review Letters, 59(12), pp. 1305–1308. ttps://doi.org/10.1103/PhysRevLett.59.1305
- Bauhofer, W., & Kovacs, J. Z. (2009). "A review and analysis of electrical percolation in carbon nanotube polymer composites". Composites Science and Technology, 69(10), 1486-1498.
- Bejan A and Kraus A D Heat transfer handbook. New York: J. Wiley, 2003.
- Bilisik, K. and Akter, M. (2022) 'Polymer nanocomposites based on graphite nanoplatelets (GNPs): a review on thermal-electrical conductivity, mechanical and barrier properties', Journal of Materials Science, 57, pp. 7425–7480. https://doi.org/10.1007/s10853-022-07092-0
- Botura, G., Sweet, D. and Flosdorf, D. (2005) 'Development and Demonstration of Low Power Electro-Thermal De-icing System', in 43rd AIAA Aerospace Sciences

Meeting and Exhibit, Reno, NV, USA, AIAA Paper 2005-1460. https://doi.org/10.2514/6.2005-1460.

- Cai, M., Thorpe, D., Adamson, D. H. and Schniepp, H. C. (2012) 'Methods of graphite exfoliation', Journal of Materials Chemistry, 22, pp. 24992–25002.
- Cha C, Shin SR, Annabi N, Dokmeci MR, Khademhosseini A. Carbon-based nanomaterials: multifunctional materials for biomedical engineering. ACS Nano. 2013 Apr 23;7(4):2891-7. doi: 10.1021/nn401196a.
- Charlier, J. C., Blase, X. and Roche, S. (2007) 'Electronic and transport properties of nanotubes', Reviews of Modern Physics, 79(2), pp. 677–732.
- Choy, T. C. (2015) Effective Medium Theory: Principles and Applications. Oxford: Oxford University Press.
- Churchill, S. W. and Chu, H. H. S. (1975) 'Correlating equations for laminar and turbulent free convection from a vertical plate', International Journal of Heat and Mass Transfer, 18(11), pp. 1323–1329.
- Dabrowska, A., Bellucci, S., Cataldo, A., Micciulla, F. and Huczko, A. (2014) 'Nanocomposites of epoxy resin with graphene nanoplates and exfoliated graphite: Synthesis and electrical properties', Physica Status Solidi (b), 251(12), pp. 2599–2602.
- Dong, L., Zhang, Z., Zheng, H., Yang, G., Hu, J., Shu, L. and Jiang, X. (2025) 'Ice thickness/density measurement method based on its capacitance effect', High Voltage, 10(2), pp. 400–410.
- Fakorede, O., Feger, Z., Ibrahim, H., Ilinca, A., Perron, J. and Masson, C. (2016) 'Ice protection systems for wind turbines in cold climate: Characteristics, comparisons and analysis', Renewable and Sustainable Energy Reviews, 65, pp. 662–675.

https://www.sciencedirect.com/science/article/pii/S1364032116303124. ISSN 1364-0321.

- Falkovsky, L. A. (2008) 'Optical properties of graphene', Journal of Physics: Conference Series, 129(1), 012004.
- Forestiere, C., Maffucci, A. and Miano, G. (2010) 'Hydrodynamic model for the signal propagation along carbon nanotubes', Journal of Nanophotonics, 4(1), 041695.
- Forestiere, C., Maffucci, A. and Miano, G. (2011) 'On the evaluation of the number of conducting channels in multiwall carbon nanotubes', IEEE Transactions on Nanotechnology, 10(6), pp. 1221–1223.
- Ghosh S, Calizo I, Teweldebrhan D, Pokatilov EP, Nika DL, Balandin AA, Bao W, Miao F, Lau CN. Extremely high thermal conductivity of graphene: Prospects for thermal management applications in nanoelectronic circuits. Appl. Phys. Lett. 92, 151911 (2008). https://doi.org/10.1063/1.2907977
- Gilboa, G., Sochen, N. A. and Zeevi, Y. Y. (2002) 'Regularized shock filters and complex diffusion', in Heyden, A., Sparr, G., Nielsen, M. and Johansen, P. (eds.) Computer Vision — ECCV 2002. Berlin, Heidelberg: Springer Berlin Heidelberg, pp. 399–413.
- Giovinco G, Sibilia S, Maffucci A. Characterization of the thermal conductivity and diffusivity of graphene nanoplatelets strips: a low-cost technique. Nanotechnology. 2023 Jun 6;34(34):345703. doi: 10.1088/1361-6528/acd5da.
- Gonçalves, G. Nanocarbon-Based Composites and Their Thermal, Electrical, and Mechanical Properties. C 2025, 11, 21. https://doi.org/10.3390/c11010021

- Gusynin, V. P., Sharapov, S. G. and Carbotte, J. P. (2006) 'Magneto-optical conductivity in graphene', Journal of Physics: Condensed Matter, 19(2), 026222.
- Hasselman, D. P. H. and Johnson, L. F. (1987) 'Effective thermal conductivity of composites with interfacial thermal barrier resistance', Journal of Composite Materials, 21(6), pp. 508–515. https://doi.org/10.1177/002199838702100602
- Horng, J., Chen, C.-F., Geng, B., Girit, C., Zhang, Y., Hao, Z., Bechtel, H. A., Martin, M., Zettl, A. et al. (2011) 'Drude conductivity of Dirac fermions in graphene', Physical Review B, 83, 165113. https://doi.org/10.1103/PhysRevB.83.165113.
- Hu, Z., Tong, G., Lin, D., Chen, C., Guo, H., Xu, J. and Zhou, L. (2016) 'Graphene-reinforced metal matrix nanocomposites – A review', Materials Science and Technology, 32, pp. 930–953. https://doi.org/10.1080/02670836.2015.1104018
- Huang, J., Yang, X., Her, S.-C. and Liang, Y.-M. (2019) 'Carbon nanotube/graphene nanoplatelet hybrid film as a flexible multifunctional sensor', Sensors, 19(2).
- Jiménez-Suárez, A. and Prolongo, S. G. (2020) 'Graphene nanoplatelets', Applied Sciences, 10(5).
- Karim, N., Zhang, M., Afroj, S., Koncherry, V., Potluri, P. and Novoselov, K. S. (2018) 'Graphene-based surface heater for de-icing applications', RSC Advances, 8, pp. 16815–16823. https://doi.org/10.1039/C8RA02567C.
- Kirkpatrick, S. (1973). Percolation and conduction. Reviews of Modern Physics, 45(4), 574-588.
- Kovtun A et al. 2019 Benchmarking of graphene-based materials: real commercial products vs. ideal graphene 2D Materials 6 025006.

- Lahbacha, K.; Sibilia, S.; Trezza, G.; Giovinco, G.; Bertocchi, F.; Chiodini, S.; Cristiano, F.; Maffucci, A. Electro-Thermal Parameters of Graphene Nano-Platelets Films for De-Icing Applications. Aerospace 2022, 9, 107. https://doi.org/10.3390/aerospace9020107
- Lange, F. F. (1973) 'Effect of microstructure on strength of Si_3N_4–SiC composite system', Journal of the American Ceramic Society, 56(9), pp. 445–450.
- Lee, K.-S., Prasad, P. N., Huyet, G. and Tan, C. H. (2012) 'Feature issue introduction: Quantum dots for photonic applications', Optical Materials Express, 2, pp. 682–684.
- Maffucci, A. and Miano, G. (2013) 'Number of conducting channels for armchair and zig-zag graphene nanoribbon interconnects', IEEE Transactions on Nanotechnology, 12(5), pp. 817–823.
- Maffucci, A., Micciulla, F., Cataldo, A. E., Miano, G. and Bellucci, S. (2017) 'Modeling, fabrication, and characterization of large carbon nanotube interconnects with negative temperature coefficient of the resistance', IEEE Transactions on Components, Packaging and Manufacturing Technology, 7(4), pp. 485–493.
- Maffucci, A., Micciulla, F., Cataldo, A., Miano, G. and Bellucci, S. (2016) 'Bottom-up realization and electrical characterization of a graphene-based device', Nanotechnology, 27(9), 095204.
- Malik, R., Huang, Q., Silvestri, L., Liu, D., Pellegrini, V., Marasco, L., Venezia, E., Abouali, S., Bonaccorso, F., Lain, M. J., Greenwood, D., West, G., Shearing, P. R. and Loveridge, M. J. (2020) 'Synthesis of layered silicon-graphene hetero-structures by

wet jet milling for high capacity anodes in Li-ion batteries', 2D Materials, 8(1), 015012.

- Mbayachi, V. B., Ndayiragije, E., Sammani, T., Taj, S., Mbuta, E. R. and Khan, A. U. (2021) 'Graphene synthesis, characterization and its applications: A review', Environmental Technology & Innovation, 3, 100163. https://www.sciencedirect.com/science/article/pii/S2211715621000680. ISSN 2211-7156.
- McLachlan, D. S. (1987) 'An equation for the conductivity of binary mixtures with anisotropic grain structures', J. Phys. C: Solid State Phys.20 865. Doi: 10.1088/0022-3719/20/7/004
- Min, H., Jain, P., Adam, S. and Stiles, M. D. (2011) 'Semiclassical Boltzmann transport theory for graphene multilayers', Physical Review B, 83, 195117. https://doi.org/10.1103/PhysRevB.83.195117
- Nan, C. W. (1993) 'Physics of inhomogeneous inorganic materials, Progress in Materials Science, 37(1), pp. 1–116. https://doi.org/10.1016/0079-6425(93)90004-5
- Nan, C.-W., Birringer, R., Clarke, D.R. and Gleiter, H. (1997) Effective Thermal Conductivity of Particulate Composites with Interfacial Thermal Resistance. Journal of Applied Physics, 81, 6692-6699. http://dx.doi.org/10.1063/1.365209
- Omanović-Mikličanin, E., Badnjević, A., Kazlagić, A. et al. Nanocomposites: a brief review. Health Technol. 10, 51–59 (2020). https://doi.org/10.1007/s12553-019-00380-x
- Orfanidis, S. J. (2002) Electromagnetic Waves and Antennas. Rutgers University, New Brunswick, NJ.
- Palmer, H. B. (1937) 'The capacitance of a parallel-plate capacitor by the Schwartz-Christoffel transformation',

Transactions of the American Institute of Electrical Engineers, 56(3), pp. 363–366.

- Peigney, A., Laurent, C., Flahaut, E. and Rousset, A. (2000) 'Carbon nanotubes in novel ceramic matrix nanocomposites', Ceramics International, 26, pp. 677–683. https://www.sciencedirect.com/science/article/pii/S0272884200000043. ISSN 0272-8842.
- Prabhakaran, P., Kim, W. J., Lee, K.-S. and Prasad, P. N. (2012) 'Quantum dots (QDs) for photonic applications', Optica Publishing Group, 2, pp. 578–593. https://opg.optica.org/ome/abstract.cfm?URI=ome-2-5-578
- Rahman, M. A. (2014) 'A review on semiconductors including applications and perspectives', Journal of Scientific & Industrial Research, 73, pp. 68–76. https://core.ac.uk/download/pdf/235049651.pdf
- Rahman, M. M., Khan, K. H., Parvez, M. M. H., Irizarry, N. and Uddin, M. N. (2025) 'Polymer nanocomposites with optimized nanoparticle dispersion and enhanced functionalities for industrial applications', Processes, 13(4), 994. https://www.mdpi.com/2227-9717/13/4/994. ISSN 2227-9717.
- Reich, S., Maultzsch, J. and Ordejón, P. (2002) 'Tight-binding description of graphene', Physical Review B, 66, 035412. https://doi.org/10.1103/PhysRevB.66.035412.
- Ren, W., Cheng, HM. The global growth of graphene. Nature Nanotech 9, 726–730 (2014). https://doi.org/10.1038/nnano.2014.229
- Saleh M, Alshahrani T, Almutairi M, Alharbi A, Alghamdi A. Comprehensive review of carbon-based nanostructures: properties, synthesis, characterization, and applications. Journal

of Industrial and Engineering Chemistry. 2024;132:1–22. doi: 10.1016/j.jiec.2024.01.035.

- Seibold P 2020 Largest inscribed rectangle square or circle, MATLAB Central File Exchange.
- Sevostianov, I, Mogilevskaya, S.G., Kushch, V.I. (2019) 'Maxwell's methodology of estimating effective properties: alive and well', International Journal of Engineering Science 140 (2019) 35–88. https://doi.org/10.1016/j.ijengsci.2019.05.001
- Shahil, K. M. F. and Balandin, A. A. (2012) 'Graphene–multilayer graphene nanocomposites as highly efficient thermal interface materials', Nano Letters, 12, pp. 861–867. https://doi.org/10.1021/nl203906r. PMID 22214526.
- Shariatinia, Z. (2021) 'Applications of carbon nanotubes', in Thomas, S., Sarathchandran, C., Ilangovan, S. A. and Moreno-Piraján, J. C. (eds.) Micro and Nano Technologies. Elsevier, pp. 321–364.
- Sherman, R. D., Middleman, L. M. and Jacobs, S. M. (1983) 'Electron transport processes in conductor-filled polymers', Polymer Engineering & Science, 23(1), pp. 36–46. https://doi.org/10.1002/pen.760230109
- Sibilia, S., Bertocchi, F., Chiodini, S., Cristiano, F., Ferrigno, L., Giovinco, G. and Maffucci, A. (2021) 'Temperature-dependent electrical resistivity of macroscopic graphene nanoplatelet strips', Nanotechnology, 32(27), 275701. https://doi.org/10.1088/1361-6528/abef95.
- Sibilia, S.; Tari, L.; Bertocchi,F.; Chiodini, S.; Maffucci, A. A Capacitive Ice-Sensor Based onGraphene Nano-Platelets Strips.Sensors 2023, 23, 9877. https://doi.org/10.3390/s23249877

- Siconolfi, F.; Cavaliere, G.;Sibilia, S.; Cristiano, F.; Giovinco, G.;Maffucci, A. Industrial-GradeGraphene Films as DistributedTemperature Sensors. Sensors 2025, 25,3227. https://doi.org/10.3390/s25103227.
- Siegel, R. W., Chang, S. K., Ash, B. J., Stone, J., Ajayan, P. M., Doremus, R. W. and Schadler, L. S. (2001) 'Mechanical behavior of polymer and ceramic matrix nanocomposites', Scripta Materialia, 44, pp. 2061–2064. https://www.sciencedirect.com/science/article/pii/S1359646201008922. ISSN 1359-6462.
- Simmons, J. G. (1963) 'Generalized formula for the electric tunnel effect between similar electrodes separated by a thin insulating film', Journal of Applied Physics, 34(6), pp. 1793–1803.
- Singh, K. J., Ahmed, T., Gautam, P., Sadhu, A. S., Lien, D.-H., Chen, S.-C., Chueh, Y.-L. and Kuo, H.-C. (2021) 'Recent advances in two-dimensional quantum dots and their applications', Nanomaterials, 11(6), 1549. https://www.mdpi.com/2079-4991/11/6/1549. ISSN 2079-4991.
- Singh, Y. (2013) 'Electrical resistivity measurements: A review', International Journal of Modern Physics: Conference Series, 22, pp. 745–756.
- Stauffer, D., & Aharony, A. (1992). Introduction To Percolation Theory: Second Edition (2nd ed.). Taylor & Francis. https://doi.org/10.1201/9781315274386
- Stroud D., "Generalized effective-medium approach to the conductivity of an inhomogeneous material", Phys. Rev. B 12, 3368–3373 (1975). https://doi.org/10.1103/PhysRevB.12.3368
- Tari, L., Cavaliere, G., Sibilia, S., Chiodini, S., Ferrigno L, and Maffucci, A. "Design of a low-cost oscillator-based

conditioning method for a graphene film-based capacitive sensor in aerospace de-icing applications," 2025 IEEE International Instrumentation and Measurement Technology Conference (I2MTC), Chemnitz, Germany, 2025, pp. 1-6, doi: 10.1109/I2MTC62753.2025.11079111.

- Tian, X., Itkis, M. E., Bekyarova, E. B. and Haddon, R. C. (2013) 'Anisotropic thermal and electrical properties of thin thermal interface layers of graphite nanoplatelet-based composites', Scientific Reports, 3, 1710. https://doi.org/10.1038/srep01710.
- Todri-Sanial, A., Dijon, J. and Maffucci, A. (2017) Carbon Nanotubes for Interconnects: Process, Design and Applications. Springer.
- Yu Y.-J., Han M. Y., Berciaud S., Georgescu A. B., Heinz T. F., Brus L. E., Kim K. S., Kim P. High-resolution spatial mapping of the temperature distribution of a Joule self-heated graphene nanoribbon. Applied Physics Letters. 2011 Oct 31;99(18):183105. https://doi.org/10.1063/1.3657515
- Wang, R. M., Zheng, S. R. and Zheng, Y. P. (2011) Polymer Matrix Composites and Technology. Woodhead Publishing Limited and Science Press Limited.
- Wang, Y., Shan, J. W. & Weng, G. J. (2015) 'Percolation threshold and electrical conductivity of graphene-based nanocomposites with filler agglomeration and interfacial tunneling', Journal of Applied Physics, 118(6), 065101. researchwithrutgers.com+2pubs.aip.org+2
- Wang, Z. (2017) 'Recent progress on ultrasonic de-icing technique used for wind power generation, high-voltage transmission line and aircraft', Energy and Buildings, 140, pp. 42–

49.
https://www.sciencedirect.com/science/article/pii/S0378778817302633. ISSN 0378-7788.

- Xie, J., Li, Z., Lu, B. and Yuan, W. (2024) 'A flexible CSRR-based array icing sensor with defective microstrip structure', IEEE Sensors Journal, 24(12), pp. 19934–19943.
- Xu, Zhiping. (2018). Fundamental Properties of Graphene. 10.1016/B978-0-12-812651-6.00004-5.
- Yamazaki, M., Jemcov, A. R. and Sakaue, H. (2021) 'A review on the current status of icing physics and mitigation in aviation', Aerospace, 8(7), 188. https://www.mdpi.com/2226-4310/8/7/188. ISSN 2226-4310.
- Zhang, H., Cong, X., Xiao, W., Ameyama, K. and Ma, C. (2016) 'Enhanced mechanical properties of Al5083 alloy with graphene nanoplates prepared by ball milling and hot extrusion', Materials Science and Engineering: A, 658, pp. 8–15.
- Zhang, H., Zhu, H., Xu, C., Li, Y., Liu, Q., Wang, S. and Yan, S. (2022) 'Effect of nanoparticle size on the mechanical properties of polymer nanocomposites', Polymer, 252, 124944. https://www.sciencedirect.com/science/article/pii/S0032386122004323. ISSN 0032-3861.
- https://doc.comsol.com.

ACKNOWLEDGMENTS

Questo lavoro di tesi è stato in parte dalla EU Commission, nell'ambito del progetto "SH10 GICE", Graphene Flagship, Core3/H2020-SGA-FET-GRAPHENE-2019, grant #881603, del progetto "TERASSE", H2020-MSCA-RISE Programme, grant #823878, and by MUR—Next Generation EU, del progetto ECS 0000024 "Rome Technopole", CUP H33C22000420001 e del progetto PRIN 2022 "SENS-AI", grant #2022R5HWJN.

Ringrazio le aziende Nanesa s.r.l., Jaber Innovation s.r.l. e ASD s.r.l. per il supporto dato durante tutto il periodo di ricerca sia per le forniture dei materiali in esame, sia per le applicazioni.